Modeling Sheets and Fibers in Biological Tissues

Babak Samari

Doctor of Philosophy

School of Computer Science
McGill University
Montreal, Quebec, Canada

A thesis submitted to McGill University in partial
fulfillment of the requirements of the degree of
Doctor of Philosophy

Acknowledgements

I am deeply grateful to my doctoral supervisor, Professor Kaleem Siddiqi. His outstanding dedication and responsibility towards his students, his vision and deep knowledge of the field, and his kindness and sense of understanding made my doctoral studies, though challenging at times, always rewarding and fulfilling. I also want to share my gratitude with researchers and colleagues with who I had the opportunity to work with and learn from: Professor Gregory Dudek, Professor Gustav Strijkers, Professor Ioannis Rekleitis, Doctor Martijn Froeling, Professor James Clark, Professor Michael Langer, Professor Peter Savadjiev, Ryan Eckbo, Professor Hervé Lombaert, Professor Nathan Friedman, Professor Luc Devroye, Professor Joelle Pineau, Professor Adrian Vetta, Mr. Jan Binder, Mr. Nick Wilson and Ms. Marlene Gray. I also want to thank my former and current lab mates: Tabish Syed, Emmanuel Piuze, Chu Wang, Damien Goblot, Tristan Aumentado-Armstrong, Amir Kadivar, Pulkit Khandelwal, Aashima Singh, and Gabriel Downs and to wish them all the best for the future. During a major portion of my studies, I was a member of the NSERC CREATE-MIA program. I am very grateful to its wonderful administrator, Krys Dudek. I am particularly grateful to two of my best friends, Morteza Rezanejad and Bahareh Ghotbi, at the Center for Intelligent Machines at McGill University. I will always cherish memories of my time together with them. I want to thank several of my close friends who provided me great personal support: Elham Karimi, Arash Gholami, Behin Molaie, Ashkan Esmaeilnia, Damoon Daryadel, Shahab Bayani, Milad Kiaee, Abbas Sabzevari, Mohammad Hosseinnejad, Saman Rahimi, Hasan Mozaffari, Saeed Mohamadkhani, Elham Pourtaghi, and Mitra Aqaei. I am deeply grateful to my family, my father, Hossein, my mother, Tahereh and my brother Arash, for their constant support and for always believing in me. My deepest gratitude is to my beloved wife and my best friend, Pantea Ahmadi. She has always stood by me and supported me with her glowing spirit and beautiful smile.

Abstract

Recent advancements in medical imaging and image acquisition demand the development of novel analysis methods and algorithms so that appropriate geometric measurements can be made, information which may not be computable just from the raw data. Through diffusion magnetic resonance imaging, for example, we now have a way to infer the dominant orientation of fibrous structure in tissue, at the millimeter or sub-millimeter scales. Such measurements on their own do not answer more complex questions about fiber geometry, such as whether the fibers lie along specific surfaces, or how the fibers move in dynamic tissue. Motivated by such considerations, this thesis develops methods and algorithms to address two specific problems. First, given local measurements of fiber orientation, we develop and evaluate an algorithm to recover sheets on which these fibers lie, where appropriate. Second, given fiber orientation measurements in deforming tissue, we develop a moving frame method to recover local spatio-temporal signatures to capture how the fibers rotate.

Whereas the notions of sheets and cleavage plains have often been the subject of literature on myocardial tissue geometry, the potential sheet-like organization of fiber tract systems in the mammalian brain has been a topic of some controversy. We study the existence of sheet-like organization of fibers in biological tissues by introducing a framework that, from an oriented vector field representing local fiber directions, is capable of finding sheets on which they may lie. We apply our method to the cases of ventricular myofibers and brain tractograms to recover the sheet-like organizations using an efficiently imple-

mented algorithm. For both cardiac fibers and fiber tract systems in the mammalian brain, our method gives a principled approach to recover sheet-like geometries given a single dense direction field as input.

Past work on modeling fiber geometry has largely focused on the static case, so few models presently exist to provide geometric signatures to describe moving fibers. We contribute to this problem by extending past moving frame methods to the case of dynamic direction field data so that they are capable of measuring the rotation of cardiac fibers in a spatio-temporal setup. We validate our approach by providing proof of concept results on both simulated data, from a computational modeling challenge dataset of canine hearts, and on new in vivo human heart data.

Abrégé

Les progrès récents en imagerie médicale et en acquisition d'images exigent le développement de méthodes et d'algorithmes d'analyse novateurs permettant de réaliser des mesures géométriques appropriées, mesures qui peuvent ne pas être calculables uniquement à partir des données brutes. Grâce à l'imagerie par résonance magnétique par diffusion, par exemple, nous avons maintenant un moyen de déduire l'orientation dominante de la structure fibreuse des tissus, à l'échelle millimétrique ou submillimétrique. De telles mesures ne permettent pas à elles seules de répondre à des questions plus complexes sur la géométrie des fibres, par exemple si les fibres se trouvent le long de surfaces spécifiques ou comment les fibres se déplacent dans les tissus dynamiques. Motivée par de telles considérations, cette thèse développe des méthodes et des algorithmes pour répondre à deux questions spécifiques. Premièrement, étant donné les mesures locales d'orientation des fibres, nous développons et évaluons un algorithme permettant de récupérer les feuillets sur lesquelles reposent ces fibres, le cas échéant. Deuxièmement, étant donné les mesures d'orientation des fibres dans les tissus en déformation, nous développons une méthode à cadre mobile pour récupérer les signatures spatio-temporelles locales afin de capturer la rotation des fibres.

Alors que les notions de feuillets et de plans de clivage font souvent partie de publications sur la géométrie des tissus myocardiques, l'organisation en forme de feuillet des systèmes de faisceaux de fibres dans le cerveau des mammifères a fait l'objet de certaines controverses. Nous étudions l'existence d'une organisation en forme de feuillet de

fibres dans des tissus biologiques, en introduisant un paradigme qui, à partir d'un champ de vecteurs orienté représentant les directions locales des fibres, est capable de trouver les feuillets sur lesquels elles peuvent reposer. Nous appliquons notre méthode aux cas de myofibres ventriculaires et de tractogrammes cérébraux afin de récupérer les organisations en forme de feuillet, en utilisant un algorithme efficace. Notre méthode propose une approche basée sur des principes permettant de récupérer des géométries en forme de feuillet, à la fois pour des fibres cardiaques et des systèmes de tractus fibreux dans le cerveau.

Les travaux antérieurs sur la modélisation de la géométrie des fibres se sont largement concentrés sur le cas statique. Il existe donc actuellement peu de modèles permettant de fournir des signatures géométriques décrivant les fibres en mouvement. Nous contribuons à résoudre ce problème en étendant les méthodes de cadres mobiles précédents au cas des données de champ de direction dynamique, afin qu'elles soient capables de mesurer la rotation des fibres cardiaques dans une configuration spatio-temporelle. Nous validons notre approche en fournissant des résultats de validation du concept à la fois sur des données simulées, à partir d'un ensemble de données de modélisation informatique des coeurs canins, ainsi que sur des données in vivo du cœur humain.

Acronyms

3D	3 Dimensional
4D	4 Dimensional
CB	Cingulum Bundle
CC	Corpus Callosum
CPU	Central Processing Unit
CST	Cortico Spinal Tract
GPU	Graphics Processing Unit
dMRI	Diffusion Magnetic Resonance Imaging
DTI	Diffusion Tensor Imaging
DT-MRI	Diffusion Tensor Magnetic Resonance Imaging
EF	Ejection Fraction
FA	Fractional Anisotropy
GHM	Generalized Helicoid Model
HCP	Human Connectome Project
HVMB	Helical Ventricular Muscle Band

ICP	Inferior Cerebellar Peduncle
ILF	Inferior Longitudinal Fasciculus
LV	Left Ventricle
MCP	Middle Cerebellar Peduncle
MR	Magnetic Resonance
MRI	Magnetic Resonance Imaging
NMR	Nuclear Magnetic Resonance
NBD	Neighbourhood
OR	Optic Radiations
PDF	Probability Density Function
RV	Right Ventricle
SLF	Superior Longitudinal Fasciculus
UF	Uncinate Fasciculus
VMF	Von Mises-Fisher

Symbols

$\mathbb{R}^n$	Real coordinate space of dimension n
p	Point
$\mathbf{T}$	Tangent vector
$\mathbf{N}$	Normal vector
$\mathbf{B}$	Binormal vector
$\mathbf{a}, \mathbf{b}, \mathbf{u}, \mathbf{v}, \mathbf{V}, \mathbf{n}$	Vector fields
L	Lie bracket
$\frac{\partial}{\partial x^i}$	Partial derivative
$J_{\mathbf{a}}$	Jacobian of $\mathbf{a}$
$< \mathbf{a}, \mathbf{b} >$	Dot product of $\mathbf{a}$ and $\mathbf{b}$
$\mathbf{a}.\mathbf{b}$	Dot product of $\mathbf{a}$ and $\mathbf{b}$
$[\mathbf{a}, \mathbf{b}]$	Lie bracket of $\mathbf{a}$ and $\mathbf{b}$
$\mathbf{a} \times \mathbf{b}$	Cross product of $\mathbf{a}$ and $\mathbf{b}$
$curl\ \mathbf{a}$	Curl of $\mathbf{a}$
$\nabla_{\mathbf{v}}\mathbf{u}$	Gradient of $\mathbf{u}$ in direction of $\mathbf{v}$

ρ	Holonomicity
F	Local frame field
E	Global frame field
F^T	F transpose
F^t	F at time t
$\mathbf{e}_i, \mathbf{E}_i$	Basis for global frame
$\mathbf{f}_i$	Basis for local frame
$\omega(\mathbf{v})$	1-form operator on vector $\mathbf{v}$
$[\alpha_{ij}]$	Attitude matrix
$\wedge$	Wedge product operator
α	Helix angle of cardiac fibers
β'	Cardiac sheet angle
c_{ijk}	Cartan connection form parameter
$\theta(\mathbf{x}, t)$	Rotation of vector $\mathbf{x}$ at time t

Contents

List of Figures

List of Tables

1

Introduction

Oriented elements compose fibrous structures in biological tissue, and their geometry plays an important role in organ function. In the heart, for example, myocytes are stacked end on end in a particular fashion to facilitate electrical conductivity and efficient mechanical contraction. In the brain, white matter fiber tracts are neuro-anatomically partitioned into specific bundles that connect distinct brain regions. In both cases, the local geometry has been qualitatively described as being sheet-like in particular regimes. Yet, to date, few if any quantitative methods exist for finding these sheets from imaging data.

Our present understanding of heart wall fiber geometry also suffers from the limitation that it is based on ex vivo and hence static data, observed through diffusion imaging or histology. Thus, little is known about the manner in which fibers rotate or are locally displaced when the heart beats. Yet, the geometric organization of moving fibers in the heart wall is key to its mechanical function and to the distribution of forces within it to effect

efficient, repetitive pumping. Thus far, there has been little work on the computational modeling of moving fibers in biological tissue.

The first problem that this thesis addresses is that of, given an input vector field, finding a second one perpendicular to it with which it best spans a sheet-like structure locally. We develop a computational solution which is based on the iterative minimization of suitable energy functionals using gradient descent. Given a fixed vector field representing the input fiber direction, and starting from an arbitrary initialized moving vector field, we first directly consider the magnitude of the Lie bracket of the two vector fields as an energy function that indicates the local deviation from being sheet-like. We perturb the moving vector field iteratively in such a way that the energy reduces at each step throughout the entire volume, and illustrate this approach for finding sheets from cardiac ventricular diffusion data.

We then consider the related notion of non-holonomicity as the energy function which we once again aim to minimize directly. We show that this second approach leads to an algorithm which converges in theory and in practice, under reasonable assumptions on the input data, and we provide high quality sheet reconstructions from both heart wall DTI data and labeled tracts in the human brain, along with a sheet likeliness measure. Whereas sheet-like geometries have been described qualitatively in past literature, ours is the first method to provide a reconstruction of them from a single direction field.

The second problem addressed in this thesis is that of modeling moving fibers computationally. Starting with orthonormal vector fields which span the sheet-like structure of ventricular myocardium, we fit a frame field to the cardiac volume and then develop

a moving frame method to model geometric changes, with a spatio-temporal formulation of the associated Cartan matrix. This is a direct extension of the moving frame method developed for the case of static fibers, introduced in [66]. We apply our construction to simulated (canine) data obtained from the left ventricular mechanics challenge in STACOM 2014, and also to in vivo human left ventricular data. The method shows promise in providing Cartan connection parameters to describe spatio-temporal rotations of fibers, which in turn could benefit subsequent analyses or be used for diagnostic purposes.

In an application of this method, we consider the challenging problem of recovering fiber orientation from noisy diffusion data, such as that obtained from in vivo imaging of the heart. Recovering reliable fiber orientation from in vivo data is considerably difficult. To this end, we use a geometric approach, with a spatio-temporal Cartan frame field to model spatial (within time-frame) and temporal (between time-frame) rotations within a single consistent mathematical framework. The key idea is to calculate the Cartan structural connection parameters, and then fit probability distributions to these volumetric scalar fields. Voxels with low log-likelihood with respect to these distributions signal geometrical "noise" or outliers. With experiments on both simulated (canine) moving fiber data and on an in vivo human heart sequence, we demonstrate the promise of this approach for outlier detection and denoising via inpainting.

1.1 Objectives of the thesis

This thesis has two main objectives:

1. Given a vector field that is aligned with the orientation of fibrous structures in bio-

logical tissues, we aim to recover a second vector field such that it has the highest chance of spanning sheets in the tangent space to the fiber. To this end we:

- Define energy functions using the notion of the Lie bracket and non-holonomicity to locally quantify sheet-likeliness;
- Introduce a gradient-descent based energy minimization approach that from a given vector field, is capable of finding a second vector field perpendicular to it that spans sheets;
- Show that under certain constraints, the algorithm converges for the case of a non-holonomicity based energy;
- Develop an efficient and parallelizable, GPU-based implementation;
- Implement a method and a tool to visualize the fitted sheets, and the error of fit on the input volume; and
- Demonstrate the method on different samples of cardiac and brain data.

2. We aim to model the motion of myofibers in the left ventricle and quantify their rotation in the cardiac beat cycle. To this end we:

   - Extend the notion of connection forms from the static case in 3D [66] to the dynamic case (which is 4D) via the notion of spatio-temporal connection forms;
   - Consider the motion of material points in the dynamic case and introduce a parameterization to model it;
   - Utilize synthetic 4D cardiac simulation data to demonstrate a proof of concept result;

- Introduce a frame fitting model to the acquired in vivo cardiac data;
- Measure the rotation of cardiac fibers locally during the contraction phase for both human in vivo and canine simulation detests; and
- Propose a statistical model to find irregular oriented structures, based on a population of spatio-temporal connection forms and illustrate the method on both simulation and real data.

1.2 Publications arising from this thesis

Finding sheets in biological tissues

- **(Conference)** Syed, Tabish A., Babak Samari, and Kaleem Siddiqi. "Estimating Sheets in the Heart Wall." In International Workshop on Statistical Atlases and Computational Models of the Heart, pp. 3-11. STACOM 2018, Granada, Spain. Lecture Notes in Computer Science, vol 11395, Springer.
- **(Conference)** Samari, Babak, Tabish A. Syed, and Kaleem Siddiqi. "Minimizing Non-holonomicity: Finding Sheets in Fibrous Structures." In International Conference on Information Processing in Medical Imaging, pp. 183-194. IPMI 2019, Hong Kong. Lecture Notes in Computer Science, vol 11492, Springer.

Babak Samari, Tabish Syed: Contributed equally to the design and implementation of the energy minimization algorithms, on implementing the visualization pipeline, on the proof of convergence, and on writing the article.

1.2 Publications arising from this thesis

Kaleem Siddiqi: Contributed to methodological development, writing, and interpretation of results.

Moving frames for moving fibers

- **(Conference)** Samari, Babak, Tristan Aumentado-Armstrong, Gustav Strijkers, Martijn Froeling, and Kaleem Siddiqi. "Cartan Frames For Heart Hall Fiber Motion.", Functional Imaging and Modelling of the Heart, pp. 32-41. FIMH 2017, Toronto, Canada. Lecture Notes in Computer Science, vol 10263, Springer.
- **(Conference)** Samari, Babak, Tristan Aumentado-Armstrong, Gustav Strijkers, Martijn Froeling, and Kaleem Siddiqi. "Denoising Moving Heart Wall Fibers Using Cartan Frames." In International Conference on Medical Image Computing and Computer-Assisted Intervention, pp. 672-680. MICCAI 2017, Quebec City, Canada. Lecture Notes in Computer Science, vol 10433, Springer.

Babak Samari: Lead this work. Developed and implemented the spatio-temporal algorithms and the visualization pipeline, and carried out the majority of the writing.
Tristan Aumentado-Armstrong: Assisted with the processing of the canine simulation data, and helped with writing.
Gustav Strijkers and Martijn Froeling: Lead the in vivo cardiac imaging and helped with writing and interpretation of results.
Kaleem Siddiqi: Contributed to methodological development, writing, and interpretation of results.

1.3 Additional publications

In the course of my doctoral studies, I was fortunate to be able to collaborate actively with colleagues of mine in the Shape Analysis group at McGill University. This lead to several publications on which I am a co-author, but which are not in the area of focus of my thesis.

- **(Conference)** Rezanejad, Morteza, Babak Samari, Ioannis Rekleitis, Kaleem Siddiqi, and Gregory Dudek. "Robust Environment Mapping Using Flux Skeletons." In 2015 IEEE/RSJ International Conference on Intelligent Robots and Systems (IROS), pp. 5700-5705. IEEE, 2015.

Morteza Rezanejad: Lead this work, contributing to the design and implementation of the algorithms, and carrying out the majority of the writing.
Babak Samari: Contributed to the design and implementation of the algorithms, and to writing the article.
Ioannis Rekleitis, Kaleem Siddiqi, and Gregory Dudek: Contributed to methodological development, writing and interpretation of results.

- **(Conference)** Wang, Chu, Babak Samari, and Kaleem Siddiqi. "Local Spectral Graph Convolution For Point Set Feature Learning." In Proceedings of the European Conference on Computer Vision (ECCV), pp. 52-66. 2018.

Chu Wang: Lead this work, contributing to the design and implementation of the algorithms, and carrying out the majority of the writing.

Babak Samari: Contributed to the designing and implementation of the algorithms, and to writing the article.

Kaleem Siddiqi: Contributed to, methodological development, writing, and interpretation of results.

1.4 Organization of the thesis

This thesis is organized into three main parts. A schematic organization of its contents is presented in Figure 1.1. First, in Part I, we start by providing a review of relevant background. In Chapter 2, we briefly review mathematical topics, in particular, the Lie bracket, holonomicity, and differential forms, all of which are relevant to the main contributions of the thesis. Then, in Chapter 3, we review a selection of literature on the geometry of fibrous structures. In Part II, we start by reviewing sheet-like organizations in the brain and in the heart in Chapter 4. Then, in Chapter 5, we develop iterative algorithms that from an input vector field tangent to the direction of fibers, find a second vector field such that the two span sheets. Later, in Chapter 6, we demonstrate sheet fitting algorithms on cardiac ex vivo and brain in vivo datasets. Chapters 7, 8, and 9 of Part III focus on modeling the motion of fibers during the cardiac beat cycle. Here, we develop a spatio-temporal framework to describe this motion using the notion of connection forms. We demonstrate that this model is capable of measuring the rotation of myofibers during the contraction phase for both simulation and in vivo data. We then, specialize in the application of this model and show how it can be useful in distinguishing noise and irregular structures. Finally, in Chapter 10, we summarize the findings and contributions of this dissertation and discuss

1.4 Organization of the thesis

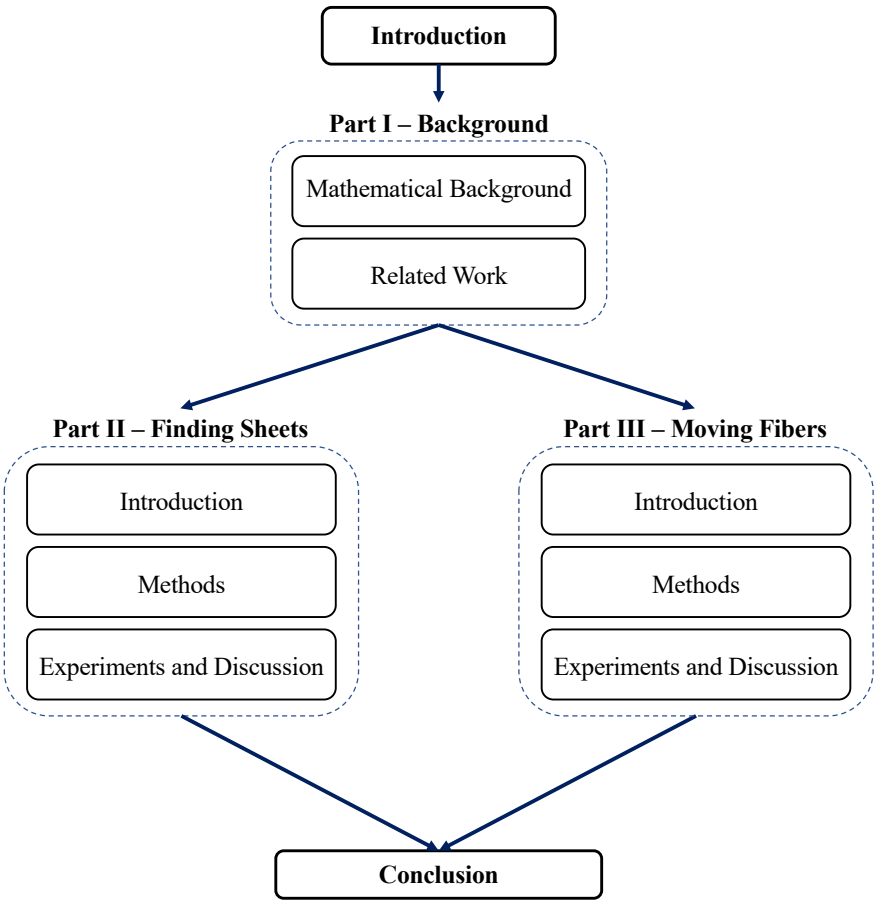

Figure 1.1: Organization of the thesis.

directions for future work.

Part I

Part I: Background

2

Mathematical Background

In this chapter we provide a mathematical background that is relevant to the sheet finding and fiber geometry modeling approaches developed later in this thesis. In particular, we review concepts related to the Lie Bracket, differential forms and texture flows. The reader familiar with these subjects may proceed directly to Chapter 3.

2.1 The Lie Bracket and non-holonomicity

Given two smooth vector fields $\mathbf{a}$ and $\mathbf{b}$ on a manifold M, the Lie bracket $\mathbf{L} = [\mathbf{a}, \mathbf{b}]$ is their commutator. With f a smooth function defined on M the commutator acts on f as follows:

$$L(f) = \mathbf{a}(\mathbf{b}f) - \mathbf{b}(\mathbf{a}f).$$

2.1 The Lie Bracket and non-holonomicity

In Cartesian coordinates we let $\mathbf{a} = a_i \dfrac{\partial}{\partial x^i}$ and $\mathbf{b} = b_i \dfrac{\partial}{\partial x^i}$ (with summation implied over repeated indices). The Lie bracket is then given by

$$L = \left(a_j \frac{\partial b^i}{\partial x^j} - b_j \frac{\partial a^i}{\partial x^j} \right) \frac{\partial}{\partial x^i}.$$

Therefore, given vector fields $\mathbf{a}$ and $\mathbf{b}$, we have

$$L = J_{\mathbf{b}}\mathbf{a} - J_{\mathbf{a}}\mathbf{b}, \tag{2.1}$$

where, $J_{\mathbf{a}}$ and $J_{\mathbf{b}}$ are the Jacobians of $\mathbf{a}$ and $\mathbf{b}$, respectively. In Cartesian coordinates the Jacobian of $\mathbf{a}$ is defined as

$$J_{\mathbf{a}} = \begin{pmatrix} \dfrac{\partial a^1}{\partial x^1} & \dfrac{\partial a^1}{\partial x^2} & \dfrac{\partial a^1}{\partial x^3} \\ \dfrac{\partial a^2}{\partial x^1} & \dfrac{\partial a^2}{\partial x^2} & \dfrac{\partial a^2}{\partial x^3} \\ \dfrac{\partial a^3}{\partial x^1} & \dfrac{\partial a^3}{\partial x^2} & \dfrac{\partial a^3}{\partial x^3} \end{pmatrix}. \tag{2.2}$$

Given the two vector fields $\mathbf{a}$ and $\mathbf{b}$, we estimate the value of $\mathbf{L}$, which is itself a vector field, using Equation (2.1). This equation gives the Lie bracket an interpretation as the vector displacement while moving along a parallelogram spanned by $\mathbf{a}$ and $\mathbf{b}$ at a point. In other words, we start at the point p and then move along streamlines of $\mathbf{a}$, $\mathbf{b}$, $-\mathbf{a}$ and then $-\mathbf{b}$. The vector displacement to p is the Lie bracket. The magnitude of $\mathbf{L}$ at a point p can therefore be used as a measure of deviation from a sheet spanned locally by fields $\mathbf{a}$ and $\mathbf{b}$, around p. For vector fields spanning sheets, we expect the parallelograms to close, and therefore the magnitude of the Lie bracket to be zero. A similar construction based

on the Lie bracket is used by Tax et al. [86] to estimate sheet probability in the brain from diffusion data. In Chapter 5, we shall define an energy based on the L^2 norm of the Lie bracket in a local neighbourhood $N(p)$ of point p. Then, given $\mathbf{a}$, we shall estimate the vector field $\mathbf{b}$ that minimizes this energy at every point in space, while constraining the solution space to vectors $\mathbf{b}$ in the plane perpendicular to $\mathbf{a}$. Figure 2.1 illustrates the Lie bracket operation on two arbitrary vector fields.

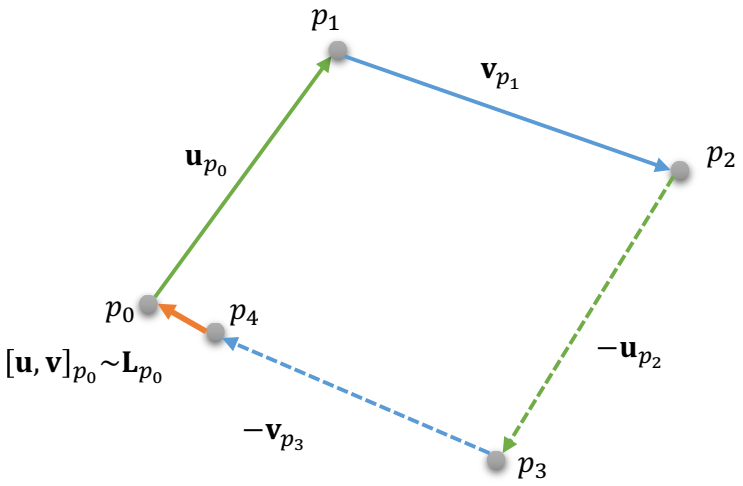

Figure 2.1: Conceptual illustration of the Lie bracket operation between two vector fields u and $\mathbf{v}$, at point p_0. See text for a discussion.

Theorem 1 *Given a unit vector field* $\mathbf{n}$ *which is orthonormal to a family of surfaces, it can be shown that* $\langle \mathbf{n}, \operatorname{curl} \mathbf{n} \rangle = 0$ *[102], where we use* $\langle \cdot, \cdot \rangle$ *to denote the inner product. Conversely, any vector field* $\mathbf{n}$ *such that* $\langle \mathbf{n}, \operatorname{curl} \mathbf{n} \rangle = 0$ *is orthonormal to a family of surfaces and is said to be* holonomic.

For a general vector field $\mathbf{n}$, its degree of non-holonomicity ρ is defined as follows

[102]:

$$\rho = \Big\langle \mathbf{n}, \operatorname{curl} \mathbf{n} \Big\rangle.$$

Consider two orthonormal vector fields $\mathbf{u}$ and $\mathbf{v}$ such that $\mathbf{n} = \mathbf{u} \times \mathbf{v}$. It is easy to show then, that *non-holonomicity* ρ expressed in terms of $\mathbf{u}$ and $\mathbf{v}$ reduces to

$$\rho^{\mathbf{uv}} = \Big\langle \mathbf{u} \times \mathbf{v},\ [\mathbf{u}, \mathbf{v}] \Big\rangle,$$

where $[\mathbf{u}, \mathbf{v}]^i = u^j \frac{\partial v^i}{\partial x^j} - v^j \frac{\partial u^i}{\partial x^j}$ is the Lie Bracket of $\mathbf{u}$ and $\mathbf{v}$.

2.2 Differential forms

We provide a brief overview of differential forms since they will later be used in our discussion of moving frame methods for modeling fibers. In particular, differential forms are essential to comprehend the notion of Cartan connections, used by Piuze et al. [66] to describe the static rotation of cardiac fibers locally as described in Section 3.5. We further extend it to model the motion of fibers both in space and time in Part III of this thesis.

Definition 1 *Let* $(\mathbb{R}^n)^*$ *be a set of linear maps* $\psi : \mathbb{R}^n \to \mathbb{R}$ *referred to the dual space of* $\mathbb{R}^n$ *and* $\Lambda^k(\mathbb{R}^n)^*$ *be maps of alternating, and multi-linear* k *vectors in* $\mathbb{R}^n$ *to* $\mathbb{R}$*. Then, a k-form is a map* $\omega : \underbrace{\mathbb{R}^n \times \cdots \times \mathbb{R}^n}_{k \text{ times}} \to \Lambda^k(\mathbb{R}^n)^*$

Note 1 *Given a k-form* $\omega : \underbrace{\mathbb{R}^n \times \cdots \times \mathbb{R}^n}_{k \text{ times}} \to \mathbb{R}$*, and* $\mathbf{v}_i$*s as vectors in* $\mathbb{R}^n$*,* $1 \leqslant \forall i \leqslant k$*:* ω *is:*

1. *alternating if:* $\omega(\mathbf{v}_1, \ldots, \mathbf{v}_i, \ldots, \mathbf{v}_j, \ldots, \mathbf{v}_k) = -\omega(\mathbf{v}_1, \ldots, \mathbf{v}_j, \ldots, \mathbf{v}_i, \ldots, \mathbf{v}_k)$.
2. *multi-linear if:* ω *is linear for all of its inputs, i.e.:*
   - $\omega(\mathbf{v}_1, \ldots, c\mathbf{v}_i, \ldots, \mathbf{v}_k) = c\omega(\mathbf{v}_1, \ldots, \mathbf{v}_i, \ldots, \mathbf{v}_k)$,
   - $\omega(\mathbf{v}_1, \ldots, \mathbf{v}_i + v_i', \ldots, \mathbf{v}_k) = \omega(\mathbf{v}_1, \ldots, \mathbf{v}_i, \ldots, \mathbf{v}_k) + \omega(\mathbf{v}_1, \ldots, v_i', \ldots, \mathbf{v}_k)$.

Therefore, a k-form is an alternating, multi-linear operator on k vectors where each vector is in $\mathbb{R}^n$. Now, we define a basis for these k-forms in the following:

2.2 Differential forms

Let $i_1, \ldots, i_k$ be k numbers between 1 and n and let $\mathbf{v}_j$s be vectors in $\mathbb{R}^n$; then, we define:

$$dx_{i_1,\ldots,i_k}(\mathbf{v}_1, \ldots, \mathbf{v}_k) = det \begin{bmatrix} \mathbf{v}_{1i_1} & \ldots & \mathbf{v}_{1i_k} \\ \vdots & \ddots & \vdots \\ \mathbf{v}_{ki_1} & \ldots & \mathbf{v}_{ki_k} \end{bmatrix}. \tag{2.3}$$

To simplify notation, let $dx_{i_1,\ldots,i_k}$ refer to $dx_{i_1,\ldots,i_k}(\mathbf{v}_1, \ldots, \mathbf{v}_k)$. Using the definition of the determinant, we know that $dx_{i_1,\ldots,i_k}$ is multi-linear and alternating. We also see that for any two numbers $h, l \in \{1, \ldots, k\}$ where $h \neq l$ and $i_h = i_l$, $dx_{i_1,\ldots,i_k}$ would be equal to zero. Moreover, if we swap i_h with i_l, we get the negative sign for $dx_{i_1,\ldots,i_k}$. These leads to the idea of defining a basis for k-forms. Assuming $I = i_1, \ldots, i_k$ where $i_j \in \{1, \ldots, n\}, i_1 < \cdots < i_k$, Shifrin [79] shows that $\{dx_I\}$ is a basis for $\Lambda^k(\mathbb{R}^n)^*$, i.e. elements of $\{dx_I\}$ are linearly independent and they span $\Lambda^k(\mathbb{R}^n)^*$. Considering $\{dx_I\}$ as a basis for $\Lambda^k(\mathbb{R}^n)^*$, we can summarize a k-form ω as:

$$\omega = \sum_I a_I dx_I \tag{2.4}$$

where the a_Is, also known as 0-forms, are shortcuts for $a_I(x_1, \ldots, x_n)$, which are real valued functions in $\mathbb{R}^n$. A k-form is called differentiable if a_I are differentiable functions.

We define a wedge product as an operator: $\wedge : \Lambda^k(\mathbb{R}^n)^* \times \Lambda^l(\mathbb{R}^n)^* \rightarrow \Lambda^{k+l}(\mathbb{R}^n)^*$. In order to formulate the wedge product, we first define how it works on the basis of $\Lambda^k(\mathbb{R}^n)^*$

and $\Lambda^l(\mathbb{R}^n)^*$. Assume $I = i_1, \ldots, i_k$ and $J = j_1, \ldots, j_l$ where $i_m, j_m \in \{1, \ldots, n\}$:

$$dx_I \wedge dx_J = dx_{I,J} \tag{2.5}$$

where J has been concatenated to I. Now considering Equations (2.4) and (2.5), a wedge product on a k-form:$\sum_I a_I dx_I$ and an l-form:$\sum_J b_J dx_J$ can be applied by wedging the corresponding dx_I and dx_J according to the Equation (2.5) and multiplying corresponding real function coefficients a_I, b_J.

Note 2 *Let $\Phi \in \Lambda^k(\mathbb{R}^n)^*$, $\Psi \in \Lambda^l(\mathbb{R}^n)^*$ and $\Omega \in \Lambda^h(\mathbb{R}^n)^*$, Shifrin [79] shows that the wedge product has the following properties:*

- *skew-communicative, i.e.* $\Phi \wedge \Psi = (-1)^{kl} \Psi \wedge \Phi$
- *associative, i.e.* $(\Phi \wedge \Psi) \wedge \Omega = \Phi \wedge (\Psi \wedge \Omega)$
- *distributive, e.g.* $(\Phi + \Psi) \wedge \Omega = \Phi \wedge \Omega + \Psi \wedge \Omega$

As has been shown in Equation (2.4), $a_I(x_1, \ldots, x_n)$s are real functions in $\mathbb{R}^n$. From differential calculus, we know that derivative of a function in $\mathbb{R}^n$ is a summation of its partial-derivatives, i.e. $da_I = da_I(x_1, \ldots, x_n) = \sum_{j=1}^n \frac{\partial a_I}{\partial x_j} dx_j$. Thus, we now can define the derivative of a k-form ω in $\mathbb{R}^n$ as the following:

$$d\omega = \sum_I da_I \wedge dx_I \tag{2.6}$$

which is a (k+1)-form in $\mathbb{R}^n$.

2.2 Differential forms

Now that we have defined basic notations for differential forms, we specialize to the space of $\mathbb{R}^3$. In 3D Cartesian space, where $x = x_1, y = x_2, z = x_3$, the following statements are true:

- A 0-form is a function f in $\mathbb{R}^3$
- A 1-form is $fdx + gdy + hdz$
- A 2-form is $fdxdy + gdydz + hdxdz$
- A 3-form is $fdxdydz$
- $(k > 3)$-forms are zero (since an element dx, dy or dz needs to repeat more than once).

In this thesis, we shall use the notion of 1-forms and their properties in Part III, to model the motion of cardiac myofibers in a spatio-temporal setup.

2.3 Texture flows, helicoids and moving frames for modeling fibers

We briefly review the current literature on the use of frame fields attached to curve data, for modeling texture flows in computer vision and image analysis. This development is at the heart of the use of the helicoid for texture flow analysis [8]. These methods were later extended to 3D and used for modeling fiber tracts in diffusion MRI in the brain via the notion of the generalized helicoid [73, 74]. We shall briefly discuss these developments and then also show the connection to more general (model-free) moving frame methods for fiber geometry [65], which provide a foundation for the results of Part III of this thesis.

Definition 2 *A curve in* $\mathbb{R}^3$ *is defined as a differentiable function* $\gamma : (a, b) \rightarrow \mathbb{R}^3$ *where* $a, b \in \mathbb{R}$. *The speed function of a curve is then defined as* $\rho(t) = \|\gamma'(t)\|$.

We refer to a curve as a unit speed curve if $\forall t \in (a, b) : \|\gamma'(t)\| = 1$. O'Neill [60] shows that there exists a parametrization β for an arbitrary curve γ where β is a unit speed curve.

Definition 3 *Let* $\mathbb{O} \subset \mathbb{R}^3$ *then:*

- *A vector field* $\mathbf{E}$ *on* $\mathbb{O}$ *is defined as a function that assigns to each point* $p \in \mathbb{O}$ *a tangent vector* $\mathbf{V}(p)$

2.3 Texture flows, helicoids and moving frames for modeling fibers

- *Let* $\mathbf{E}_1, \mathbf{E}_2, \mathbf{E}_3$ *be 3 vector fields on* $\mathbb{O}$*. They. build a frame field if:*

$$\forall p \in \mathbb{O}, 1 \leqslant i, j \leqslant 3 : \mathbf{E}_i \cdot \mathbf{E}_j = \begin{cases} 1 & i = j \\ 0 & i \neq j. \end{cases}$$

Note 3 *We can now define a vector field on a curve* $\gamma : (a, b) \to \mathbb{R}^3$ *as a function that assigns to each number* $t \in (a, b)$ *a tangent vector* $\mathbf{T}$ *at the point* $\gamma(t)$*.*

We define 3 important vector fields on a curve as follows:

Definition 4 *Let* $\beta : (a, b) \to \mathbb{R}^3$ *be a unit speed curve (i.e.* $\forall s \in (a, b) : \|\beta'(s)\| = 1$*), then:*

1. $\mathbf{T} = \beta'$ *is a unit tangent vector field on* β*.*
2. *Assuming that* $\mathbf{T}$ *is differentiable,* $\mathbf{T}'$ *is called a curvature vector field on* β*,* $\kappa(s) = \|\mathbf{T}'(s)\|$ *is called a curvature function on* s*, and* $\mathbf{N} = \frac{\mathbf{T}'}{\kappa(s)}$ *is called a principal normal vector field.*
3. $\mathbf{B} = \mathbf{T} \times \mathbf{N}$ *is called a binormal vector field.*

These 3 vector fields are orthogonal to each other and form a frame field on a curve, known as the Frenet frame field [60]. Ben-Shahar and Zucker [8] review the organization of 2D texture flows using a Frenet frame field. Informally, a 2D texture flow can be defined as a "two-dimensional structure characterized by local parallelism and slowly varying dominant local orientation" or a set of curves which are dense and locally parallel to each other [8]. Let $q \in \mathbb{R}^2$ be an arbitrary point on a texture flow. The local behavior of a texture

flow can be looked at on a frame field $\mathbf{E_T}, \mathbf{E_N}$ at q where $\mathbf{T}, \mathbf{N}$ are tangent and normal vectors of a texture flow at the point q. Figure 2.2 shows a texture flow as a frame field of $\mathbf{E_T}, \mathbf{E_N}$. An orientation function $\theta(x, y)$ is defined on the neighborhood of the point q, and then the surface $s(x, y) = (x, y, \theta(x, y))$ in $XY\theta$ is parametrized. In the following, we introduce definitions and formulations used for surface geometry.

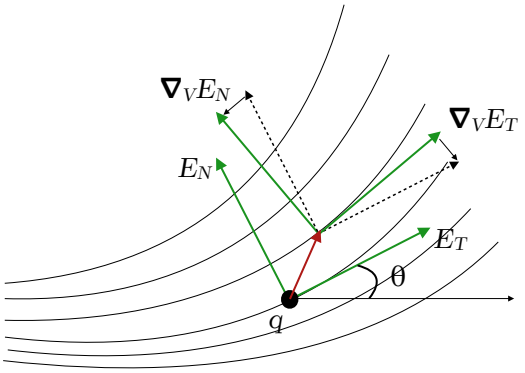

Figure 2.2: Illustration of texture flow using tangent and normal frames (adapted from Ben-Shahar and Zucker [8]).

Definition 5 *Assume* $\mathbf{M} \subset \mathbb{R}^3$ *is a surface and* p *is a point on* $\mathbf{M}$ *and* $\mathbf{U}$ *is a unit normal vector field on* M*:*

1. *If we let* $\mathbf{v}$ *be a tangent vector to* $\mathbf{M}$ *on* p*, then* $S_p(\mathbf{v}) = -\nabla_{\mathbf{v}}\mathbf{U}$ *is called the shape operator of* $\mathbf{M}$ *at* p*.*
2. *If we let* $\mathbf{u}$ *be a unit tangent vector to* $\mathbf{M}$ *on* p*, then the number* $k_p(\mathbf{u}) = S_p(\mathbf{u}).\mathbf{u}$ *is called normal curvature of* M *at* p *in the* u *direction.*

3. $k_{1p} = \arg\min_{\mathbf{u}} k_p(\mathbf{u})$ *and* $k_{2p} = \arg\max_{\mathbf{u}} k_p(\mathbf{u})$ *are defined as the principal curvatures of* $\mathbf{M}$ *at* p.

4. $H_p = \frac{k_{1p}+k_{2p}}{2}$ *is called the mean curvature of* $\mathbf{M}$ *at* p.

5. M *is defined as a minimal surface if* $\forall p \in \mathbf{M} : H_p = 0$ *i.e.* $\forall p \in \mathbf{M} : k_{1p} = -k_{2p}$.

Note 4 *A normal curvature of a surface at a point* p, *(*$k_p(\mathbf{u})$*), should not be confused with the normal curvature of a flow which measures change in the texture flow in the direction of* $\mathbf{E_N}$.

Ben-Shahar and Zucker [8] show that if $\triangle\theta = 0$ (i.e. θ is a harmonic function) and $s(x, y)$ is a minimal surface, then the frame field has the property of "slowly varying dominant local orientation". Furthermore, the plane and the helicoid surfaces are the only surfaces that are both harmonic and minimal. Equation (2.7) describes the geometry of a helicoid surface:

$$\theta(x, y) = \tan^{-1}(\frac{y}{x}) + C. \tag{2.7}$$

Without loss of generality, let us assume that $q = (0, 0)$ and $\theta(0, 0) = 0$ (i.e. frame $\mathbf{E_T}, \mathbf{E_N}$ is aligned with a global coordinate system). Then we have:

$$\nabla_{\mathbf{v}}\theta(0, 0) = (\nabla_{\mathbf{v}}\mathbf{E_T}, \nabla_{\mathbf{v}}\mathbf{E_N}) = (\mathbf{K_T}, \mathbf{K_N}). \tag{2.8}$$

Combining Equations (2.7) and (2.8) and simplifying them results in the following equation for $\theta(x, y)$:

$$\theta(x, y) = \tan^{-1}(\frac{\mathbf{K_T}x + \mathbf{K_N}y}{1 \pm (\mathbf{K_N}x - \mathbf{K_T}y)}). \tag{2.9}$$

The '$\pm$' sign in Equation (2.9) gives us two different solutions known as the "right helicoid" model for the '$+$' sign and the "left helicoid" model for the '$-$' sign. Considering the definition of $\mathbf{K_T}, \mathbf{K_N}$, Ben-Shahar and Zucker [8] verified that among these solutions, the right helicoid model is the only one with a constant ratio of curvatures (i.e. $\exists C \in \mathbb{R}, \forall q : \frac{\mathbf{K_T}(q)}{\mathbf{K_N}(q)} = C$); thus, it is the simplest model in terms of co-variation of $\mathbf{K_T}$ and $\mathbf{K_N}$.

Savadjiev et al. [73, 74, 75] extended the 2D frame by in the helicoid model by adding the binormal basis, $\mathbf{B}$, to form a 3D cartesian space. They showed that in this setup, the right helicoid model $\theta(x, y)$ could be generalized to $\theta(x, y, z)$ by adding a linear component $\mathbf{K_B}z$ to the Equation (2.9). Then, they argued that the myofibers of the left ventricles can be fitted to this model. For more detail review of this model please refer to Section 3.4.

It can be shown that θ is a 1-form operator [8], i.e., it is alternating and multi-linear. Based on this observation and inspired by the notion Connection forms [10], Piuze et al. [66, 65] further extend this idea by modeling the local rotation of frame fields via 9 connection form scalars. Using these connection forms, they modeled the rotation of cardiac myofibers by fitting a local coordinate system to them based on the extrinsic geometry of the heart. The connection form model has more degrees of freedom than the generalized helicoid model. We shall review this model in Section 3.5 as it is an essential component to Part III of this thesis.

3

Related Work

3.1 Biology of cardiac ventricles

A good deal is known about the structure of the mammalian heart and its wall (Figure 3.1). Past accounts, including [29, 84], report that coronorary arteries and veins are located in the direction along the epicardial surface. To carry nutrition to the deeper cells in the heart wall, blood vessels are organized transmurally. While myocardial capillaries are typically parallel to the long axis of the myocytes, vessels that connect myocardial capillaries to the veins pass-through muscle layers [82]. In a healthy human heart, the average Ejection Fraction (EF), which refers to the percentage of the blood pumping out from the left ventricle (LV) during systole, is measured to be more than 50%. This indicates that at least half of the ventricular blood volume passes through vessels in each cardiac phase. This phenomenon is facilitated by an electrical signal diffused by calcium entry and derived by local motion and rearrangement of myocytes [82].

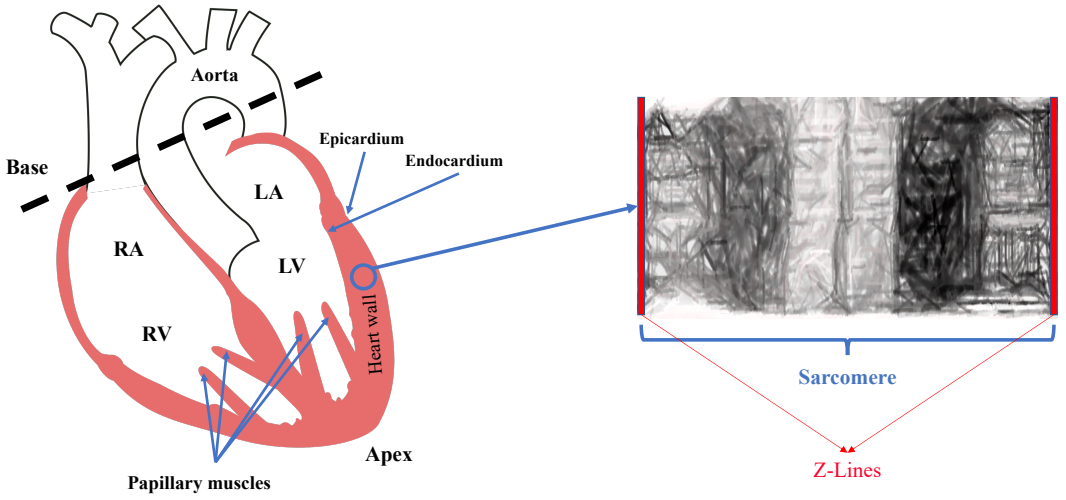

Figure 3.1: **Left:** A schematic of the anatomy of the human heart. LV stands for the left ventricle, RV stands for the right ventricle, LA stands for left aorta and RA stands for right aorta (adapted from Wikipedia contributors [100])). **Right:** Illustration of a typical muscle sarcomere bounded by z-lines, which are shown in red (adapted from Ohtsuki [59]).

As illustrated in Figure 3.1, cardiac ventricular walls are comprised of myocytes which themselves contain sarcomeres, which are the contractile elements. The myocytes change shape during the muscle contraction phase [59, 50]. Studies indicate that the maximum length of a cardiac sarcomere under physiologic stretch is bounded by 2.25 microns, compared to its minimum length of 1.5 microns. Therefore, cardiac mechanics are affected by the contraction of these cells, with the maximum shortening being about one-third in length. In typical cases, though the shortening is between one-fifth and one-tenth in length [82]. Measurements via quantitative electron microscopy indicate that these changes in length are not uniform throughout the heart wall and the change increases moving from the epicardial to the endocardial wall. A comprehensive study on canine hearts suggests that mid-wall shortening of sarcomeres by only 13% is what drives the entire cardiac

motion [30].

Quantification of the functionality of the cardiac ventricles can help in the diagnosis of cardiac diseases and evaluation of invasive cardiac procedures [15, 42, 72]. For instance, Ejection Fraction (EF), is a very widely used clinical standard to evaluate the health of the heart. To this end, different imaging modalities including echocardiography, ultrasound, and MRI sought to unravel the previously unknown structure and function of the LV. There are at least two different properties that make such analyses difficult. First, as illustrated in Figure 3.2, the LV is likely the most structurally complex region of the heart. It consists predominantly of fibrous structures that are geometrically non-symmetric. Regimes of myocytes at the cellular level are organized end on end, with each myocyte containing central nuclei and branches which connect them to a number of neighboring cells. This complex of attached myocytes to form elongated structures is referred to as a myofiber in the literature [82, 45]. These structures of interest are accompanied by fat, nerves, veins, arteries and lymphatics [97], which makes their analysis even more challenging. Second, the heart is not static but rather is a rapidly moving organ, which unlike other organs such as the lungs, cannot be easily stabilized in a living subject for in vivo imaging purposes. Static analysis of the heart and particularly the LV is usually possible only ex vivo. Unfortunately, such studies cannot directly reveal many details regarding cardiac contraction, particularly the change in the geometry of myofibers as the heart beats. What makes the analysis of cardiac motion at a micro level even more complicated, is the motion of the entire heart. Near the valves and the base of the heart, the organ is attached, while its apex is free to move, and other moving organs including the lungs can affect its shape during its contraction. Thus, isolating the shape changes in the heart wall that are purely

due to the contraction of myocytes, is not easy.

3.1.1 Ellipsoidal model

We now review the ellipsoidal model of the heart wall, that has been used to facilitate the characterization of geometric changes [77]. The LV has a unique geometric shape. While other muscles exhibit an elongated stacking of muscle cells, as shown in Figure 3.3, the LV can be described as being bounded by two ellipsoids with a ratio of $2/1$ corresponding to long/short axis lengths [82]. The early models approximate the global geometry of the heart by assuming uniform wall thickness along the axes of the ellipsoids. However, in reality, there is a variation in the thickness of the heart wall from base to the apex. As shown in Figure 3.2, the LV wall is much thinner closer to the apex and it does not have a uniformly varying curvature moving to the base.

The twisting motion of the LV during the contraction phase [82] demands specialized attention in the study of myofiber arrangement and the dynamics of cardiac contraction. Simple models of cardiac contraction, such as the ellipsoidal model, usually assume a symmetric torsion-free motion for a myofiber across the LV during the systolic phase. Studies of electrical activation through electrophysiology as well as NMR tagging, have revealed limitations of this assumed motion [47, 38, 42]. In addition, the adjacency of other structures makes the study of cardiac contraction even more challenging. For instance, papillary muscles and mitral valves work together to control and time the blood flow into the LV volume. Therefore the orientation of sarcomeres and fibers of papillary muscles are different from that of LV myofibers.

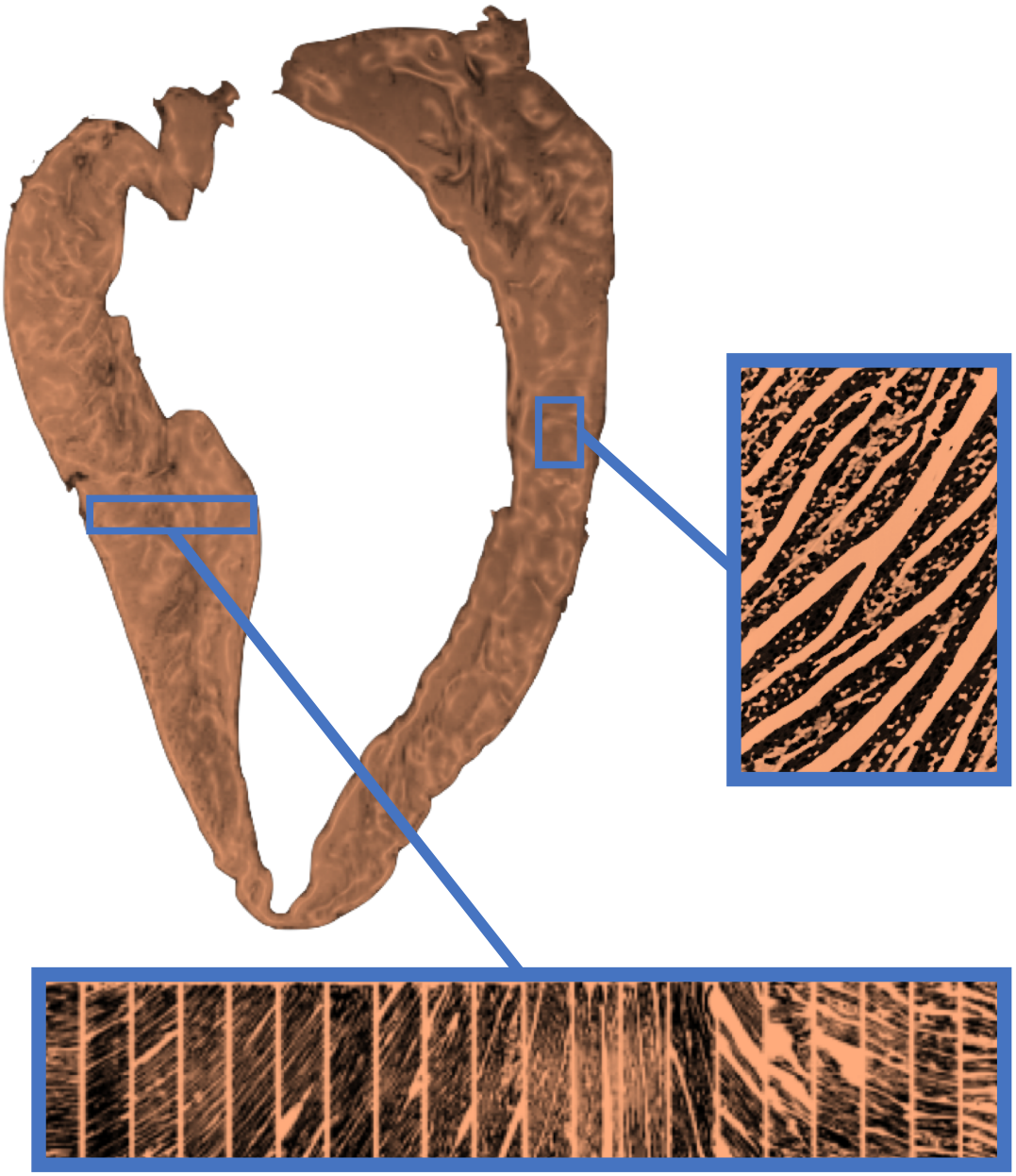

Figure 3.2: Arrangement of myocytes in the left ventricle of a canine image. **Left:** a longitudinal slice of the LV to demonstrate the change in the curvature of the wall from base (top of the heart) to apex (bottom of the heart). **Right:** arrangement of myocytes in the longitudinal section of LV and **Bottom:** along the short axis slice from epicardium to endocardium (adapted from Spotnitz [82]).

Spherical coordinate system

A global reference cardiac coordinate system can be defined with respect to the ellipsoidal model according to the spherical orthonormal bases: the long axis, the radial axis and the circumferential or the short axis of the ellipsoid. As illustrated in Figure 3.3, these axes form three orthonormal planes which are often referred to in the literature:

- The transverse or circumferential plane spanned by the radial and the circumferential (short) axes.
- The axial or transmural plane spanned by the radial and the long axes.
- The tangential plane spanned by the long and circumferential (short) axes.

Two ellipsoids with overlapping axes resemble the surfaces of the epicardium and the endocardium, respectively. This approach of modeling the LV has the advantage that describing the geometry and mechanics of the LV easy with respect to the global coordinate axes, is straightforward. For instance, considering a short axis slice of this model at the beginning of the contraction phase (end-diastole) versus the one at the end of the contraction phase (end-systole) can help us better understand how global geometry changes. Moreover, NMR tagging measurements of a short axis slice of the heart wall demonstrates a 36% thickening of it during the contraction phase [82].

Fiber/Helix angle

If we assume a uniform cylindrical (constant) volume for the LV, the 13% sarcomeric shortening or fiber shortening [84] implies an increase of myocyte thickness by only 6%.

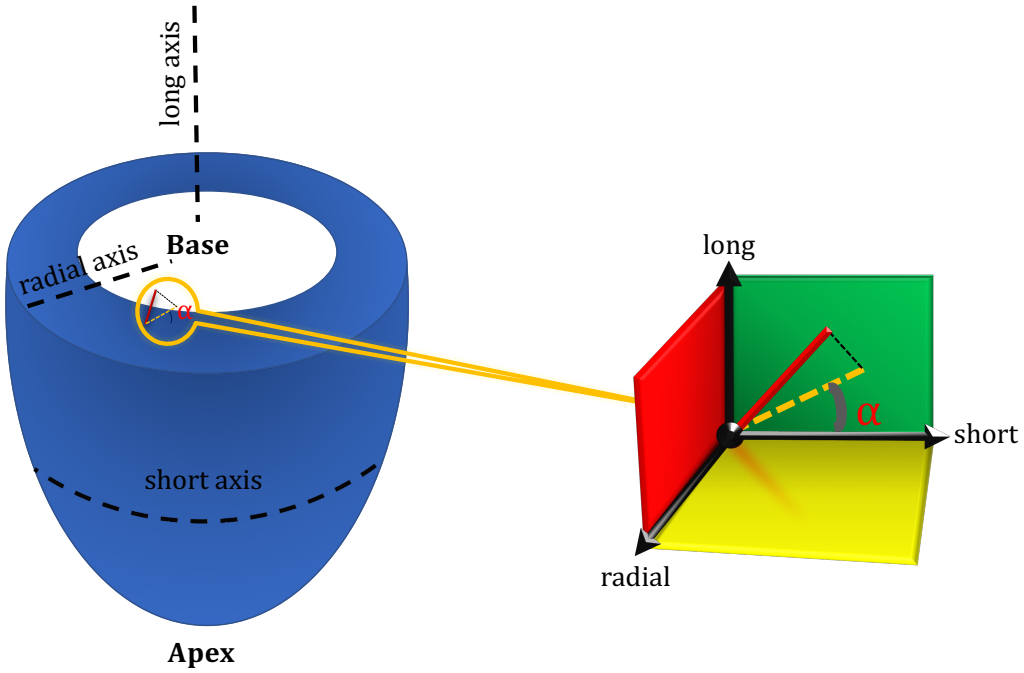

Figure 3.3: Modeling the left ventricle using two ellipsoids. The short and the long axes of the larger ellipsoid are shown with dashed lines. The transverse or circumferential plane is shown in **yellow**, the tangential plane in **green** and the axial or transmural plane in **red**. The fiber or helix angle α is illustrated as the angle between the projection of the fiber onto the tangential plane (dashed yellow line) and the circumferential plane [27, 67].

The question then is how can a 6% thickness change in each myocyte result in a 36% thickness change in the heart wall [82]? This is only possible if the myofibers change in angle moving from the epicardium to the endocardium. Thus, the notion of the helix angle (see Figure 3.3), which is also referred to in the literature as the fiber angle, is of significance.

Definition 6 *The helix angle α is the angle between the transverse plane and the projection of the direction of a myofiber onto the tangential plane.*

Achieving the desired wall thickening given the aforementioned criteria requires a change in the helix angle when moving in from epicardium to endocardium. This property has been verified by both histology [48] and MRI on ex vivo mammalian hearts [6, 34].

3.2 Early models of the geometry of myofibers

While the two ellipsoid model provides a description of the global geometry of the heart and permits mathematical analysis, it is at best a coarse approximation to reality. Early work in the modeling of ventricular macro structures, based on histology, attempted to introduce geometry-based modeling via intuitive interpretations. In 1953, Rushmer et al. [68] distinguished a 3 layer pattern for the macro organization of myocytes, namely, the superficial, middle and deep layers in the short-axis direction of the heart. As illustrated in Figure 3.4(A), this artificial division is sought to justify the rotation of regimes of myofibers moving from epicardium to endocardium. In 1979, Geiger [26] hypothesized an LV structure as a series of nested doughnut shaped geodesics. This model assumes that myocytes follow a helical pattern throughout the left ventricle. Later, Jouk et al. [41] extended this to the pretzel (nested doughnut) model, which combines two separate sets of geodesics for the right and the left ventricle (Figure 3.4 (B,C)). A rather controversial proposal by Torrent-Guasp et al. [89] assumes a single continuous band of muscle for the entire heart wall, which twists into two helices that are looped through the right and left ventricular volumes. This model of a helical ventricular muscle band (HVMB) is motivated by a particular manner of slicing the ventricles, which is guided by natural ventricular cleavage planes. Although at first glance this model roughly follows the principal

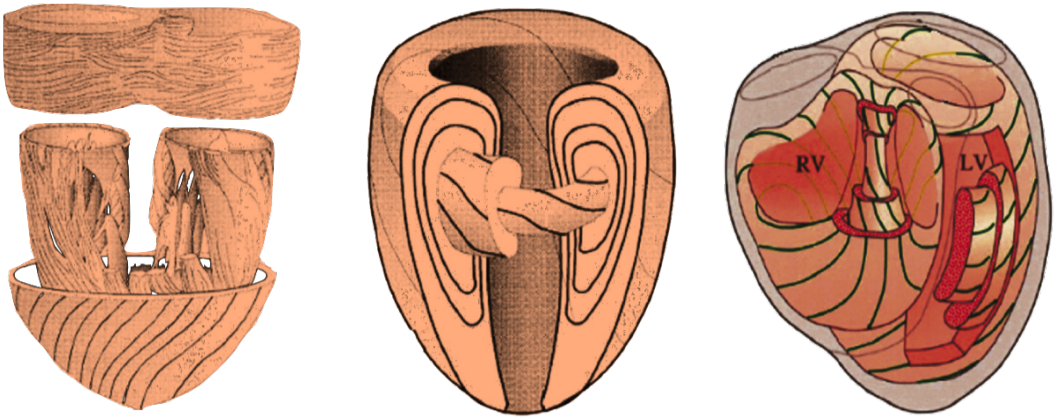

A B C

Figure 3.4: Early models of the heart wall. **A** A three layered model, **B** A simple dougnhnut model, and **C** A pretzel model (adapted from Gilbert et al. [27]).

direction of fibers everywhere, according a critical study by Gilbert et al. [27], it is not fully compatible with many other known features of myocardial structures.

3.2.1 Laminar structures and sheets in the heart wall

LeGrice et al.'s pioneering work[45] is among the first accounts of a laminar organization of ventricular myocytes in mammalian hearts. Prior to this work, the geometry of fiber paths was assumed to be helical from the apex of the heart to its base [53]. In addition, earlier studies of these structures were mostly limited to qualitative 3D descriptions based on 2D histology. Appreciating the significance of the 3D organization of myocytes in determining electrical and mechanical properties of the heart, the authors sought to find a more accurate justification of these characteristics from the geometrical perspective of myofibers. Moreover, they carried out a thorough analysis of the cellular architecture of ventricular tissues, regionally and globally, in both a quantitative and qualitative manner.

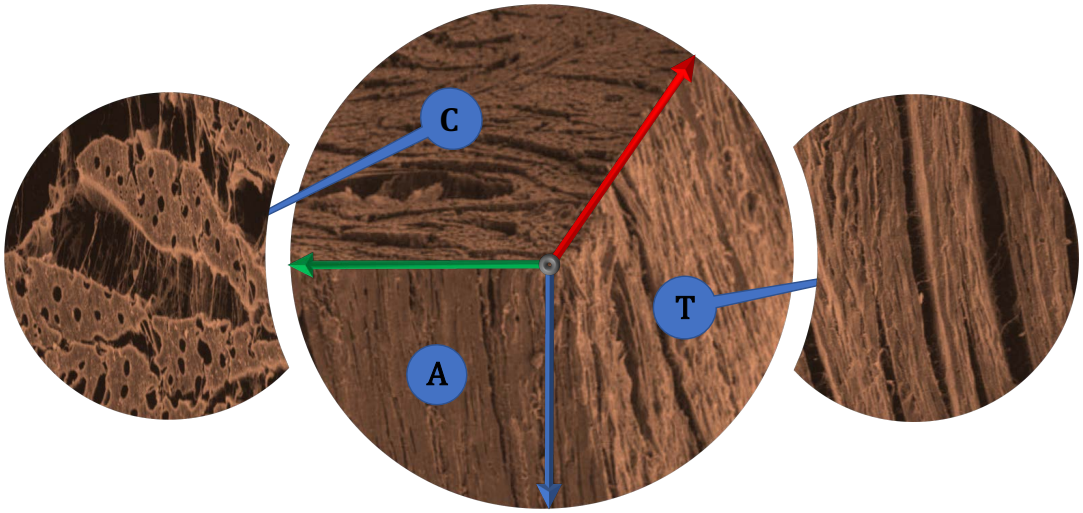

Figure 3.5: Visualization of the laminar structure of an ex vixo canine left ventricle. **Middle:** 3 orthogonal surfaces of LV: **C** Circumferential, **T** Tangential, **A** Axial. Red, green and blue arrows respectively represent short, radial and long axes (adapted from LeGrice et al. [45]).

To achieve this goal, four dogs were anesthetized and a series of sections from each heart were selected to be further studied using electron microscopy. The slicing of the ventricular muscles was carried out in accordance with the direction of fibers, with the short axis parallel to the mean fiber direction, which forms three orthogonal surfaces, as illustrated in Figure 3.5: circumferential, tangential, and axial. Several parameters were utilized in this study to quantify these scans, including, the number of myocyte branchings per unit, the relative path length of neighboring myocytes, the volume fraction occupied by myocytes, and the number of muscle cells in each layer.

As illustrated in Figure 3.5, muscle layers consist of a connected stack of myocytes that are separated via cleavage planes, while branching between the adjacent layers is relatively rare. LeGrice et al. [45] report a relative linear transmural increase in the volume of

myocytes and branches per unit and a decrease in the calculated length of connected fibers while moving from the inner wall to the outer wall. An abstract and simplified schematic is then represented to mimic the organization of muscle fibers, with a transmural segment of the cardiac wall containing layers of tightly linked myocytes running in the radial direction, with scattered circumferential and tangential branching visible between layers. The transmural organization of laminar sheets separated by cleavage planes is relatively well accepted in further studies in the cardiac imaging community [67, 34], which helps explaining the static structure of ventricular muscle tissues.

3.3 Emergence of cardiac DTI

By progress in Nuclear Magnetic Resonance (NMR) imaging, particularly the introduction of Diffusion Nuclear Magnetic Resonance Imaging (dMRI), a new window has been opened to the medical imaging community. Primarily, dMRI was developed for static tissues, such as the human brain, for mapping connectivity [4]. Then, it was further applied to assess the geometry of myofibers for ex vivo hearts [7, 34, 27]. DT-MRI or in short, DTI is an MRI based 3D imaging modality which models the axes of diffusion of water molecules by symmetric 3 by 3 tensor matrices. The three orthogonal eigenvectors of this matrix are then decomposed and sorted according to the magnitude of their eigenvalues. If there is no physical structure in the corresponding tissue, due to the isotropy of diffusion, water molecules should be able to move freely in any direction, and thus the 3 eigenvectors should have relatively close eigenvalues [27, 82]. In contrast, when the motion is restricted in certain directions, i.e., across fibers, as opposed to along them, a

diffusion tensor fit will exhibit the property that its direction of elongation serves as a proxy for the direction of highest diffusion (and hence fiber direction) [4]. We refer to the 3 ranked eigenvectors by the corresponding magnitudes of the eigenvalues as the primary, secondary and tertiary eigenvectors.

In the heart, wherein most regions the assumption of a single direction of dominant orientation holds, DTI is an accepted method and is favored in most studies [82, 27, 34]. There are, however, more advanced methods such as high angular resolution diffusion imaging (HARDI) [92, 2], that allow for more complex intra-voxel geometries to be modeled, such as branching or crossing fibers.

3.3.1 Cardiac DTI-based local coordinate system

In the case of ventricular muscle tissues, if we accept the geometry explained by LeGrice et al. [45], we should expect that the water molecules existing in cardiac myocytes should have the largest range of motion in the direction of myofibers, the second-largest degree of motion in the direction within laminar sheets and the least in the direction locally perpendicular to the sheet plane. There are several studies that validate this hypothesis by comparing DTI with histology [14, 34, 35, 91].

In several studies of myofiber geometry using DTI [27, 49, 67], the eigenvector directions are used to define a local coordinate system. Here the principal direction is taken to be that of the fibers, the second eigenvector is taken to span a sheet with the first, and the third eigenvector defines the direction of a sheet normal.

3.3.2 Sheet angle

The notion of a sheet angle varies in different papers [25, 45]. For instance, it could depend on the definition of a local and global coordinate system or on the scaling of this angle (either between 0 to 180 or -90 to +90 degrees). In attempt to have a unified definition, as illustrated in Figure 3.6, Gilbert et al. [27], defined the sheet angle β' as the angle between the circumferential (transverse) plane and the projection of the second eigenvector of a DTI reconstruction onto the radial plane spanned in the range of $[-90, +90]$ degrees. Then, based on this definition, the authors measured the β' sheet angle across different samples of DTI scans of 12 canine hearts. This work reported the amount of change in the sheet angle in different parts of the heart within a specimen and across different species. These observations led to the introduction of a notion of sheet stacks as a set of stacked laminar structures, which are separated by hypothetical boundaries. Each stack consists of a regime of circumferential myofibers. The sheet angle across these boundaries changes rapidly yet continuously when moving from epicardium to endocardium.

3.3.3 Reconstruction of cardiac myofibers and sheets using DTI

Another study by Rohmer et al. [67] of ex vivo DTI of a human heart also quantitatively verifies the earlier findings of the literature, regarding the geometry of cardiac myofiber geometry. Similar to [27], this paper assumes that cleavage planes are a barrier to the diffusion of water molecules and thus the smallest eigenvector of the diffusion tensor corresponds to the direction normal to these planes. More importantly, the authors introduce a novel model of cardiac myofibers and sheetlets from the eigenvectors decomposed from

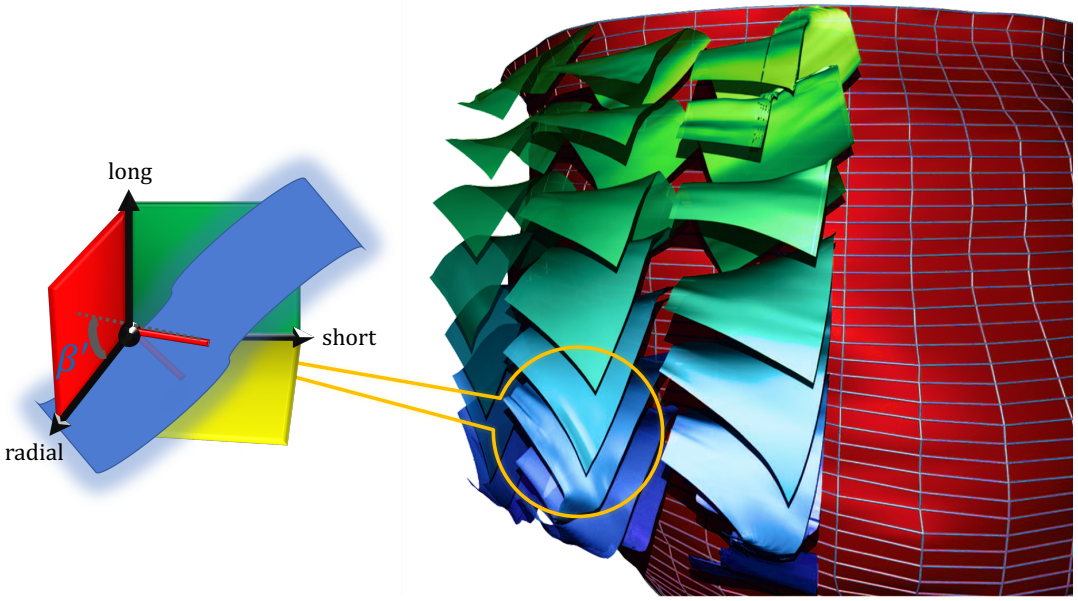

Figure 3.6: Visualization of the sheet angle (adapted from Rohmer et al. [67]). See text for a discussion.

the diffusion tensors of human cardiac data. To model the cardiac myofiber as a continuous streamline, the authors use a fiber tracking algorithm based on the direction of the principal eigenvector of the tensor matrices. From the computed fiber tracking system together with the second and third-ranked eigenvectors of the diffusion tensor, the authors construct a sheet tracking pipeline assuming that cardiac sheetlets should be oriented radially (in the direction of the second eigenvector). Then, based on these constructions, Rohmer et al. [67] calculate the sheet angle and the helix angle. Their findings confirm the earlier hypothesis based on histology [45], that the fiber angle changes gradually in the mid-wall section, but the amount of change closer to the epicardial and endocardial surfaces is more pronounced.

3.3.4 Cardiac DTI limitations

While DTI facilitates the study of cardiac macro structures in intact tissue, it suffers from certain limitations. The first has to do with the low resolution of MR based techniques. Even with the latest technology, the spatial resolution of DTI is too low to reflect the cellular arrangement of the myocardial structure. For instance, each voxel of an MR-based volume corresponds to 6 to 20 sheets [27] and around 4600 myocytes for the case of ex vivo human DTI [67].

A second challenge is that current acquisition techniques require that the scanned area should remain stable. In vivo diffusion imaging of the heart is an area of current research, and present in vivo imaging technology allows only for low resolution reconstructions [24, 23, 22, 57]. Having different time samples of in vivo data is particularly important when studying the mechanics of the heart, and the motion of the heart through the cardiac cycle. Furthermore, after the data is gathered, it usually has a low signal to noise ratio. Therefore, different smoothing and averaging techniques [46, 3, 70] are often used for post processing. On their own, these techniques could be a source of bias leading to misinterpretations of the original data.

As mentioned in Section 3.3, most of the work of the literature is based on the hypothesis that water molecules can move more freely in the direction of myocytes than in other directions within the sheet plane and have the least freedom in the orientation normal to the sheet. While this assumption makes intuitive sense, in practice it may not always be true for several reasons. For example, unlike in the brain, where tract systems are com-

prised of bundles of axons, the notion of myofibers in cardiac tissue is abstract [45, 82]. While the difference between the first eigenvalue of the diffusion tensor and the other two is significant, the second and third eigenvalues sometimes have similar values [49]. This can lead to local perturbation in the ranking result [67, 27], and thus affect the definition of an eigenvector based sheet plane. This assumption doesn't account for the motion of water molecules in other cardiac tissues that exist in the proximity of myocytes, including blood vessels, fat, and collagen.

3.4 Generalized helicoid model

Early studies in the literature show that the geometry of each fiber of the left ventricle of a heart is very close to a 3D helical curve [37]. Savadjiev et al. [75] describe one of the first attempts to model a volumetric bundle of cardiac myofibers together, using a Generalized Helicoid Model (GHM), as opposed to a single myofiber. Intuitively, this paper models the geometry of cardiac fibers as a texture flow in 3D space. First, the flows are parameterized using 3D geometrical coordinates. Thus, the frame field consists of three orthogonal bases, $\mathbf{E_T}, \mathbf{E_N}, \mathbf{E_B}$ where $\mathbf{T}, \mathbf{N}, \mathbf{B}$ are the tangent, normal and binormal vectors to an arbitrary point $q \in \mathbb{R}^3$ of a 3D texture flow. Using the same logic discussed in Section 2.3, this requires the parameterization of a surface $s(x, y, z) = (x, y, z, \theta(x, y, z))$ in $XYZ\theta$, where θ is the orientation function in the neighborhood of the point q. In 3D space, this has been modeled using a generalized helicoid:

$$\theta(x, y, z) = \tan^{-1}\left(\frac{\mathbf{K_T}x + \mathbf{K_N}y}{1 + \mathbf{K_N}x - \mathbf{K_T}y}\right) + \mathbf{K_B}z. \tag{3.1}$$

As can be seen, this is basically Equation (2.9), plus a linear term modeling rotation in the direction of the z coordinate. The authors make the assumption that, in the left ventricle of the heart, myofibers follow the geometry of a GHM texture flow. Based on this assumption, a brute-force search algorithm is run to fit the ground truth input acquired via diffusion MRI on a GHM. In other words, given that the GHM is a model that describes myocardial fiber geometry, Savadjiev et al. [75] try to find values of $\mathbf{K_T}, \mathbf{K_N}, \mathbf{K_B}$ which minimize the difference in orientation between the one predicted via a GHM fit and the one acquired via diffusion MRI, which are shown to provide accurate representations at the millimeter and sub-millimeter scales across mammalian species. They also show that an interesting feature of GHMs is that they are minimal surfaces, i.e., the mean curvature of the GHM is zero everywhere, which could be of significance in the context of mechanics of cardiac contraction.

3.5 Cartan connection model

We now follow up on the material in Section 2.2 by reviewing the mathematics of Cartan connection forms [16, 60] for the case of an orthonormal unit frame field $F = [\mathbf{f}_1, \mathbf{f}_2, \mathbf{f}_3]^T$ defined in $\mathbb{R}^3$, which is the construction used in [65] to describe the geometry of myofibers in a static heart wall. A covariant derivative of this frame field with respect to a vector $\mathbf{v}$ at point p is given by

$$\begin{aligned}
\nabla_{\mathbf{v}}\mathbf{f}_1 &= \omega_{11}(\mathbf{v})\mathbf{f}_1(p) + \omega_{12}(\mathbf{v})\mathbf{f}_2(p) + \omega_{13}(\mathbf{v})\mathbf{f}_3(p) \\
\nabla_{\mathbf{v}}\mathbf{f}_2 &= \omega_{21}(\mathbf{v})\mathbf{f}_1(p) + \omega_{22}(\mathbf{v})\mathbf{f}_2(p) + \omega_{23}(\mathbf{v})\mathbf{f}_3(p) \\
\nabla_{\mathbf{v}}\mathbf{f}_3 &= \omega_{31}(\mathbf{v})\mathbf{f}_1(p) + \omega_{32}(\mathbf{v})\mathbf{f}_2(p) + \omega_{33}(\mathbf{v})\mathbf{f}_3(p)
\end{aligned} \tag{3.2}$$

where $i \in \{1, 2, 3\}$, and $\omega_{ij}(\mathbf{v}) = \nabla_{\mathbf{v}}\mathbf{f}_i \cdot \mathbf{f}_j$. O'Neill [60] shows that these ω_{ij}s satisfy the definition of 1-forms in $\mathbb{R}^3$. For any vector field $\mathbf{v}$ in $\mathbb{R}^3$

$$\nabla_{\mathbf{v}}\mathbf{f}_i = \sum_j \omega_{ij}(\mathbf{v})\mathbf{f}_j. \tag{3.3}$$

Using the alternating property of 1-forms, $\omega_{11} = \omega_{22} = \omega_{33} = 0$ and $\omega_{21} = -\omega_{12}, \omega_{31} = -\omega_{13}, \omega_{32} = -\omega_{23}$. Let us assume that the frame field F has the following parametrization in the universal Cartesian coordinate system $E = [\mathbf{e}_1, \mathbf{e}_2, \mathbf{e}_3]^T$:

$$\begin{aligned} \mathbf{f}_1 &= \alpha_{11}\mathbf{e}_1 + \alpha_{12}\mathbf{e}_2 + \alpha_{13}\mathbf{e}_3, \\ \mathbf{f}_2 &= \alpha_{21}\mathbf{e}_1 + \alpha_{22}\mathbf{e}_2 + \alpha_{23}\mathbf{e}_3 \\ \mathbf{f}_3 &= \alpha_{31}\mathbf{e}_1 + \alpha_{32}\mathbf{e}_2 + \alpha_{33}\mathbf{e}_3 \end{aligned} \tag{3.4}$$

where each $\alpha_{ij} = \mathbf{f}_i \cdot \mathbf{e}_j$ is a real valued function. The matrix $A = [\alpha_{ij}]$ is called the attitude matrix, and $dA = [d\alpha_{ij}]$ is a matrix whose elements are 1-forms. With $\omega = [\omega_{ij}]$ it can be shown that $\omega_{ij} = \sum_k (d\alpha_{ik})\alpha_{kj}$ [60], so

$$\omega = dAA^T. \tag{3.5}$$

Connection forms describe the rate of change of a frame field $[\mathbf{f}_1, \mathbf{f}_2, \mathbf{f}_3]^T$ in the direction of an arbitrary vector $\mathbf{v}$. The dual 1-form of the frame field $[\mathbf{f}_1, \mathbf{f}_2, \mathbf{f}_3]^T$ is obtained when it is itself parametrized via 1-forms, i.e., for each vector $\mathbf{v}$ at p, $\psi_i(\mathbf{v}) = v \cdot \mathbf{f}_i(p)$. For the sake of simplicity we will use the same notation for the frame and its dual representation,

i.e.,

$$\mathbf{f}_i(\mathbf{v}) = \psi_i(\mathbf{v}) = v \cdot \mathbf{f}_i(p). \tag{3.6}$$

From the definition of the 1-form,

$$dx_i(\mathbf{v}) = \sum_j \mathbf{v}_j \frac{\partial x_i}{\partial x_j}(p) = \mathbf{v}_i. \tag{3.7}$$

Combining Equations (3.6) and (3.7) results in

$$\mathbf{f}_i(\mathbf{e}_j) = \mathbf{f}_i \cdot \mathbf{e}_j = (\sum_k \alpha_{ik}\mathbf{e}_k)\mathbf{e}_j = \alpha_{ij}. \tag{3.8}$$

From Equations (3.7) and (3.8) we have $\mathbf{f}_i = \sum_j \alpha_{ij} dx_j$ which, with $F = [\mathbf{f}_i]^T$, can be written in the dual 1-form representation as $F = A[dx_1 \quad dx_2 \quad dx_3]^T$. The Cartan structural equation is then given by O'Neill [60]:

$$\begin{aligned} d\mathbf{f}_i &= \textstyle\sum_j \omega_{ij} \wedge \mathbf{f}_j, \text{ i.e., } dF = \omega F, \\ d\omega_{ij} &= \textstyle\sum_k \omega_{ik} \wedge \omega_{kj}, \text{i.e., } d\omega = \omega\omega. \end{aligned} \tag{3.9}$$

Since there are three unique connection forms $\omega_{12}(\mathbf{v}), \omega_{13}(\mathbf{v}), \omega_{23}(\mathbf{v})$, feeding the frame field's unit vectors to them produces nine different connection parameters $c_{ijk} = \omega_{ij}(\mathbf{f}_k)$. Here, for the vector $\mathbf{v}$ at a point p, $\omega_{ij}(\mathbf{v})$ represents the amount of $\mathbf{f}_i(p)$'s turn toward $\mathbf{f}_j(p)$ when p moves in the direction of $\mathbf{v}$. The estimation of these connection parameters for frame fields attached to diffusion MRI data of ex vivo hearts was the strategy proposed in [65] to parametrize the static geometry of heart wall myofibers.

These nine different coefficients are used to estimate the motion of the frame field using first order approximation of the Taylor expansion of the frame field F in the direction of the vector $\mathbf{v}$ at a point p

$$\mathbf{f}_i(\mathbf{v}) \simeq \mathbf{f}_i(p) + d\mathbf{f}_i(\mathbf{v}). \tag{3.10}$$

Applying the Cartan structural Equation (3.9) on the Equation (3.10), where $\mathbf{v} = \sum_k \mathbf{v}_k \mathbf{f}_k$, results in:

$$\mathbf{f}_i(\mathbf{v}) \simeq \mathbf{f}_i(p) + \sum_j (\sum_k \mathbf{v}_k c_{ijk}) \mathbf{f}_j(p). \tag{3.11}$$

This idea is then used to calculate the local rotation of a frame field using connection forms. Piuze et al. [65] address different approaches to estimate each c_{ijk} for an arbitrary smooth frame field. In several related papers based on this idea [66, 80, 81, 65] apply algorithms for fitting connection forms to frame fields attached to diffusion MR data of ex vivo mammalian hearts.

3.6 Sheets in the mammalian brain

The white matter of the mammalian brain consists of bundles of elongated nerve fibers, called axons [54]. Unlike cardiac ventricle myofibers, which are abstract representations of interconnected myocytes, brain axons are organized in actual fiber bundles that literally connect different regions of brains to communicate electric signals between them. These bundles themselves then form groups which are referred to as white matter fiber tracts [40]. Knowing the geometry of these fiber bundles or streamlines is particularly important in neuroscience, e.g., to help neurosurgeons in planning surgeries with minimal possibility

of damage to important tract systems in order to preserve the functionality of the brain.

Similar to the case of cardiac dMRI, water molecules are assumed to have more freedom in their motion in the direction of axons. However, as discussed in Section 3.3.4, the resolution of MR-based techniques for mapping fiber tract systems in the brain is far behind the resolution of physical structures in question. In fact, according to [39], a single voxel acquired via dMRI can contain hundreds of thousands of axons and other neighboring biological tissues. Furthermore, for the case of neurological dMRI, fiber crossings due to intersections of axon bundles, make the characterization of their geometry even more complex than that of cardiac DTI.

While DTI can only provide information regarding a single direction for tracts per voxel, more advanced dMRI based modalities, such as high angular resolution diffusion imaging (HARDI) [92, 2], account for potential crossing of fibers within a voxel. Therefore, fiber tracking or the development of tractography algorithms for application to neuro-dMRI is a complex topic of research that is beyond the scope of this dissertation [39]. These algorithms can be used to provide navigation maps of cerebral fiber paths of white matter connections, namely connectomes. In 2009, Van Essen et al. [93], commenced a neuro-imaging project in which they gathered comprehensive MR scans of a population of 1200 healthy adults, making them available to the research community for further analysis. Their results have been used in the research that followed since then, including in the Human Connectome Project (HCP) [52]. These results are used in Part II for proof of concept validation of the sheet finding algorithm we propose.

The notion of sheets in human connectomes has been around in the literature implic-

3.6 Sheets in the mammalian brain

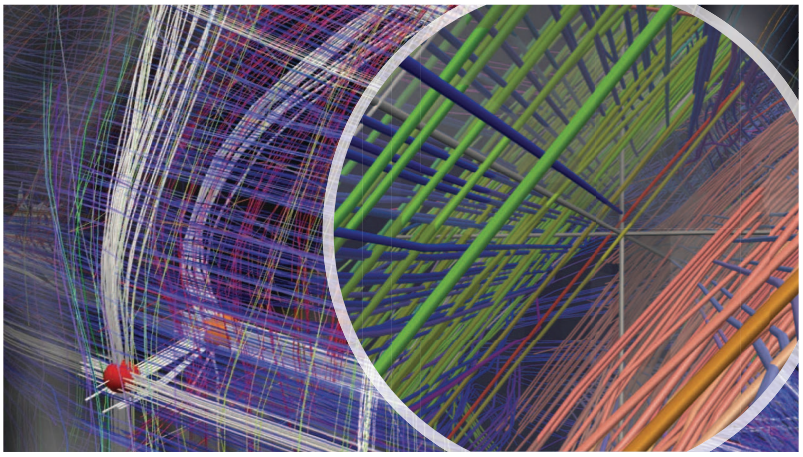

Figure 3.7: Visualizing sheets as gridlike structures in the crossing of fiber pathways in the brain (adapted from Wedeen et al. [99]).

itly for some time [94, 43, 104]. In 2012, Wedeen et al. [99], in a rather controversial article, reported that fiber pathway crossings have a gridlike pattern in certain areas of the brain. As illustrated in Figure 3.7, different fiber tracts, which can be visualized as 3D streamlines, appear to form regular grids that cross each other almost orthogonally, throughout the brain. The authors argue that this is statistically impossible unless there exists an underlying structure to these areas of interest. They report qualitative results both on distinct brain regions and on different mammalian species. Catani et al. [12] in a critical review question the existence of these perpendicular crossings. They argue that this phenomenon could be the result of the limitation of the tractography algorithm used in [99] and the image acquisition and reconstruction process itself.

While this research has spawned much discussion [98], the construction of principled methods for finding sheet-like structures and quantifying them has largely remained an open question. From another perspective, in a series of publications, Tax et al. [86, 87]

introduced the notion of a “Sheet Probability Index (SPI)” to quantify the likeliness that a sheet passes through a query voxel of white matter in a diffusion tensor reconstruction. This measure is not a probability, strictly speaking. They show that certain regions of the brain are more likely to have sheet-like structures since the normal component of the Lie bracket of the 2 principal vector fields of their corresponding voxels has relatively higher values. They also demonstrate robustness and consistency in their findings over different specimens, scanners, and imaging techniques.

Part II

Part II: Finding Sheets in Biological Tissues

4

Introduction

The contents of this part are largely based on the articles: “Estimating Sheets in the Heart Wall”[85], and “Minimizing Non-holonomicity: Finding Sheets in Fibrous Structures”[71] which are the result of collaborative work with colleagues in the Shape Analysis Group at McGill University. This work focuses on finding sheet-like structures in biological tissues.

Fibrous biological tissues are reported to be organized in sheet-like geometries in certain regimes. Examples include laminar sheets and cleavage planes in the heart wall [34, 45], and sheets on which fiber tract systems in the mammalian brain are posited to lie [99]. Quantitative geometric characterizations of sheets in biological tissue are often based on orientation measurements from in-vivo or ex-vivo specimens, using diffusion imaging. Heart wall myofibers are thought to lie within laminar sheets, an organization

which exerts an important influence on the heart's mechanical and electrophysiological properties [55, 20]. In work based on thick tissue sections from excised canine hearts using scanning electron microscopy, as well as studies based on contrast-enhanced MRI, it has been shown that these laminar sheets are geometrically prominent, and can be associated with large cleavage planes which fall between them [45, 28]. When working with intact excised hearts, sheet orientation is typically estimated using the three eigenvectors of a diffusion tensor reconstruction. In the majority of such approaches, the principal eigenvector is assumed to coincide with myofiber orientation and is taken together with the second eigenvector to span the local sheet. The third eigenvector thus gives the normal to the sheet, with qualitative justification such as that given in [34]. A typical example is the tracking and reconstruction algorithm developed by Rohmer et al. for the visualization of laminar sheets in a cadaver human heart in [67], as reviewed in Chapter 3, Section 3.3.3.

Once estimated, sheet structure can be the basis for the assessment of normal heart function. For example, Dou et al. investigate the hypothesis that ventricular thickening in humans occurs via laminar sheet shear and sheet extension, using diffusion and strain MRI [18]. In the context of electrophysiology, Young and Panfilov put forth the hypothesis that an assumption of differing conduction speeds along fibers (v_f), across them but in laminar sheets (v_s), and between the laminar sheets (v_n), can reliably predict the time of arrival of the conduction wave, at any particular location in the heart [101]. This conduction wave triggers the contraction of myocytes, which in turn determines the timing and dynamic shape of the heart beat.

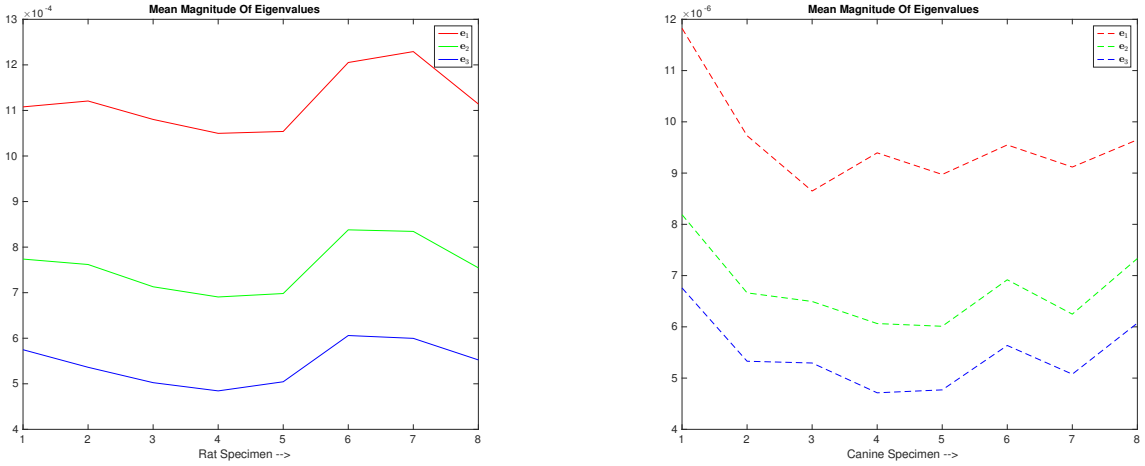

Figure 4.1: The mean eigenvalues of the three eigenvectors of the diffusion tensor for 8 different rat (**left**) and canine (**right**) specimens. The data is from the open access repository in [76].

Whereas the idea that the principal eigenvector gives a faithful estimate of local myofiber orientation has widespread support, the second and third eigenvectors are associated with eigenvalues that are sometimes very close to one other. When this happens, these directions are locally ambiguous. Examples of plots of mean eigenvalues are shown for 8 rat and 8 canine heart datasets in Figure 4.1. In one of the first reported studies of similar canine DTI datasets by Peyrat et al. [62], a statistical analysis framework for atlas construction was proposed. The results showed consistency in fiber orientations associated with the principal eigenvector, but greater variability in sheet structure derived from the remaining two. Similar trends in terms of the relative magnitudes of the mean of the three eigenvalues were observed by Lombaert et al. [49], where an atlas of 10 ex vivo human hearts were constructed, and detailed tensor statistics were reported. Here the second and third eigenvalues were found to have greater standard deviations as well as overlap in their distributions. Thus, in such situations, the directions of the second and third eigenvectors

can be ambiguous and reliance on them for sheet estimation could be problematic.

The same is true of the mammalian brain; in regions where multiple tract systems co-exist and cross one another, fiber geometry is not well characterized by a single diffusion tensor. In the human brain, the hypothesis that distinct tract systems lie on 2D sheets which intersect one another at approximately 90 degree angles to generate a local grid-like pattern, has been supported by qualitative considerations and visualization in [99]. Others have pointed out that distinct tract systems might span a sheet without being locally orthogonal to one another [12] and that quantitative measures of sheet geometries derived from diffusion data are desirable [86, 87, 1]. Yushkevich et al. [103] have fit deformable medial models to segmented tract systems to obtain sheet-like representations of fasciculi where appropriate [104]. Motivated by the property that two vector fields span an integrable surface when the normal component of the associated Lie bracket goes to zero, Tax et al. have used this quantity to define a local sheet probability index along with robust algorithms to estimate it [86, 87]. In their work, the local vector field directions are chosen from the peaks of a fiber orientation distribution function. The normal component of the Lie bracket has also been shown to be effective for sheet structure visualization, via the construction of a sheet tensor in [33], while Ankele and Shultz have applied this measure directly to diffusion tensor data in [1]. Motivated by these formal approaches to sheet structure estimation based on the integrability of vector fields, in this part of the thesis, we study a more general problem, which is the reconstruction of local sheets from a *single* direction field. Such a field might arise from the principal eigenvector direction of a diffusion tensor (e.g. as in the case of the heart wall), or from the tangent vectors to precomputed streamlines, as in the case of labeled tract systems in the mammalian brain.

Introduction

We depart from past approaches by treating sheet structure estimation as an energy minimization problem, where, given the single direction field as input, we find a second vector field that is optimal with respect to spanning a local sheet with it. The main idea here is to find the best local vector field orthogonal to the principal eigenvector in the sense of spanning a sheet. To accomplish this goal, we first use the Lie bracket along with a suitable energy function to estimate this vector field via energy minimization. This construction is reported in Section 5.1. Then, in Section 5.2, we extend this minimization by using a formal notion of holonomicity. Holonomic vector fields can be shown to be normal to a family of smooth surfaces. As it turns out, this is equivalent to finding the second field as a local minimizer of the normal component of a Lie bracket. Based on these ideas, we present a gradient descent based algorithm to recover sheets, along with a proof of convergence. We also report a very efficient implementation of the algorithm using GPUs. Our application of this algorithm to mammalian heart wall orientation data from two species, rat and canine, reveals sheet geometries consistent with what has been reported only in qualitative descriptions thus far from DTI, or in observations from histological slices of heart wall tissue. Of more significance are our results on labeled tract systems from the Human Connectome Project, where we test the sheet hypothesis in a formal way. Given a tract system described as a collection of streamlines in 3D as input, we recover sheet geometries where there is support for them. As a by-product of our approach, we provide high quality visualizations of the sheets in biological structures using the software we have written. We anticipate that such visualizations will be useful to anatomists when examining fibrous structures in the context of their local surroundings.

5

Methods

First, in Section 5.1, we consider the Lie bracket and develop a heuristic method to minimize it in order to find sheet-like structures. This first construction, although effective in practice, does not provide theoretical convergence guarantees, and the implementation is computationally expensive. Motivated by these considerations, in Section 5.2 we consider the formal notion of holonmicity and try to find sheets that directly minimize a non-holonomicity based energy. We show that our method converges under certain assumptions on the energy functional and we provide an efficient and GPU-based implementation of it.

5.1 Sheet estimation by Lie bracket energy minimization

As discussed in Chapter 4, laminar sheets, and cleavage planes have been posited to exist but evidence of them are via 2D histology. The problem of recovering sheet models di-

rectly from cardiac DTI is of interest since this allows for 3D full heart analysis. In this section, we design a pipeline that estimates sheets in the heart only from the principal eigenvector of DTI data. Let $\mathbf{u}$ be the unit norm vector field derived from the principal eigenvector of a cardiac DTI reconstruction aligned with the local direction of myofibers. This is a common assumption, used in the context of fiber orientation modeling from diffusion data in a variety of methods, as reviewed in [82]. The second and third eigenvectors can be associated with similar eigenvalues (see Figure 4.1) and thus may not be reliable for sheet estimation. We use the following alternate strategy to recover the sheet direction, $\mathbf{v}$, using only the principal eigenvector $\mathbf{u}$. Let $\mathbf{v}(\theta)$ be a vector field in the local plane perpendicular to the vector field $\mathbf{u}$. Our objective is to estimate the field $\hat{\mathbf{v}}(\theta)$, which together with $\mathbf{u}$ spans a local sheet, by minimizing a Lie bracket based energy $E_p(\theta)$ which at point p is defined as follows:

$$E_p(\theta) = \sum_{q \in N(p)} L_q(\theta)^T L_q(\theta). \tag{5.1}$$

Here $L_q(\theta) = J_{\mathbf{v}_q(\theta)}\mathbf{u} - J_{\mathbf{u}_q(\theta)}\mathbf{v}$ is the Lie bracket at the point q and $\mathbf{v}_q(\theta)$ and $\mathbf{u}_q$ are the values of vector fields $\mathbf{v}$ and $\mathbf{u}$ respectively at the point q. Note that $\mathbf{v}_p$ is a function of a single parameter θ - the orientation of the vector in the plane perpendicular to the fixed field $\mathbf{u}_q$. We shall not express $\mathbf{v}_p$ in terms of θ, since this parameter is not used explicitly in the algorithm reported in this section.

In order to minimize the energy $E(\theta)$, we use gradient descent with respect to θ pointwise. Rather than using θ explicitly we directly update the vector field $\mathbf{v}$ using the follow-

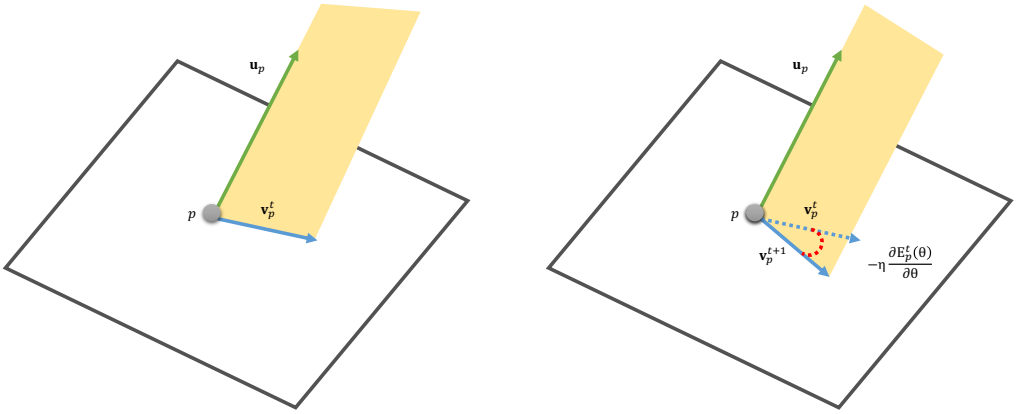

Figure 5.1: An illustration of a gradient decent step of the Lie bracket energy minimization algorithm. **A**: Illustration of two normal vectors u, v that estimate the sheet locally at point p. **B**: Visualization of the updated v after a step of gradient decent.

ing update equation:

$$\mathbf{v}_p^{t+1}(\theta) = \mathbf{v}_p^t(\theta - \eta \frac{\partial E(\theta)}{\partial \theta}).$$

The update is performed by rotating $\mathbf{v}_p$ about the axis $\mathbf{u}_p$ by an angle $\eta \frac{\partial E(\theta)}{\partial \theta}$. This method of update allows us to not have to write $\mathbf{v}$ explicitly in terms of θ and also ensures that the vector field $\mathbf{v}$ stays in the plane perpendicular to $\mathbf{u}$ after the update. This turns out to be more convenient than explicitly solving the problem for the Cartesian parameterization. Figure 5.1 provides a schematic illustration of a gradient decent step of our Lie bracket energy minimization algorithm.

5.2 Sheet estimation by non-holonomicity energy minimization

The notion of the Lie bracket has also been used in past approaches in computing sheet probability indices, such as in the work by Tax et al. [86]. As such, using it to devise an algorithm for sheet estimation by minimizing it was a reasonable start. However, there were certain limitations, the most serious of which is that there is a lack of theory to support the direct minimization. In this section, we, therefore, propose an improved method which is based on the notion of non-holonomicity. It has been shown by Yu [102], that for a pair of vector fields which span a surface, the non-holonomicity vanishes identically. Thus, one can directly minimize the non-holonomicity as an objective of the energy minimization. Similar to Section 5.1, let $\mathbf{u}$ be tangent to the direction of fibers and $\mathbf{v}$ be the current estimate of the vector field such that $\langle \mathbf{u}, \mathbf{v} \rangle = 0$. Further, let $\rho^{\mathbf{uv}}$ be the non-holonomicity function of $\mathbf{u}$ and $\mathbf{v}$. We propose a strategy which starts with a *single* input vector field $\mathbf{u}$, and estimates an orthonormal vector field $\mathbf{v}$ by iterative minimization of an appropriate energy function.

Consider the non-holonomicity $\rho(\theta)$ corresponding to a perturbed vector field $\hat{\mathbf{v}} = \mathbf{v}(\theta)$, where θ is a scalar function which parametrizes the field $\hat{\mathbf{v}}$ with respect to field $\mathbf{v}$ in the plane perpendicular to $\mathbf{u}$. Using the definition of non-holonomicity $\rho^{\mathbf{uv}}$ given in Chapter 2, Section 2.1, a straightforward computation shows that $\rho(\theta)$ is given by

$$\rho(\theta) = \rho^{\mathbf{uv}} \cos^2\theta + \rho^{\mathbf{un}} \sin^2\theta + \alpha^{\mathbf{uv}} \sin 2\theta + \nabla_{\mathbf{u}}\theta = \rho_s(\theta) + \nabla_{\mathbf{u}}\theta, \tag{5.2}$$

where, $\alpha^{\mathbf{uv}} = \frac{\langle \mathbf{n},[\mathbf{u},\mathbf{n}]\rangle - \langle \mathbf{v},[\mathbf{u},\mathbf{v}]\rangle}{2}$ and, $\rho^{\mathbf{uv}}$ and $\rho^{\mathbf{un}}$ are the non-holonomicity functions of the unperturbed fields $\mathbf{u}$ and $\mathbf{v}$, and $\mathbf{u}$ and $\mathbf{n}$.

Notice that for a constant perturbation function θ, $\nabla_{\mathbf{u}}\theta = 0$. Therefore $\rho(\theta) = \rho_s(\theta)$, the sinusoidal part of the $\rho(\theta)$ function which has a period of π. Further, a 180° turn of $\mathbf{v}$ leaves $\rho(\theta)$ unchanged. We know that for regions with sheet-like geometry, the spanning vector fields $\mathbf{u}$ and $\mathbf{v}$ are such that $\rho^{\mathbf{uv}} = 0$. We, therefore, define an energy function as follows:

$$E(\mathbf{u}, \mathbf{v}, \theta) = \rho^2(\theta). \tag{5.3}$$

This energy is zero in regions where $\mathbf{u}$ and $\mathbf{v}$ span a sheet, and high in regions which are less sheet-like. We can therefore pose the estimation of the vector field $\mathbf{v}$ as the following energy minimization problem:

$$\begin{aligned} \mathbf{v}^* &= \arg\min_{\mathbf{v}} E(\mathbf{u}, \mathbf{v}, \theta) \\ &\text{subject to } \langle \mathbf{u}, \mathbf{v} \rangle = 0. \end{aligned} \tag{5.4}$$

5.2.1 Minimization algorithm and analysis

We solve the minimization problem of Equation (5.4) using an iterative gradient descent approach. Figure 5.2 presents an overview of this approach. We initialize with a $\mathbf{v}$, such that the orthogonality constraint $\langle \mathbf{u}, \mathbf{v} \rangle$ is satisfied. We maintain this constraint in the subsequent iterations by forcing each update to lie in the plane orthonormal to $\mathbf{u}$. At each

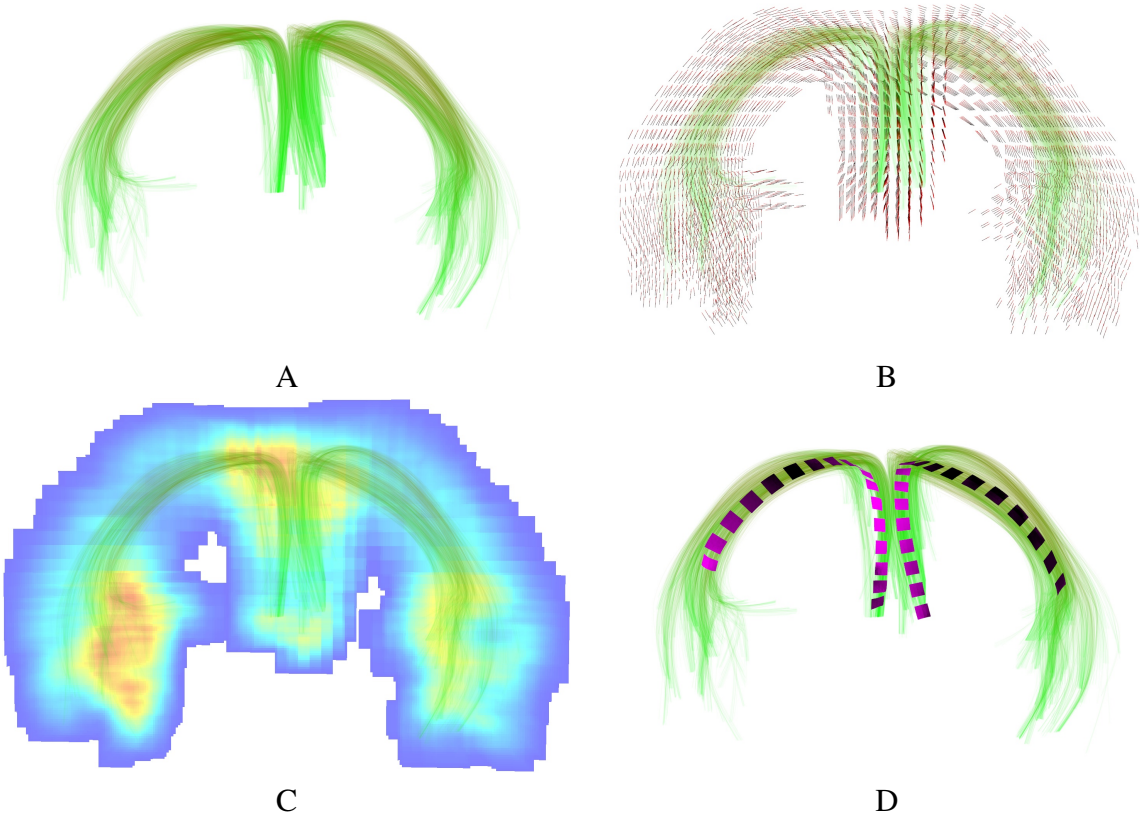

Figure 5.2: (Best viewed by zooming-in on the electronic version of this thesis) **A**: We assume as input a set of streamlines, in this example those corresponding to the left and right Fornix tracts from a Human Connectome Project (HCP) atlas. **B**: We then extract a local direction field on a discrete grid, using the tangents to the streamlines. **C**: The local non-holonomicity value, after convergence of our algorithm, gives a measure of how likely it is that the streamlines support a sheet-like organization locally. The non-holonomicity energy increases from light blue to red, using a jet colormap volumetric rendering. **D**: Our estimated sheets are overlaid on the streamlines as magenta surfaces, but only in regimes found to support sheet-like geometries.

step the varying vector field $\mathbf{v}(\theta)$ is updated using the gradient of the energy function

$E(\mathbf{u}, \mathbf{v}, \theta)$. We update θ using a general discrete gradient descent update as follows:

$$\frac{\theta^{t+1} - \theta^t}{\eta} = -\frac{\partial E(\theta)}{\partial \theta}$$
$$\implies \mathbf{v}^{t+1} = \mathbf{v}(\theta^{t+1}),$$

where η is the size of the time step. The update for $\mathbf{v}$ is carried out implicitly by rotating $\mathbf{v}$ about vector $\mathbf{u}$ without explicitly using θ^{t+1}. To rotate the vector $\mathbf{v}$ by an angle β we use the rotation matrix $\mathbf{R}^{\mathbf{u}}_{\beta} = \cos\beta\,\mathbf{I} + \sin\beta\,[\mathbf{u}]_\times + (1 - \cos\beta)(\mathbf{u}\mathbf{u}^T)$, where $[\mathbf{u}]_\times$ is the cross-product matrix corresponding to $\mathbf{u}$. This ensures that the orthonormality constraint is satisfied at every iteration, without having to explicitly express $\mathbf{v}$ as a function of θ in the local coordinates.

One can observe that the energy E is a function not only of the values of the vector fields $\mathbf{u}$ and $\mathbf{v}$ at a point but also of their derivatives. Therefore, the energy at a point depends on the value of the field at that point and its neighborhood. It is quite possible, therefore, that a local point wise gradient descent update at a point, as described above, may increase the energy in the neighbourhood. In fact, a key contribution of our method is that it converges due to the following property

Proposition 1 *For an incompressible smooth vector field* $\mathbf{u}$*, there exists a positive* η *such that a gradient descent update of* θ *reduces the energy everywhere.*

Proof 1 *(A more detailed proof is available in Appendix A.) Let* $\mathbf{u}$ *be the fixed input vector field and* $\mathbf{v}$ *be the current estimate of the second vector field. Consider the gradient of the*

energy function of Equation (5.3) *at time* t *given by*

$$\frac{\partial E(\theta)}{\partial \theta} = 2\Big(\rho_s(\theta) + \nabla_{\mathbf{u}}\theta\Big)\Big((\rho^{\mathbf{un}} - \rho^{\mathbf{uv}})\sin 2\theta + 2\alpha^{\mathbf{uv}}\ \cos 2\theta + \operatorname{div}\mathbf{u}\Big),$$

where θ *represents the perturbation with respect to the current* $\mathbf{u}$ *and* $\mathbf{v}$.

Before the update, $\theta \equiv 0$, *therefore we have*

$$\frac{\partial E(\theta)}{\partial \theta}\Big|_{\theta\equiv 0} = 2\rho^{\mathbf{uv}}(2\alpha^{\mathbf{uv}} + \operatorname{div}\mathbf{u}) = \mathcal{E}_0^{\rho}.$$

Then, θ^{t+1} *is given by*

$$\theta^{t+1} = -\eta\mathcal{E}_0^{\rho}.$$

To prove our claim, it is sufficient to show that this update reduces the energy, so that

$$E(0) > E(-\eta\mathcal{E}_0^{\rho}). \tag{5.5}$$

For small θ *we let* $\sin\theta \approx \theta$, $\cos\theta \approx 1$. *The condition for convergence in Equation* (5.5) *for small positive* η *then reduces to*

$$4\alpha^{\mathbf{uv}}(2\alpha^{\mathbf{uv}} + \operatorname{div}\mathbf{u}) + \nabla_{\mathbf{u}}\mathcal{E}_0^{\rho} > 0.$$

Since we have assumed that our initial fixed vector field $\mathbf{u}$ *represents smoothly varying local orientation in fibrous tissue, we can assume that* $\operatorname{div}\mathbf{u}$ *is small, and then the con-*

vergence condition reduces to $\nabla_{\mathbf{u}}\mathcal{E}_0^\rho \gtrapprox -8(\alpha^{\mathbf{uv}})^2$*. For a smooth enough vector field with small divergence, we can choose a positive time step* η *such that the energy is reduced.*

It is possible to consider a stronger smoothness condition: $|\nabla_{\mathbf{u}}\mathcal{E}_0^\rho| < 8(\alpha^{\mathbf{uv}})^2$*, which helps us improve our energy function and select the additional parameters, as discussed in the following section.*

6

Experiments and Discussion

In this chapter, in Section 6.1 we first show the findings of our first attempt to develop a sheet finding algorithm according to the method described in Section 5.1. This implementation shows the experimental promise of our method and illustrates proof of concept results. In future work, in Section 6.2, based on the algorithm described in Section 5.2, we demonstrate more comprehensive experimental results using a more efficient implementation that is fast and is supported by proof of convergence. While developing our algorithms,we tested different parts of our implementations using a controlled prototype for which we had a closed-form solution for our input. For instance, considering a circumferential vector field in a cylindrical volume, we were able to show that depending on our initialization, our estimated second vector field was either axial or radial.

6.1 Sheets estimated by Lie bracket energy minimization

We tested our Lie bracket energy minimization algorithm on ex vivo DTI data of 8 rat hearts and 8 canine hearts from the open access repository in [76], with an initial step size of $\eta = 0.2$ and an exponential decay with a decay rate of 0.9 and decay every 20 steps. Each rat heart dataset is $64 \times 64 \times 128$, with a voxel dimension of $0.25 \times 0.25 \times 0.25mm^3$. Each canine dataset is $300 \times 300 \times 333$, with a voxel dimension of $0.3125 \times 0.3125 \times 0.8mm^3$. The canine specimens are therefore 57 times larger than the rat specimens in terms of the number of voxels. In practice, our algorithm converges relatively fast, with the gradient descent loss plateauing after about 150 iterations. We ran each specimen, from both the rat and canine datasets, for 200 iterations. Our Matlab implementation, which has not been optimized, took about 50 minutes per rat heart and around a day for each canine heart on an Intel Core i9-7900x machine. We note that since our energy is local, it would be possible to get a significant boost in speed by implementing the algorithm on a GPU, thus making the approach quite practical.

Given the noisy nature of DTI data, in our implementation, we estimate the partial derivatives using the minimum of central, forward and backward finite differences, as a simple form of filtering. Using the minimum of these three finite differences helps smooth the derivatives while preserving local structure in the presence of noise. Further, we also correct for any random 180° flips present in the raw eigenvector directions due to the directionless nature of DTI tensor measurements.

Figure 6.1 compares our estimated sheet direction vector $\hat{\mathbf{v}}$ (red) with the commonly

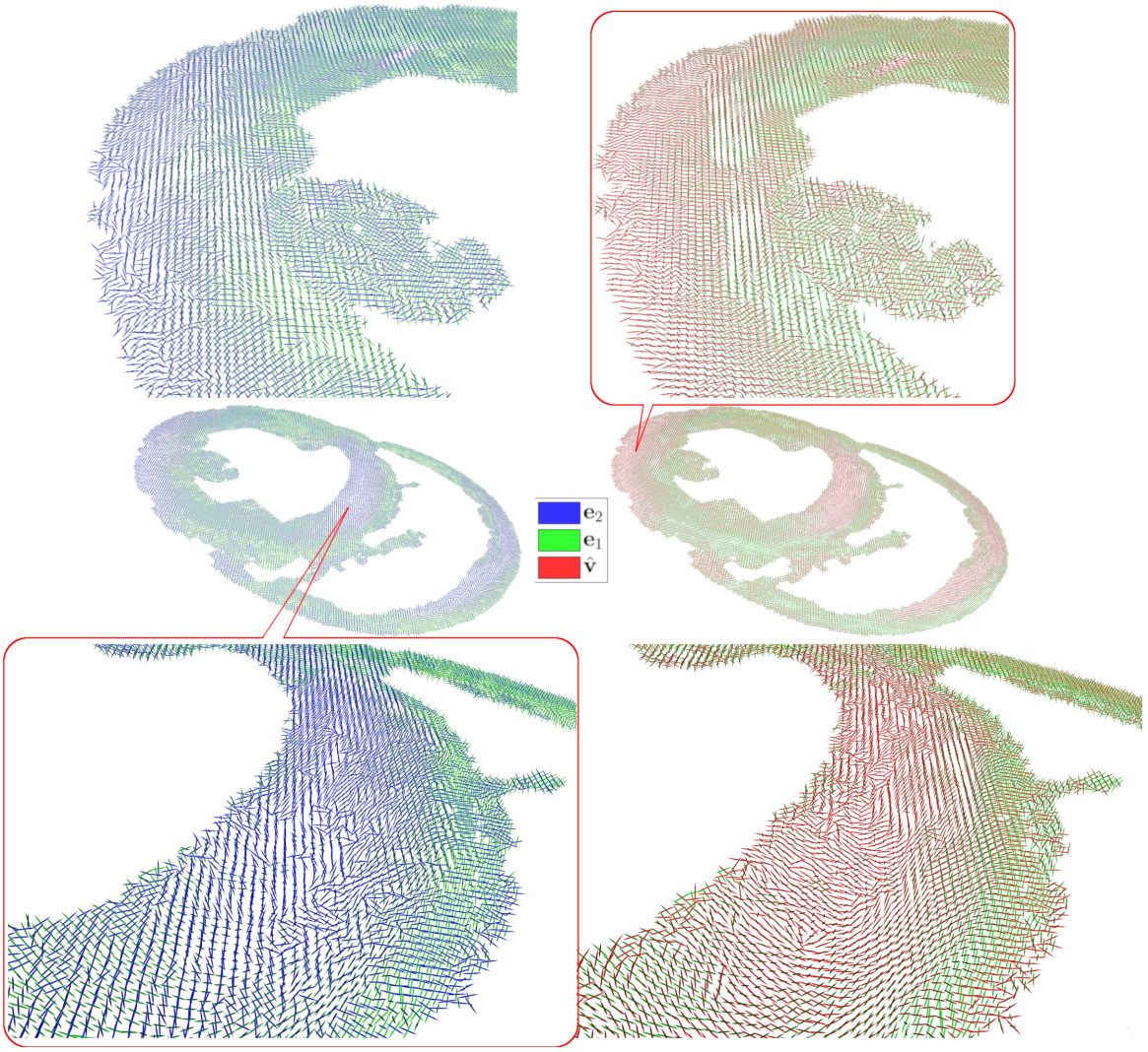

Figure 6.1: (Best viewed by zooming in on the electronic version of this thesis.) Using a sample slice from a canine heart (middle row) we focus on regions in the left ventricular wall (**top row**) and the septum (**bottom row**). In all panels the principal eigenvector direction $\mathbf{e}_1$ is shown in green. In the panels on the left the tensor eigenvector $\mathbf{e}_2$ is shown in blue. For comparison, in the panels on the right our estimated sheet direction vector $\hat{\mathbf{v}}$ is shown in red.

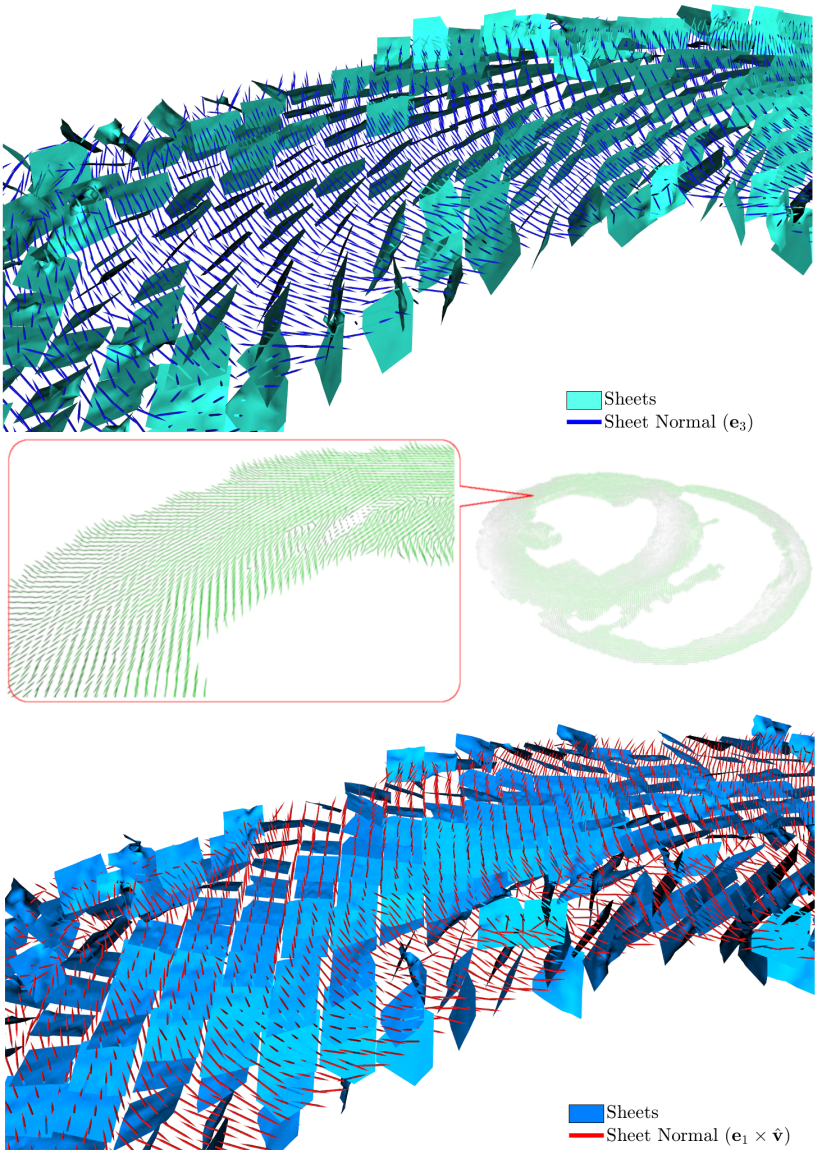

Figure 6.2: (Best viewed by zooming in on the electronic version of this thesis.) The **top** row shows the sheets spanned by $\mathbf{e}_1$ and $\mathbf{e}_2$ in cyan, with the corresponding normal vector $\mathbf{e}_3$ (blue). The **bottom** row shows our proposed sheets, spanned by $\mathbf{e}_1$ and $\hat{\mathbf{v}}$, in blue, along with our sheet normal vector $\mathbf{n} = \mathbf{e}_1 \times \hat{\mathbf{v}}$ (red). The **middle** row shows the zoomed-in region in the left ventricular wall from a short axis slice of the canine heart being analyzed, with the principal eigenvector $\mathbf{e}_1$ shown in green.

used second eigenvector $\mathbf{e}_2$ (blue) of the DTI tensor data. For clarity, the figures show a single short axis slice around the middle of a canine heart. In all panels, the principal eigenvector $\mathbf{e}_1$ is shown in green. Observe that in the lower right panel the estimated vector field $\hat{\mathbf{v}}$ (red) is relatively smooth, resembling the nature of $\mathbf{e}_1$ (green), as it should. In contrast, in the lower left panel the second eigenvector $\mathbf{e}_2$ (blue) is considerably noisier, even in smooth regimes of $\mathbf{e}_1$. As such, the sheet structure estimated using $\mathbf{e}_1$ and $\mathbf{e}_2$ would be noisy as well.

In Figure 6.2, we use the estimated vector field $\hat{\mathbf{v}}$ to draw sheets spanned by the vector fields $\mathbf{e}_1$ and $\hat{\mathbf{v}}$, and compare them with the sheets spanned by the vector fields $\mathbf{e}_1$ and $\mathbf{e}_2$. Local sheets are drawn by fitting a surface to points estimated by following streamlines along $\mathbf{e}_1$ and $\hat{\mathbf{v}}$. Specifically, we start at a grid point, say $\mathbf{r}$, and place it in a queue. We iteratively dequeue a point, follow the sheet by moving in the directions of $\pm\mathbf{e}_1$ and $\pm\hat{\mathbf{v}}$ at the point, and enqueue each neighboring point. In our implementation, we use bilinear interpolation to estimate the value of vector fields at non-grid points and we fit a sheet once 40 such points have been obtained.

In fact, even in the relatively smooth region shown in the top half of Figure 6.1, we observe in Figure 6.2 (top row) that the estimated sheets using $\mathbf{e}_1$ and $\mathbf{e}_2$ (cyan) are all oriented in a radial direction despite the varying myofiber orientation in the middle and border regions of the heart wall. The principal direction of fibers (shown in green in the middle row) are in the circumferential direction. However, the third eigenvector $\mathbf{e}_3$ (blue), which is normal to the sheets in cyan, does not follow this orientation. Our estimated normals $\mathbf{n} = \mathbf{e}_1 \times \hat{\mathbf{v}}$ (red), shown in the bottom row, are oriented in the long axis direction

in the middle of the wall and in the radial direction closer to the inner and outer walls. The sheets estimated using our computed normals better follow the local orientation $\mathbf{e}_1$ of the fibers.

6.2 Sheets estimated by non-holonomicity energy minimization

We begin by providing details about the data that we used and the implementation of the non-holonomicity energy minimization algorithm described in Section 5.2. Then, we illustrate our findings using our visualization Software.

Data: In order to validate our method we carried out a few experiments with data obtained from two sources. The first is the same one that we already described in Section 6.1. The second source is a dataset of labeled fiber tract systems in the human brain, constructed from a fiber bundle atlas generated from data from the Human Connectome Project, used in the ISMRM 2015 Tractography challenge [52]. This dataset is available for public download as well. The tangents at a list of points along fiber tracts from the data were used to generate our fixed direction vector field.

Modifying the energy function: As a corollary of our convergence analysis above, we infer from the bound on the energy gradient that a smoother energy function will have better convergence properties. This is, in fact, the case in practice, and we, therefore, used

a modified energy function $\hat{E}$ defined as

$$\hat{E}(\mathbf{u}, \mathbf{v}, \theta(\mathbf{x})) = \sum_{\hat{\mathbf{x}} \in Nbd(\mathbf{x})} \rho^2(\hat{\mathbf{x}}) \tag{6.1}$$

where $Nbd(\mathbf{x})$ is the neighbourhood of $\mathbf{x}$. We used a neighborhood size of $3 \times 3 \times 3$ in our experiments, since we are using first order estimates in the computation of derivatives. This energy converges for a wider range of choices of the step size η. Intuitively one may understand this modification as increasing the size of the neighborhood while calculating the deviation from sheet-like geometry at a point.

Choosing η: The convergence bound can also act as a guide to choosing the time step η, which is the only parameter other than the neighborhood size, in our approach. In accordance with the final convergence condition, we observed empirically that for brain tracts, the range of feasible η choices is smaller. This can be attributed to the more complex tract geometry in the brain compared to the heart. In fact, while larger η's worked well for simple tracts like the Inferior Longitudinal Fasciculus (ILF), more complex tract systems such as the corpus callosum (CC) required the use of a smaller η for convergence. Nonetheless, an η of 0.1, as shown in Figure 6.3, resulted in smooth convergence for every tract system, as predicted by our analysis.

Convergence rate: As shown by the plots in Figure 6.3, for our 3 datasets, with $\eta = 0.1$, the mean energy over all voxels in a dataset starts to flatten out after about 500 iterations. A quantitative analysis of the convergence rate is however beyond the scope of the present

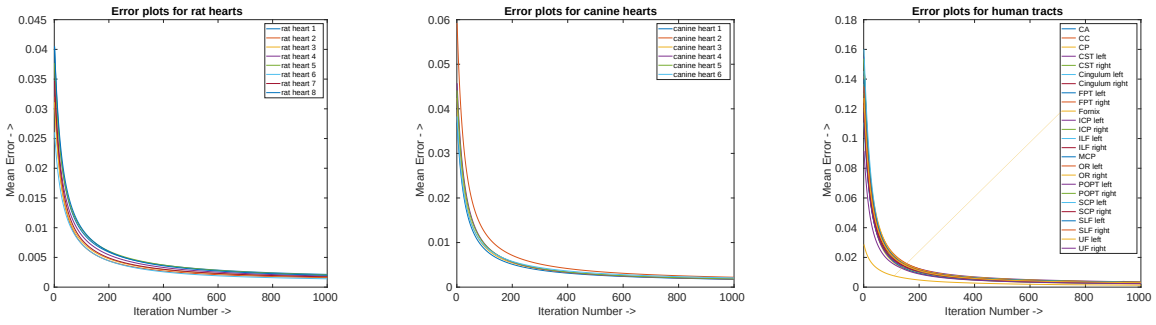

Rat Hearts Canine Hearts Human Brain Tracts

Figure 6.3: (Best viewed by zooming-in on the electronic version of this thesis.) Mean energy as a function of iteration number, for all examples reported in this section.

thesis, but we aim to take this up in the future.

Implementation and runtime: We implement our algorithm in the PyTorch framework [61]. To achieve this the derivatives and the spatial average calculations for the modified energy function are formulated as convolutions. This allows for GPU-based computation, which significantly reduces run-time and makes it feasible to analyze large datasets, in practical exploratory settings. We provide a comparison of run times on a CPU (Intel Core i9-7900x) and a GPU (Titan Xp), for volumes of different sizes in Table 6.1.

Sample	Size (Voxels)	CPU (s)	GPU (s)
Rat Heart	$64 \times 64 \times 128$	7.9	0.1
Canine Heart	$300 \times 300 \times 333$	279.3	5.6
Human Brain Tracts	$90 \times 108 \times 90$	11.0	0.1

Table 6.1: Time taken in seconds, per iteration, for a CPU based implementation versus that taken by a GPU based implementation, for different volumes.

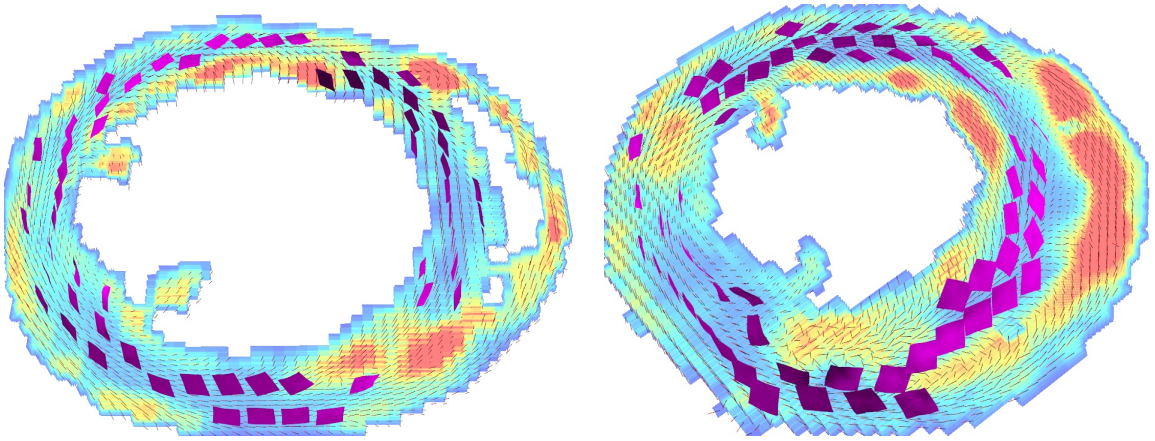

Rat1 Rat 2

Figure 6.4: (Best viewed by zooming-in on the electronic version of this thesis.) Estimates of sheet-likeliness in short axis slices of two rat hearts, illustrated with a volumetric jet colormap rendering (with the energy increasing from blue to red), along with our estimated sheets using the non-holonomicity energy minimization algorithm shown as magenta surfaces.

6.2.1 Sheet reconstruction and visualization

The output of our algorithm is a vector field $\mathbf{v}$ which is locally best in the sense of spanning a sheet with $\mathbf{u}$, together with an energy value at each voxel that is proportional to non-holonomicity. We use this final energy value as a guide for exploring and reconstructing sheets in the brain and the heart, in an iterative breadth first approach. At each step, we extend the sheet by a small quadrilateral sheetlet, composed of two triangular faces. The two triangular faces are generated by moving in the direction of $\mathbf{u}$ followed by $\mathbf{v}$ with a step size of around $ds = 0.2$ voxels, and then in direction $\mathbf{v}$ followed by $\mathbf{u}$. For sheet-like regions, the two triangular faces are expected to share an edge. In fact, the gap between the two triangular faces is proportional to the Lie bracket $[\mathbf{u}, \mathbf{v}]$ at a point. In

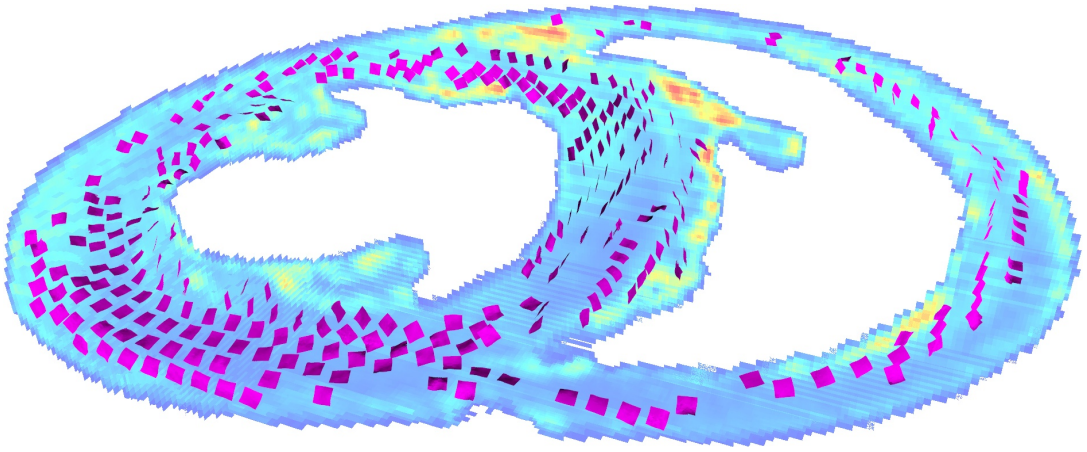

Canine 1

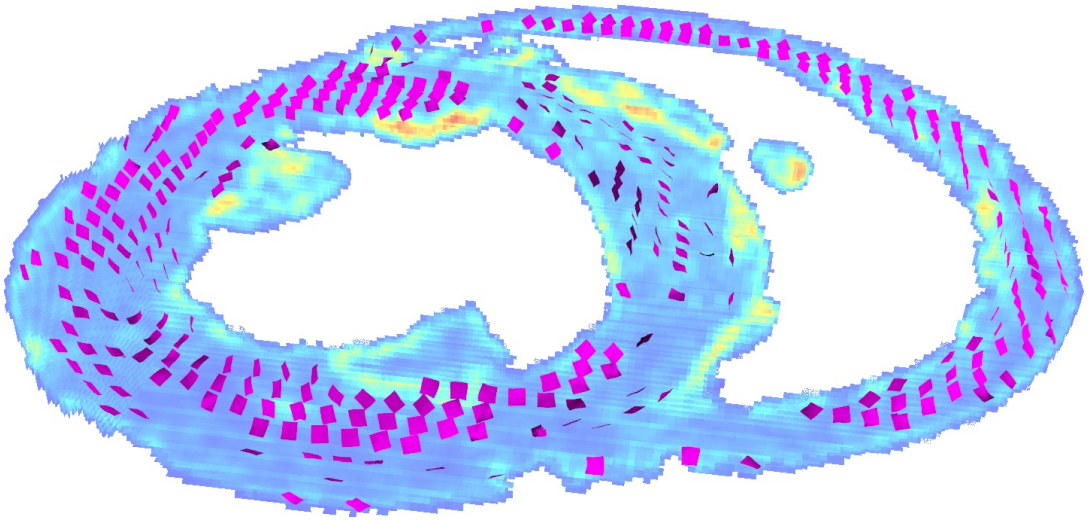

Canine 2

Figure 6.5: (Best viewed by zooming-in on the electronic version of this thesis.) Estimates of sheet likeliness in short axis slices of two canine hearts, illustrated with a volumetric jet colormap rendering (with the energy increasing from blue to red), along with our estimated sheets using the non-holonomicity energy minimization algorithm shown as magenta surfaces.

our visualizations, we only show sheets in locations with low energy. This reconstruction process is repeated n times (with $n \approx 7$) in all four $\pm\mathbf{u}$, $\pm\mathbf{v}$ directions, in a breadth-first traversal manner. Since the reconstructed points are not limited to voxel locations, we use distance from already drawn vertices, r, as a criterion for adding new points. The parameter r was fixed at half the step size. We developed an OpenGL based visualization tool for rendering all the results presented in this section. For the heart data, we draw sheets with uniform sampling in a given box (Figures 6.4 and 6.5), while for the brain data, we draw sheets, when supported, at locations uniformly sampled along the tracts (Figure 6.7).

Figures 6.4 and 6.5 present sheets reconstructed from diffusion tensor data for two rat hearts and two canine hearts, respectively. In all sub-figures we show a short axis slice, with a jet colormap volume rendering of the final sheet fitting energy (energy increases from cyan to red), and with our reconstructed sheets shown as magenta surfaces. For the rat hearts we also show the direction of the principal eigenvector as an orientation field. In both species, there is clear support for both axial sheets in the wall of the left ventricle (LV), consistent with the laminar organization reported via histology in early work [45], as well as regimes of more circumferential sheets. The geometry of sheets in the septum is more complex, being predominantly circumferential, and exhibiting a degree of fanning. The right ventricle (RV) also shows sheet-like geometries for the canine hearts, while for the rats the RV is squashed due to imaging conditions. Finally, the LV papillary muscles are associated with a higher energy, and thus a lower chance of being sheet-like, consistent with the property that along them muscle cells are oriented in the long axis direction. The sheet fitting energy is also high at the junctions of the LV and RV.

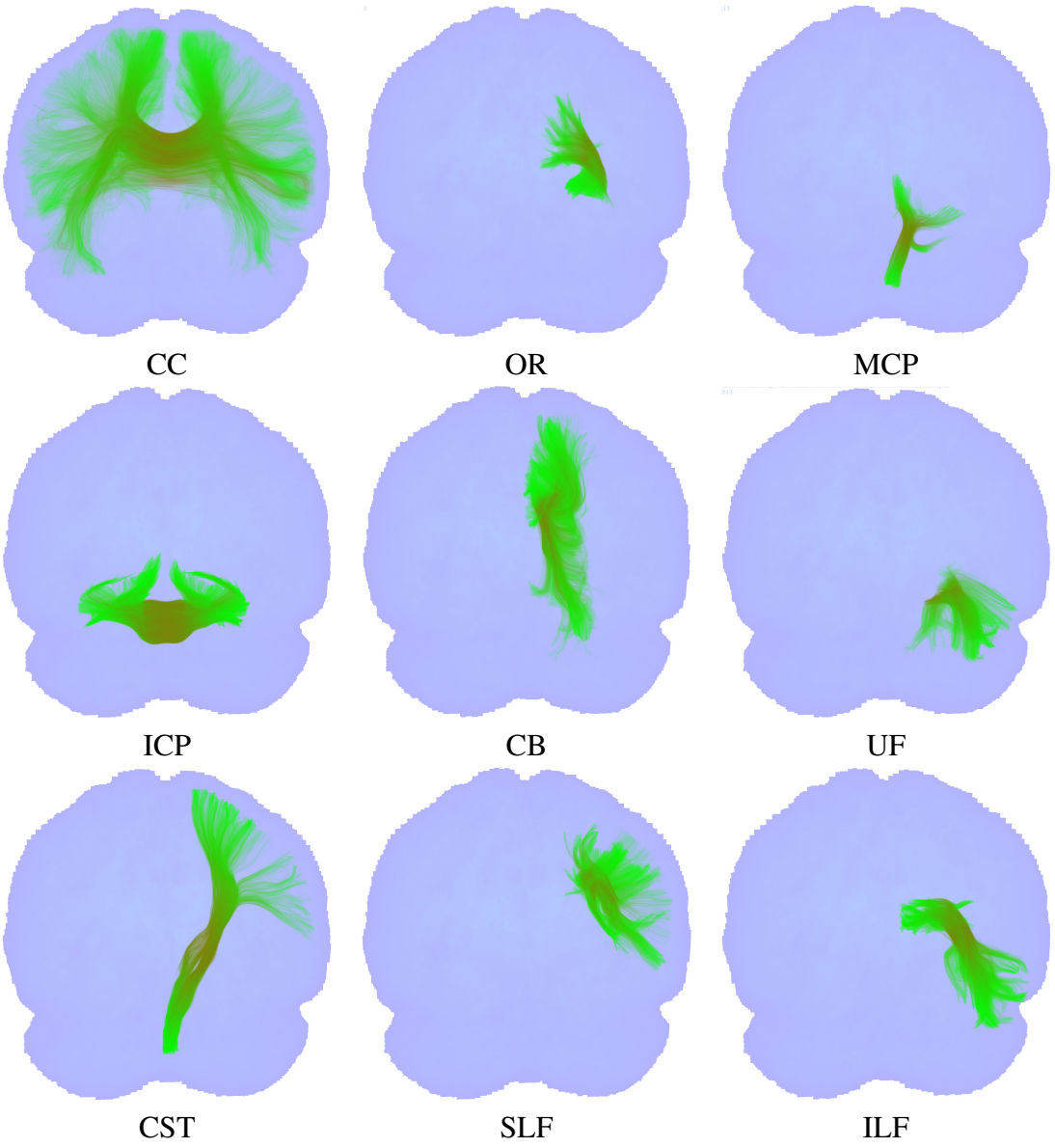

Figure 6.6: The HCP tracts analysed in Figure 6.7, shown in the context of their actual locations in the brain.

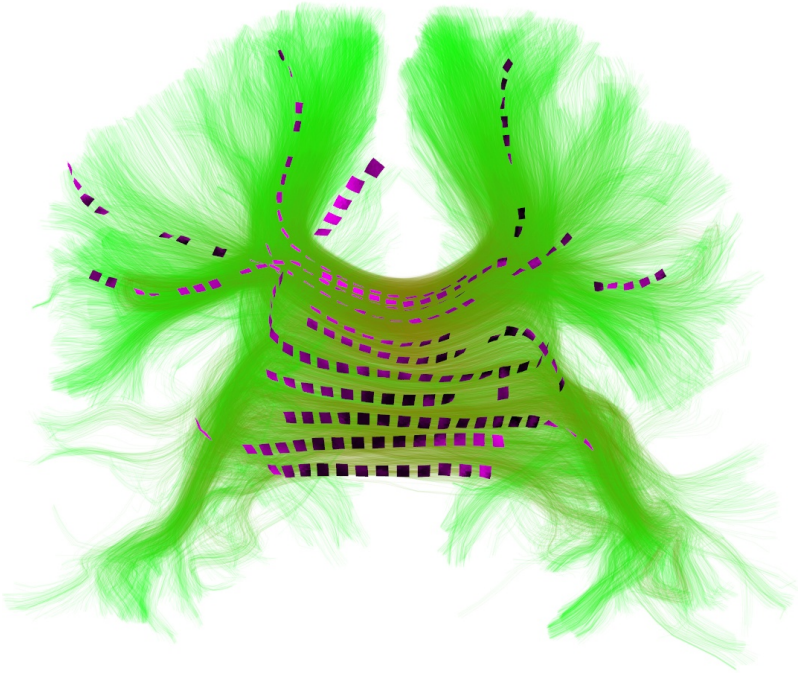

CC

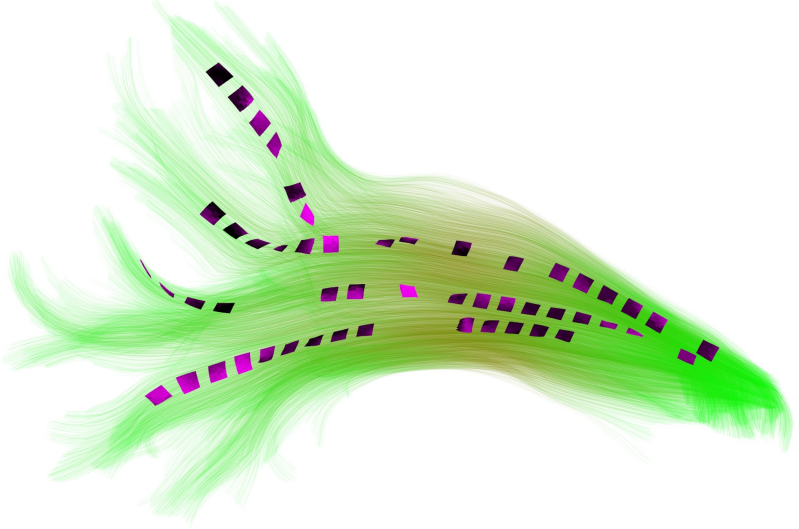

OR

6.2 Sheets estimated by non-holonomicity energy minimization

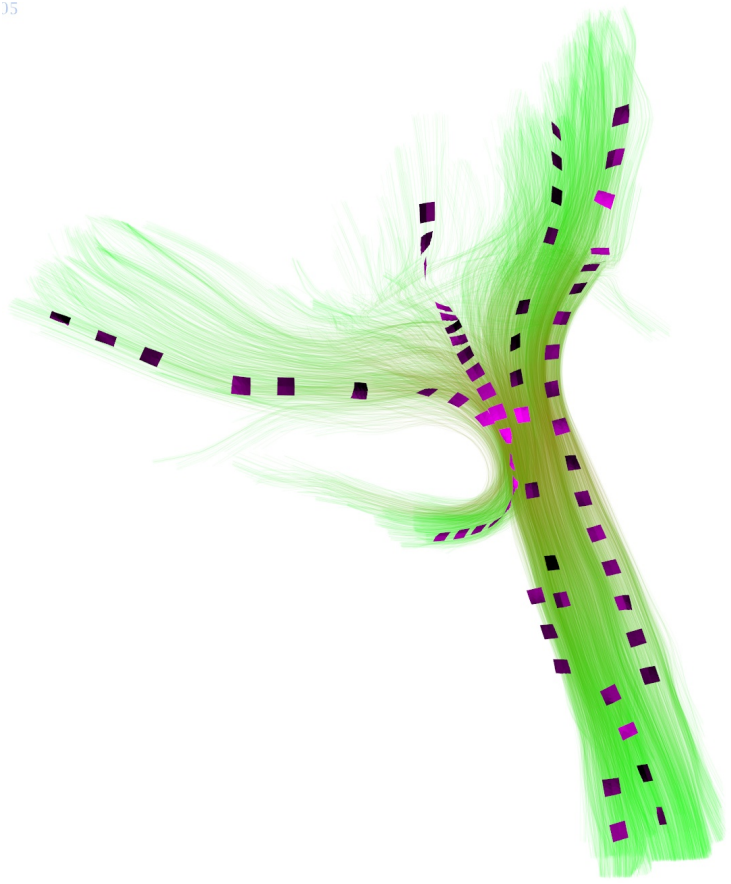

ICP

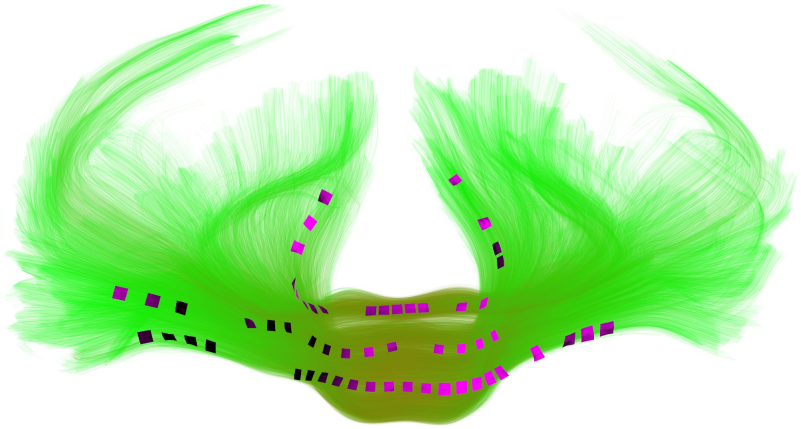

MCP

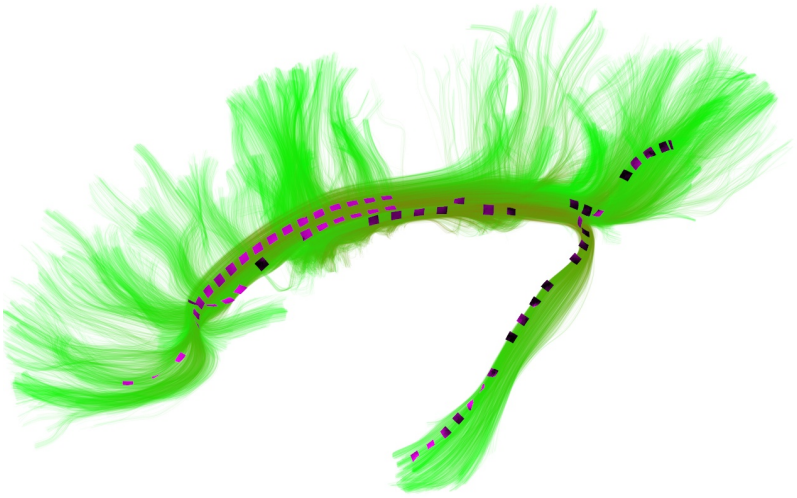

CB

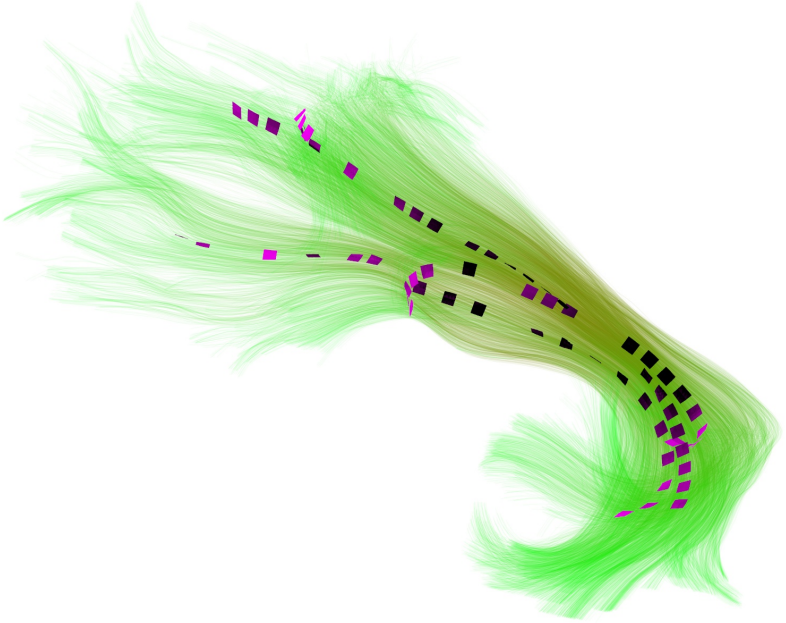

UF

6.2 Sheets estimated by non-holonomicity energy minimization

CST

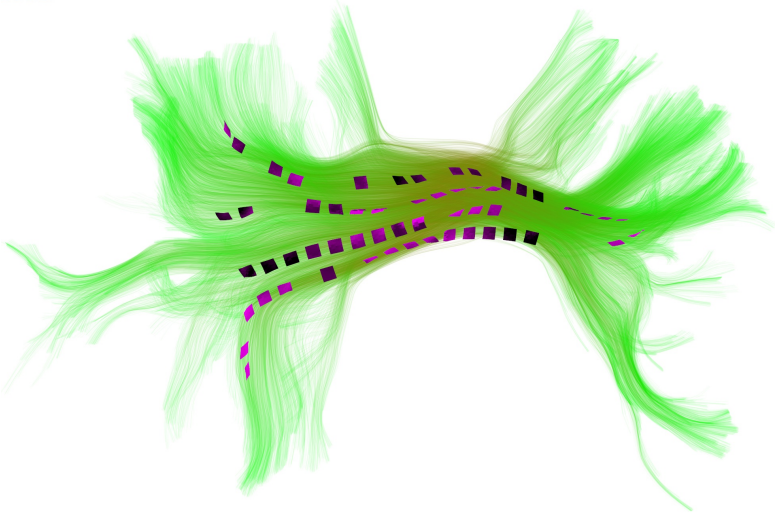

SLF

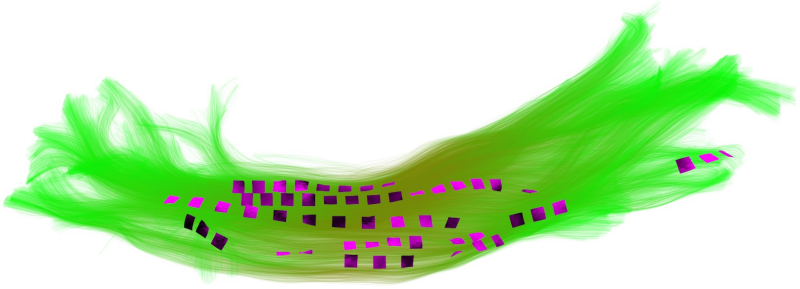

ILF

Figure 6.7: (Best viewed by zooming-in on the electronic version of this thesis.) Tract systems from an HCP atlas are shown with green streamlines, with the estimated sheets (where present) shown as magenta surfaces: corpus callosum (CC), optic radiation (OR), inferior cerebellar peduncle (ICP), middle cerebellar peduncle (MCP), cingulum bundle (CB), uncinate fasciculus (UF), corticospinal tract (CST), superior longitudinal fasciculus (SLF), and inferior longitudinal fasciculus (ILF).

Moving to the human brain, Figure 5.2 (bottom left) shows sheet fitting energy rendered as a jet colormap for the Fornix tract, with our recovered sheets shown as magenta surfaces (bottom right). We then consider many other tract systems, which are shown in the context of their actual positions in the full brain in Figure 6.6. For several of these we have chosen the left hemisphere tract to analyze. A number of these tract systems (CC, CB, SLF, Fornix) have been considered in cross species qualitative investigations of sheet geometry in [99], but with no explicit sheet reconstruction. Our recovered sheets for these tracts, where we find support, are depicted as magenta surfaces in Figure 6.7. The corresponding sheet fitting energies are rendered as a volumetric jet colormap in Figure 6.8. It is clear from Figures 5.2, 6.7, and 6.8, that whereas certain regimes of these tracts are indeed sheet-like (e.g. the two main arms of the Fornix, and the middle section of the CC), others, such as the fanning regions, are not. Our method allows for navigation and

labeling of a tract by the estimated value of the energy based on non-holonomicity, and for the quantitative recovery of subtle shape properties that thus far have been described only qualitatively. For example, the CST is more tube like, providing little local evidence of sheet geometries in most parts, while the MCP, SLF and ILF have large sheet-like regions.

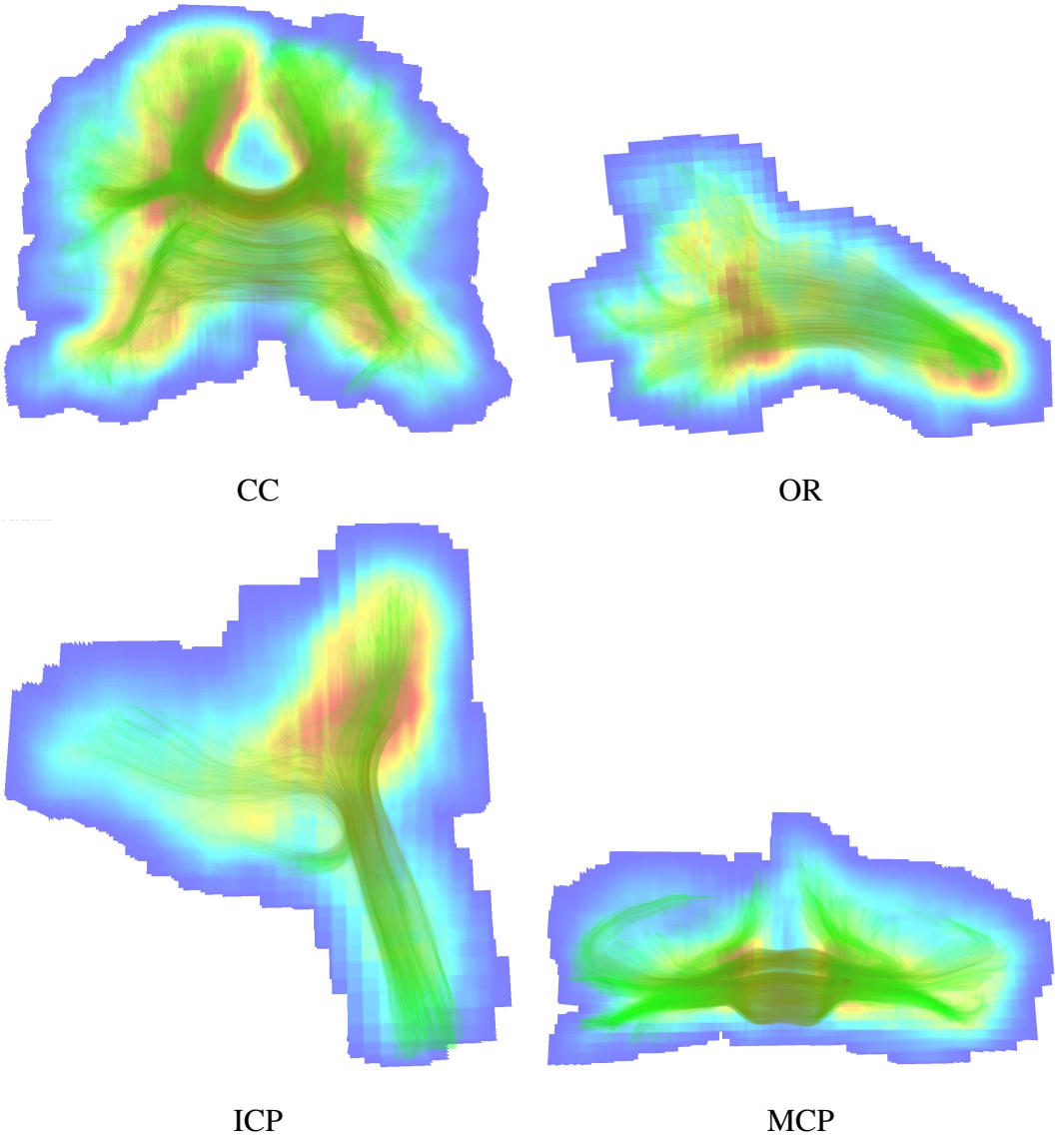

CC OR

ICP MCP

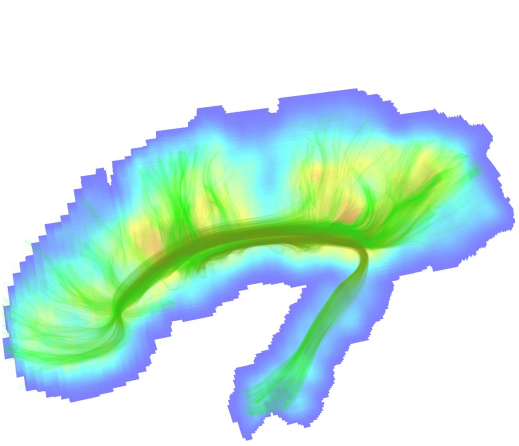

CB

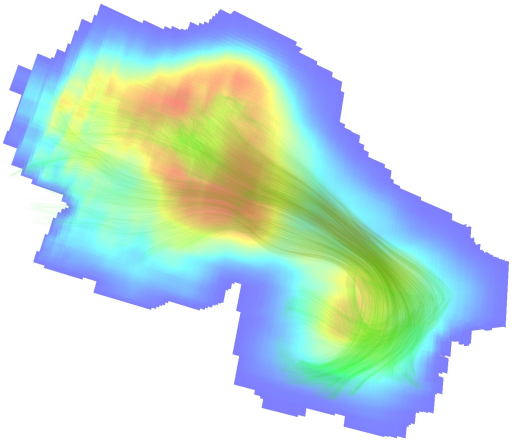

UF

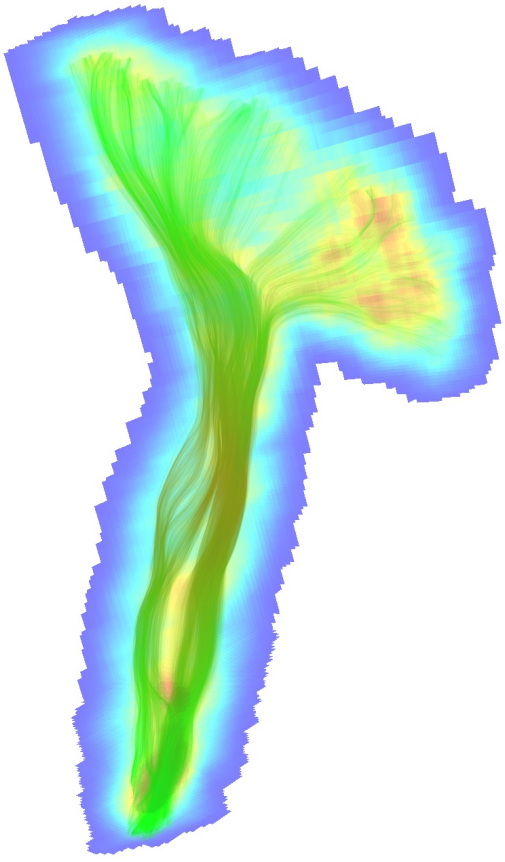

CST

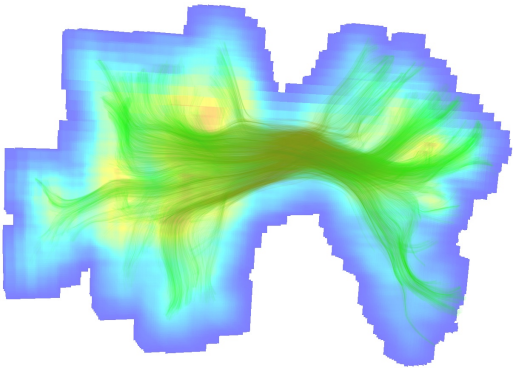

SLF

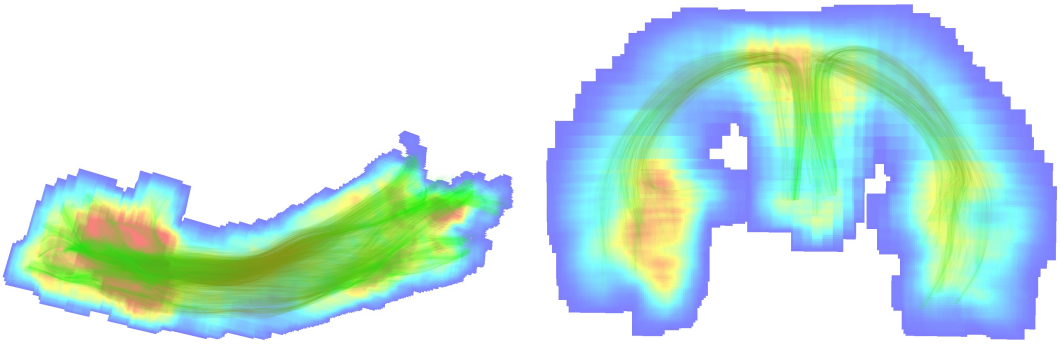

ILF Fornix

Figure 6.8: The HCP tracts analysed in Figure 6.7, shown superimposed on the final sheet fitting energy, visualized using volume rendering with a jet colormap (energy increases from cyan to red). The value of the final energy is proportional to the fitting error.

6.3 Discussion

In this part of the thesis, we have presented two methods for estimating a frame field spanning a sheet locally, from a single vector field. The first method minimizes an energy based on the Lie bracket, by using a gradient descent approach. We applied this algorithm to find sheets in ex vivo cardiac DTI data. This implementation demonstrated a promising proof of concept result. Then we designed an efficient algorithm which directly minimizes non-holonomicity. We showed that this algorithm converges and provided reconstructions and high quality visualizations of sheets on which myofibers in the heart are organized, or sheets on which fiber tract systems in the brain might lie, and provided a local measure of sheet-likeliness. Such an algorithm could now be used to settle questions concerning the geometric organization of tract systems as suggested in [99], in a quantitative and principled way.

Our result of sheet finding for the case of cardiac data is different from the one reported by Rohmer et al. [67], discussed in Section 3.3.3 of Chapter 3, in a subtle way. Their sheet tracking approach makes the assumption that sheetlets can only accrue in a radial orientation, in the short axis plane of the heart the wall. This will prevent their method from recovering other possible sheet orientations by design. As illustrated in Figures 6.2, 6.4, and 6.5, our sheet finding method does not have this limitation. We are able to recover sheets that are oriented axially (in the long axis plane of the heart wall) close to the epicardium and the septum, for both canine and rat heart datasets, as well as radial sheets in the mid-wall.

6.3 Discussion

Past analyses of tract geometry in the human brain have asked the question whether *two* local directions, often taken to be the peak directions of a fiber orientation distribution function [86, 87], or the first and second principal directions of a diffusion tensor [1], provide support for sheets. These attempts have had success in designing sheet probability measures by considering the normal component of the Lie bracket. The problem we have studied here is different in a subtle way, namely, we have asked whether a *single* direction field derived from fibrous tissue supports sheet-like geometries.

Ultimately, a gold standard for validating our sheet estimates would be given by reconstructions of the sheets revealed by histology. Reconstructing sheet structure from histological sections and comparing such reconstructions with DTI measurements are worthwhile but challenging goals, which are beyond the scope of the present dissertation.

Part III

Part III: Moving Frames for Moving Fibers

7

Introduction

The contents of this part are largely based on the articles: “Cartan Frames For Heart Wall Fiber Motion”[69], and “Denoising Moving Heart Wall Fibers Using Cartan Frames”[70]. This part of the thesis develops a spatio-temporal approach, using moving frames, to model the motion of cardiac myofibers during the heart beat cycle. The approach is an extension of the method developed in [65].

Mammalian heart wall muscle is comprised of densely packed elongated myocytes in an extra-cellular matrix [21, 58]. The geometry of this packing facilitates efficient pumping to optimize ejection fraction while also providing strength. The precise manner in which fibers move and rotate with the material medium in which they are placed during the cardiac beat cycle is as yet not known. Current models of heart wall fiber geometry are mostly derived from diffusion imaging of static ex vivo hearts and from histology.

Models do exist for such data, such as the rule-based model of [5], and the techniques in [34]. Studying the 3D structure of an arbitrary collection of 3D streamlines is also possible by considering their differential form representation. A notion of connection forms by Cartan [11] introduces a method of moving frames to describe the structure of smooth manifolds. Ehresmann [19] applies this formalization to abstract the geometry of a collection of streamlines. Piuze et al. [65] use the method of moving frames and associated connection form parameters to characterize the geometry of fibers with an application to the myocardium. Although measuring fiber orientation using ex vivo DTI is a well established approach, these methods lack a temporal dimension to capture fiber rotation as the heart beats.

Whereas there is on-going progress in our community towards in vivo cardiac diffusion imaging, with the possibility to now acquire full heart fiber orientation data in beating hearts [83, 24], the mathematical tools for analysis lag behind. In this part of the thesis, we shall develop Cartan connection forms [79, 60] to model both spatial (within a time sample) and temporal (between time sample) rotations of frame fields attached to heart wall fibers. This allows one to capture spatial and temporal geometric signatures within a single consistent framework. In Chapter 2, Section 3.5, we reviewed Cartan connection forms and their use in moving frame methods. Extending a method for the case of static fibers, in Chapter 8, we add a temporal dimension to the Cartan matrix. We then specialize the model by adapting frames fit to heart wall myofiber orientations recovered from diffusion data. In Chapter 9, we demonstrate the promise of this method for the recovery of geometric curvature type spatio-temporal signatures for moving myofibers during a heart beat cycle, using both finite element simulation on canine data [9] and human in

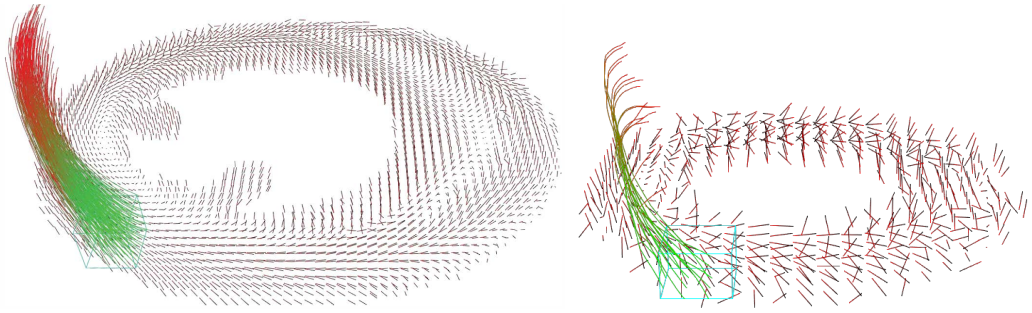

Figure 7.1: DT reconstruction of fiber orientations with tractography run from a local region. Left: Ex vivo rat heart (LV and RV). The data is from the open access repository in [76]. Right: New in vivo human heart (LV).

vivo cardiac diffusion imaging.

In a related application of moving frame methods, we also address the problem of detecting outliers in diffusion MRI based reconstructions of myofiber orientations. In the context of in vivo diffusion imaging of the human heart, which is an area of active research and ongoing progress [83, 24, 90], the recovered fiber orientations may be locally incoherent, despite denoising being applied prior to tensor fitting, with the spatial resolution being poor, as illustrated for the left ventricle in Figure 7.1 (right). We address the problem of detecting outliers in in vivo mammalian diffusion tensor reconstructions from a geometrical perspective. We do so by introducing a 4D (spatio-temporal) Cartan frame, which, when fit to measured data, allows us to characterize the distributions of Cartan form parameters. Using these distributions, one can then determine the degree to which a particular local frame fit to the data is predicted by the estimated distributions. This allows us to both detect outliers, and then remove and in-paint the missing regions. Our experiments in Chapter 9 on simulated moving fibers in a canine heart wall from the Statistical Atlases and Computational Models of the Heart (STACOM) 2014 LV mechanics

challenge show that our statistical approach is capable of robustly and accurately identifying areas with incoherent fiber orientations. We also demonstrate the applicability of our algorithm to human in vivo heart wall fiber data.

8

Methods

In this chapter, we first develop a spatio-temporal model that can describe the motion of myofibers both in space and time using a moving frame approach. We then construct two beating heart datasets: a canine dataset obtained by finite element simulation, and new in vivo human data that is suitable for our spatio-temporal connection form model, while assuming a notion of correspondences between material points of different time samples. Finally, to demonstrate an application of our method, we introduce a distribution fitting method to the calculated connection form parameters, which is able to distinguish irregular structures, i.e., geometrical outliers in our datasets.

8.1 Spatio-temporal connection forms

Following our discussion in Chapter 3, Section 3.5, we assume that for any query time $t \in \mathbb{R}$ we have a stationary state of an orthonormal moving frame field $F^t = [\mathbf{f}_1, \mathbf{f}_2, \mathbf{f}_3]^T$ fitted to left ventricular myofibers, with the corresponding universal coordinate $E^t =$

$[\mathbf{e}_1, \mathbf{e}_2, \mathbf{e}_3]^T$. We add a 4th dimension to the 3D coordinate system to represent the time axis. Let $E = [\mathbf{e}_1, \mathbf{e}_2, \mathbf{e}_3, \mathbf{e}_4]^T$ represent our extended universal coordinate system, $\mathbb{R}^4$, in-which $\mathbf{e}_i \cdot \mathbf{e}_j = \delta_{i,j}$, where $\delta_{i,j}$ is the Kronecker delta, and $\mathbf{e}_4 = [0, 0, 0, 1]^T$ is a basis vector for the time axis in the 4D representation. Thus a query $(x, y, z, t) \in \mathbb{R}^4$, represents a point (x, y, z) in E^t. We extend the 3D orthonormal local frame F^t as follows:

Definition 7 *Let* $F^t = [\mathbf{f}_1, \mathbf{f}_2, \mathbf{f}_3]^T = \begin{bmatrix} \mathbf{f}^t_{1,x} & \mathbf{f}^t_{1,y} & \mathbf{f}^t_{1,z} \\ \mathbf{f}^t_{2,x} & \mathbf{f}^t_{2,y} & \mathbf{f}^t_{2,z} \\ \mathbf{f}^t_{3,x} & \mathbf{f}^t_{3,y} & \mathbf{f}^t_{3,z} \end{bmatrix}$ *describe an orthonormal frame field in* $\mathbb{R}^3$ *at time* t*, then:*

$$\begin{bmatrix} \mathbf{f}^t_{1,x} & \mathbf{f}^t_{1,y} & \mathbf{f}^t_{1,z} & 0 \\ \mathbf{f}^t_{2,x} & \mathbf{f}^t_{2,y} & \mathbf{f}^t_{2,z} & 0 \\ \mathbf{f}^t_{3,x} & \mathbf{f}^t_{3,y} & \mathbf{f}^t_{3,z} & 0 \\ 0 & 0 & 0 & 1 \end{bmatrix} \tag{8.1}$$

is its $4D$ *extension.*

This extension preserves the spatial properties of the static case via its 3×3 top left submatrix, while accounting for the temporal motion using its last row and column. Since we know that $F^t = [\mathbf{f}_1, \mathbf{f}_2, \mathbf{f}_3]^T$ is an orthogonal matrix, it is not hard to show that $F = [\mathbf{f}_1, \mathbf{f}_2, \mathbf{f}_3, \mathbf{f}_4]^T$ is also orthogonal, i.e., $\forall i \neq j, \mathbf{f}_i \cdot \mathbf{f}_j = 0$.

Now we can define the notion of spatio-temporal connection forms in 4D. Let $F = [\mathbf{f}_1, \mathbf{f}_2, \mathbf{f}_3, \mathbf{f}_4]^T$ be an arbitrary frame field on $\mathbb{R}^4$, with the following parametrization in the

extended universal coordinate system $E = [\mathbf{e}_1, \mathbf{e}_2, \mathbf{e}_3, \mathbf{e}_4]^T$:

$$\begin{aligned}
\mathbf{f}_1 &= \alpha_{11}\mathbf{e}_1 + \alpha_{12}\mathbf{e}_2 + \alpha_{13}\mathbf{e}_3 + \alpha_{14}\mathbf{e}_4, \\
\mathbf{f}_2 &= \alpha_{21}\mathbf{e}_1 + \alpha_{22}\mathbf{e}_2 + \alpha_{23}\mathbf{e}_3 + \alpha_{24}\mathbf{e}_4, \\
\mathbf{f}_3 &= \alpha_{31}\mathbf{e}_1 + \alpha_{32}\mathbf{e}_2 + \alpha_{33}\mathbf{e}_3 + \alpha_{34}\mathbf{e}_4, \\
\mathbf{f}_4 &= \alpha_{41}\mathbf{e}_1 + \alpha_{42}\mathbf{e}_2 + \alpha_{43}\mathbf{e}_3 + \alpha_{44}\mathbf{e}_4.
\end{aligned} \tag{8.2}$$

A covariant derivative of this frame field with respect to a vector $\mathbf{v}$ at point p is given by

$$\begin{aligned}
\nabla_{\mathbf{v}}\mathbf{f}_1 &= \omega_{11}(\mathbf{v})\mathbf{f}_1(p) + \omega_{12}(\mathbf{v})\mathbf{f}_2(p) + \omega_{13}(\mathbf{v})\mathbf{f}_3(p) + \omega_{14}(\mathbf{v})\mathbf{f}_4(p), \\
\nabla_{\mathbf{v}}\mathbf{f}_2 &= \omega_{21}(\mathbf{v})\mathbf{f}_1(p) + \omega_{22}(\mathbf{v})\mathbf{f}_2(p) + \omega_{23}(\mathbf{v})\mathbf{f}_3(p) + \omega_{24}(\mathbf{v})\mathbf{f}_4(p), \\
\nabla_{\mathbf{v}}\mathbf{f}_3 &= \omega_{31}(\mathbf{v})\mathbf{f}_1(p) + \omega_{32}(\mathbf{v})\mathbf{f}_2(p) + \omega_{33}(\mathbf{v})\mathbf{f}_3(p) + \omega_{34}(\mathbf{v})\mathbf{f}_4(p), \\
\nabla_{\mathbf{v}}\mathbf{f}_4 &= \omega_{41}(\mathbf{v})\mathbf{f}_1(p) + \omega_{42}(\mathbf{v})\mathbf{f}_2(p) + \omega_{43}(\mathbf{v})\mathbf{f}_3(p) + \omega_{44}(\mathbf{v})\mathbf{f}_4(p),
\end{aligned} \tag{8.3}$$

where $[\alpha_{ij}] = [\mathbf{f}_i \cdot \mathbf{e}_j]$ is the attitude matrix in $\mathbb{R}^4$ and $\omega_{ij} = \sum_k (d\alpha_{ik})\alpha_{kj}$ is a 1-form, as discussed in Chapter 2, Section 3.5.

Definition 8 *Let $i < j$ and $i, j, k \in \{1, 2, 3, 4\}$. By using the frame field's unit vectors ($\mathbf{f}_i$s) as arguments to $\omega_{ij}(\mathbf{v})$ we have*

$$c_{ijk} = \omega_{ij}(\mathbf{f}_k). \tag{8.4}$$

Note 5 *For $j = 4$, $c_{ijk} = \omega_{ij}(\mathbf{f}_k) = 0$, because space and time are independent of each other.*

Note 6 *For a point p and with $i < j \in \{1, 2, 3\}$, $\omega_{ij}(\mathbf{f}_k)$ represents the amount of $\mathbf{f}_i(p)$'s*

turn in the direction of $\mathbf{f}_j(p)$ *when taking a step towards* $\mathbf{f}_k(p)$.

Then, given the skew-symmetry property for the 4×4 connection form matrix, we build $3 \times 4 = 12$ different non-zero and unique c_{ijk}s.

We can use these coefficients to estimate the motion of the frame field using first order approximation of the Taylor expansion of the frame field F in the direction of the vector $\mathbf{v}$ at a point p

$$\mathbf{f}_i(\mathbf{v}) \simeq \mathbf{f}_i(p) + d\mathbf{f}_i(\mathbf{v}). \tag{8.5}$$

Finally, by applying the Cartan structural Equation (3.9) on the Equation (8.5), where $\mathbf{v} = \sum_k \mathbf{v}_k \mathbf{f}_k$, we have

$$\mathbf{f}_i(\mathbf{v}) \simeq \mathbf{f}_i(p) + \sum_j \left(\sum_k v_k c_{ijk} \right) \mathbf{f}_j(p). \tag{8.6}$$

We now show how to calculate the 1-form coefficients of a given 4D frame. From the definition of the c_{ijk}s in [65] and their first order Taylor expansions, for an arbitrary vector $\mathbf{v}$ at point p, and $i, j, k, n \in \{1, 2, 3, 4\}$ we can re-write Equation (3.9) as

$$c_{ijk} = \omega_{ij}(\mathbf{f}_k) = {\mathbf{f}_j}^T J(\mathbf{f}_i)\mathbf{f}_k, \tag{8.7}$$

where $J(\mathbf{f}_i) = [\frac{\partial \mathbf{f}_{ij}}{\partial x_k}]$ is a Jacobian matrix. Given a discretized frame field, we then apply Equation (8.7) to calculate the connection form coefficients. We illustrate the above extension by a simulation in Figure 8.1, where we consider an initial fiber direction, with an attached frame field, and then apply a specific set of c_{ijk}s to it. Here, $\mathbf{f}_1$ is in the direction of the fiber, $\mathbf{f}_3$ is in the in-page direction orthogonal to $\mathbf{f}_1$, and $\mathbf{f}_2 = \mathbf{f}_3 \times \mathbf{f}_1$. The figure (left

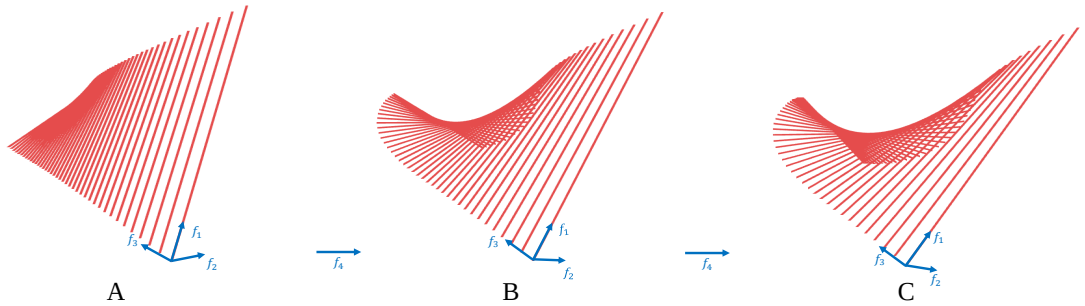

Figure 8.1: The application of a specific set of 4D connection parameters c_{ijk} to a frame field attached to a fiber direction. The sequence from left to right represents increasing time, i.e., steps in the direction $\mathbf{f}_4$. See text for the discussion.

to right) shows three samples in time of the orientations in the local neighborhood of the fiber, generated with the parameters $c_{123} = 0.5$ radians/voxel, $c_{124} = 0.03$ radians/time-step, and $c_{ijk} = 0$ for all the remaining connection parameters. The positive c_{123} value results in a clockwise rotation of fibers in the in-page direction (panel A) and the positive c_{124} value results in an increase in the total in-page rotation of fibers in time (panels B and C).

8.2 Beating heart fiber data

We construct two data sets for evaluating our moving frame method for modeling fibers in the heart wall. The first is derived from a finite element simulation applied to canine hearts from the STACOM 2014 LV mechanics challenge [9]. The second is from new in vivo diffusion imaging of an entire human heart [23].

8.2.1 Canine data (STACOM 2014)

In this challenge in vivo MRI data from four normal dogs were given as hexahedral meshes (at the beginning of the beat cycle), with associated local cardiomyocyte fiber

orientations from the first principal eigenvector of ex vivo diffusion tensor MRI data. The data also included an endocardial pressure curve and the positions of several reference points on the base of the left ventricle, at three points in the beat cycle. These positional constraints were interpolated across the LV base by radial basis function interpolation in space and linearly in time. The participants were asked to build a model that simulates the contraction behavior of the left ventricle and matches its ejection fraction. We use this data to get pointwise correspondences of material points in time. By rotating the cardiac frame field arbitrarily in-time in a controlled manner, we then applied our connection form parameter estimation to measure these changes in a spatio-temporal setup. We used this data for a finite element simulation of the heart wall based on the transversely isotropic Holzapfel-Ogden constitutive equations, which describe a non-linearly elastic incompressible material designed to model the empirical behavior of the cardiac tissue [36]. This has the following strain energy:

$$\Psi = \frac{a}{2b}\exp(b[I_1 - 3]) + \frac{a_f}{2b_f}[\exp(b_f[I_{4f} - 1]^2) - 1]$$

where $I_1 = \text{tr}(C)$, $I_{4f} = \mathbf{f}_1 \cdot C\mathbf{f}_1$, $C = F^T F$ is the right Cauchy-Green strain tensor, F is the deformation gradient, $\mathbf{f}_1$ is the local fiber direction vector in the reference configuration, and $a, b, a_f, b_f \in \mathbb{R}$ are constants. The time-varying active contraction of the fibers was modeled via the formalism of Guccione and McCulloch [31], where a time-dependent active stress component is added to the passive Cauchy stress above.

The simulation, including the transversely isotropic Holzapfel-Ogden material model and the enforced fiber rotation (below), was implemented in FEBio [51] as a plugin. We

fixed $a = 4$, $b = 5$, $a_f = 10$, $b_f = 5$, based on parameters from previous work [32]. This yielded a 3D point cloud moving over time, with a local frame attached to each point that is amenable to connection form estimation. We then devised a strategy for combining the finite element simulation with a controlled rotation of the fibers over time, as explained below.

Generating sample moving frames

In the chronological sequence of my research, for the case of simulation data, I considered the method described in [65, 75] for fitting frames to the cardiac data. As in the example in Figure 8.1, let $\mathbf{f}_1$ be a unit vector in the direction of a fiber, $\mathbf{f}_3$ the component of the heart wall normal orthogonal to $\mathbf{f}_1$ and $\mathbf{f}_2$ be $\mathbf{f}_3 \times \mathbf{f}_1$. We control the fiber orientations during simulation by rotating them over time, with a frame field formalized as follows:

$$\begin{aligned}
\mathbf{f}_1(\mathbf{x}) &= \mathbf{v}_{\text{fib}}(\mathbf{x}) \\
\mathbf{f}_3(\mathbf{x}) &= \frac{\widehat{\mathbf{f}}_3(\mathbf{x}) - (\widehat{\mathbf{f}}_3(\mathbf{x}) \cdot \mathbf{f}_1(\mathbf{x}))\mathbf{f}_1(\mathbf{x})}{||\widehat{\mathbf{f}}_3(\mathbf{x}) - (\widehat{\mathbf{f}}_3(\mathbf{x}) \cdot \mathbf{f}_1(\mathbf{x}))\mathbf{f}_1(\mathbf{x})||_2} \\
\mathbf{f}_2(\mathbf{x}) &= \mathbf{f}_3(\mathbf{x}) \times \mathbf{f}_1(\mathbf{x}).
\end{aligned}$$

Here $\mathbf{v}_{\text{fib}}(\mathbf{x})$ is the material fiber orientation at a given position $\mathbf{x}$, and the heart wall normal $\widehat{\mathbf{f}}_3(\mathbf{x})$ is given by:

$$\widehat{\mathbf{f}}_3(\mathbf{x}) = \frac{1}{2}(\nabla d_{\text{endo}}(\mathbf{x}) - \nabla d_{\text{epi}}(\mathbf{x})).$$

Let $d_{\text{endo}}(\mathbf{x})$ and $d_{\text{epi}}(\mathbf{x})$ represent the Euclidean distance from a point $\mathbf{x}$ in the myocardium to the closest points on the endocardium and the epicardium, respectively. We then con-

sider the estimation of wall position P_w of a given material point, ranging from -1 (endocardium) to 1 (epicardium): $\widehat{P}_w(\mathbf{x}) = d_{\text{endo}}(\mathbf{x}) - d_{\text{epi}}(\mathbf{x})$ and then normalized via

$$P_w(\mathbf{x}) = \frac{2\left(\widehat{P}_w(\mathbf{x}) - \min_{\mathbf{v}} \widehat{P}_w(\mathbf{v})\right)}{\max_{\mathbf{v}} \widehat{P}_w(\mathbf{v}) - \min_{\mathbf{v}} \widehat{P}_w(\mathbf{v})} - 1.$$

From this, we can apply a rotation to the fiber orientation as a function of time and wall position. Let t_{onset} be the time of onset of the cardiac contraction, t_{max} be the time of peak contraction during systole, and θ_{max} be the largest magnitude of angle change permitted at the contraction peak. Then we define the angular change over time to be:

$$\theta(\mathbf{x}, t) = \frac{P_w(\mathbf{x})(t - t_{\text{onset}})\pi\theta_{\text{max}}}{2(t_{\text{max}} - t_{\text{onset}})}.$$

Notice that the magnitude of angular rotation increases linearly in both time and $|P_w(\mathbf{x})|$. This allows us to rotate the fiber rotation over time via Rodrigues' rotation formula:

$$\widetilde{\mathbf{f}}_1(\mathbf{x}, t) = \mathbf{f}_1(\mathbf{x})\cos(\theta(\mathbf{x}, t)) + [\mathbf{f}_1(\mathbf{x}) \times \mathbf{f}_3(\mathbf{x})]\sin(\theta(\mathbf{x}, t)) + [\mathbf{f}_1(\mathbf{x}) \cdot \mathbf{f}_3(\mathbf{x})][1 - \cos(\theta(\mathbf{x}, t))]\mathbf{f}_3(\mathbf{x}).$$

8.2.2 In vivo human data

Data of a single healthy volunteer was acquired on a 3T scanner (Philips, Achieva) using a 32-channel cardiac coil. DWI was performed using a SE sequence with cardiac triggering in free breathing with asymmetric bipolar gradients [83, 24] and additional compensation for the slice and readout gradients. Data was acquired with 150 and 220 ms delays after the cardiac trigger and b-values of 0, 10, 20, 30, 50, 100, 200, and 400 s/mm^2 with 6,

3, 3, 3, 3, 3, 3, and 24 gradient-directions, respectively. Imaging parameters were; TE=62 ms; TR = 14 heart beats; FOV = 280 x 150 mm^2 (using outer volume suppression using rest slabs); slices = 14; voxel size = 7 x 2.5 x 2.5 mm^3; acquisition matrix = 112 x 48 SENSE factor = 2.5; partial Fourier= 0.85; EPI bandwidth = 42 Hz/pix; averages = 1; fat suppression = SPAIR; Gmax = 62 mT/m; max slope = 100 $mT/m/ms$ and acquisition time = 13 min.

Data processing was done using DTITools for Mathematica 10 and included the registration to correct for subject motion and eddy current deformations, noise suppression and tensor calculation using weighted linear least squares estimation [22] with the ventricles segmented manually using ITK-SNAP [103]. The primary eigenvector of the tensors within the left ventricle was extracted and used for subsequent analysis.

To fit a frame field to the in vio DTI, as proposed in Part II, we use the energy minimizing approach only on $\mathbf{e}_1$ and estimate the vector field $\mathbf{v}$ normal to it such that it maximizes sheet-likeliness and therefore minimized the non-holonomicity energy.

Definition 9 ***Sheet-based coordinate system:*** *Given an estimated* $\mathbf{v}(\mathbf{e}_1)$ *using the non-holonomicity energy minimization algorithm of Part II, the local coordinate system with the bases* $F = [\mathbf{f}_1 = \mathbf{e}_1, \mathbf{f}_2 = v, \mathbf{f}_3 = \mathbf{e}_1 \times v]^T$ *plays the role of a sheet-based coordinate system.*

This coordinate system has the benefit that it does not make any explicit assumptions about the geometry of the heart and at the same time, it is in accordance with the local sheet-like geometry of myofibers where supported. A more detailed discussion of different methods of fitting frames to cardiac DTI appears in Appendix B.

8.3 Obtaining material point correspondences

To apply the spatio-temporal connection form method to real data, we need all the time samples to be registered. In other words, in the process of calculating c_{ijk}s, for $k = 4$, we assume that the time neighbor of any query point (x, y, z, t) is the point at coordinate $(x, y, z, t \pm \epsilon)$ for a small enough ϵ. This assumption may not always hold, unless we are able to acquire dense enough time samples which are registered to a template frame. For the case of simulation data, as described in Section 8.2.1, we are able to control the temporal resolution to our level of desire. Unfortunately though, for the current state of in vivo DTI, the temporal resolution is limited to only a few samples for the entire beat cycle due to the low signal to noise ratio.

To address this problem, one could consider the motion of material points in time by taking into account the notion of corresponding material points at different time samples. For an arbitrary point $(x, y, z, t) \in \mathbb{R}^4$ let us assume that we have its corresponding point (x', y', z', t') where $t' > t$. Then, calculating the connection form parameters in this setup can be done in a straight-forward manner by re-writing Equations (8.2), (8.3) exactly as described previously, in the universal coordinate E. However, when calculating connection form parameters, i.e., $\omega_{ij} = \sum_k (d\alpha_{ik})\alpha_{kj}$, we must consider the local derivative in the direction of $\mathbf{f}_4$, i.e., $d\alpha_{ik}$ measures the amount of change of a frame at coordinate (x, y, z, t) with respect to its corresponding neighbor in the 4D coordinate (x', y', z', t').

8.3.1 In vivo cardiac registration

By using the notion of correspondences, we have a model that can parametrize any moving collection of cardiac frames. To obtain these correspondences, one can use a registration algorithm of choice that can provide a mapping between the material points of consecutive time samples. In the context of medical image processing, registration is usually referred to as the "task of finding the spatial relationship between two or more images" [44]. These algorithms generally aim to find a proper transformation that could deform a query image to best fit the template image via the minimization of a cost function.

While there is a body of literature on the topic of medical image registration, for the experiments conducted in this thesis, we use the *elastix* registration algorithm [44, 78] due to its applicability to our problem and ease of use. However, other methods, such as the LDDMM approach of Beg et al. [6], could be used. Such an approach would provide a diffeomorphism.

Figure 8.2 visualizes the result of applying the *elastix* registration method to the Fraction Anisotropy map of two time samples of the in vivo human dataset using its free-to-use and out-of-the-box implementation in the Slicer toolbox [63]. A byproduct of this registration is a mapping between its two input time samples.

The *elastix* method is described to be a multi-functional approach which aims to work for general registration applications for intensity-based images. Klein et al. [44] describe a general registration for *elastix* as follows. Having a fixed intensity image $I_F(x)$ and a moving image $I_M(x)$, the goal is to find a coordinate transformation $T(x)$ such that it minimizes a cost function $C(T|I_F, I_M)$. This requires a suitable cost function C which

A B C

Figure 8.2: An illustration of applying the *elastix* registration algorithm [44] to the Fractional Anisotropy (FA) map of two slices of human in vivo DTI. **A**: a short axis slice of the FA map at 110 ms (moving sample); **B**: a short axis slice of the FA map at 160 ms (fixed sample); **C**: a short axis slice of the output of the *elastix* registration (**A** onto **B**).

properly aligns $I_M(T(x))$ to $I_F(x)$. As mentioned in [44] there are different components to a generic registration problem, namely: the cost function C, the transformation T, the iterative energy minimization, and the sampling and interpolation strategy. *Elastix* is considered to be a general registration pipeline since it can easily adapt various algorithms for its different components. For instance, for the transformation, the 3D rigid affine transform or the nonrigid b-spline transform are two of the available options. Therefore in our experiments, we used *elastix* as a "collection of parametric intensity-based registration methods" [44] which can provide us with the notion of corresponding material points between consecutive time samples.

8.4 Distribution fitting for outlier detection

Our goal is to use connection form measurements for detecting locations where the estimated fiber orientations may be viewed as outliers. To this end, we fit probability density functions (PDFs) to the set of observed values of the forms across voxels. To simplify our calculations, we treat each connection parameter separately. If $\widehat{C}_{ijk} = \{c_{ijk}(p)\}$ is the set of observed connection form measurements for c_{ijk} across positions p, we estimate a PDF $f_{ijk}(c|\theta)$ via fitting to $\widehat{C}_{ijk}$. We considered both non-parametric fitting, via kernel density estimation using Gaussian kernels for human data, and maximum likelihood fitting with a normal distribution for simulated data, based on observations in [65]). This provides 12 independent distributions, with which we can compute the probability density of a given observed connection form value c_{ijk} via $f_{ijk}(c_{ijk}|\theta)$.

To detect outliers, we first estimate the probability distributions described above. Then, for each set of observed connection parameter values $\widehat{C}_p = \{c_{ijk}(p)\}$ at a given voxel position p, we estimate a log-likelihood of the given observed Cartan measurements at that position via $\mathcal{L}_\theta(p) = \sum_{c_{ijk}\in\widehat{C}_p} \log(f_{ijk}(c_{ijk}|\theta))$ where we have assumed independence, in keeping with the previous assumption. We may then label the fiber vector $f_1(p)$ at a given position as an outlier based on the approximate likelihood $\mathcal{L}_\theta(p)$ of its observed connection values.

Once the outliers are labeled, we can perform denoising by removing the noisy fibers and using an inpainting algorithm to re-estimate them. Here, we use an approach that separately fills in the $\mathbf{x}$, y, and z components of the fiber vectors directly, utilizing the global 4D data of each component as a scalar field [95].

9

Experiments and Discussion

First, given the moving frame method, we provide proof of concept Cartan connection parameter estimation results on a Canine data set obtained from the LV mechanics challenge [9]. Then we apply the same method on new in-vivo human DTI data containing time samples of a beating heart. Finally, we demonstrate an application of using the Cartan connection parameters for the detection of irregular local orientation patterns.

9.1 Transmural rotation

In our experiments on both the canine data and the in vivo human data, our frame axes $\mathbf{f}_1, \mathbf{f}_2, \mathbf{f}_3$ are chosen in the manner explained in the previous sections. The results from past fitting of Cartan connection parameters to static ex vivo mammalian heart data in [65] have shown $c_{123}, c_{131}, c_{232}$ to be the most significant parameters, with the others being close to zero. The first of these has to do with the helix angle change in a transmural direction and the latter two are related to sectional curvatures of the heart wall.

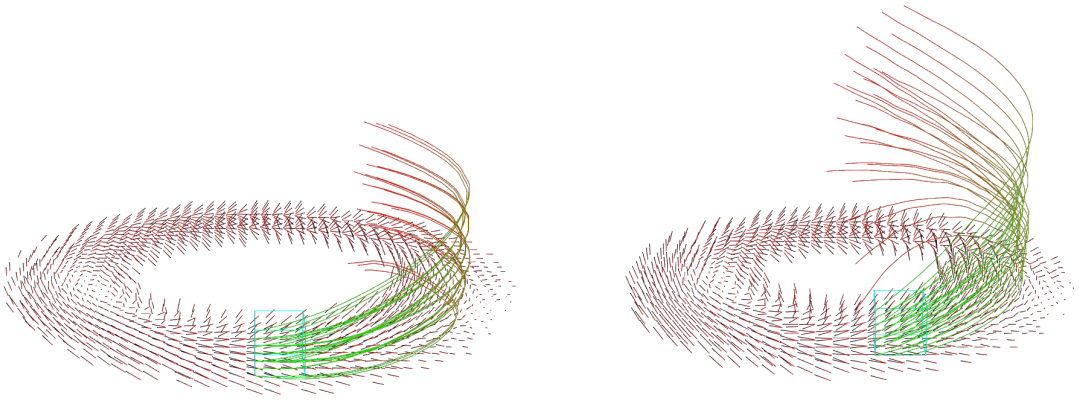

Figure 9.1: An illustration of the simulated motion of canine heart wall fibers in the left ventricle at two time points in the systolic phase: 50 ms (**A**) and 350 ms (**B**). The fiber orientations are shown in red and partial tractography provides a visualization of fibers in a local neighborhood. In this simulation the total transmural increase in applied rotation (θ) from 0 ms to 400 ms is 20 degrees.

The addition of the temporal dimension in our method now adds the possibility to look at frame axis rotation in time, i.e., c_{ij4} connection parameters. In the canine data with a simulated controlled increase in the total epicardium to endocardium rotation (the θ parameter in Section 8.2) we expect the new parameter c_{124} to pick up this effect. Figure 9.1 shows two time frames of a canine data set, where the total angular change in orientation θ is 20 degrees. This choice of enforced rotation was motivated in part by prior biological work, which suggests a small but measurable increase in the rate of transmural fiber angle change as systole progresses [17, 13]. The tractography in the visualization shows how the total epicardium to endocardium turn increases in time.

In Figure 9.2, we show histograms over the entire left ventricle of the connection form parameter fits to the canine data set in Figure 9.1. The units of c_{ijk} are radians/voxel when $k \neq 4$, and radians/10 ms when $k = 4$. In our simulations the active contraction begins

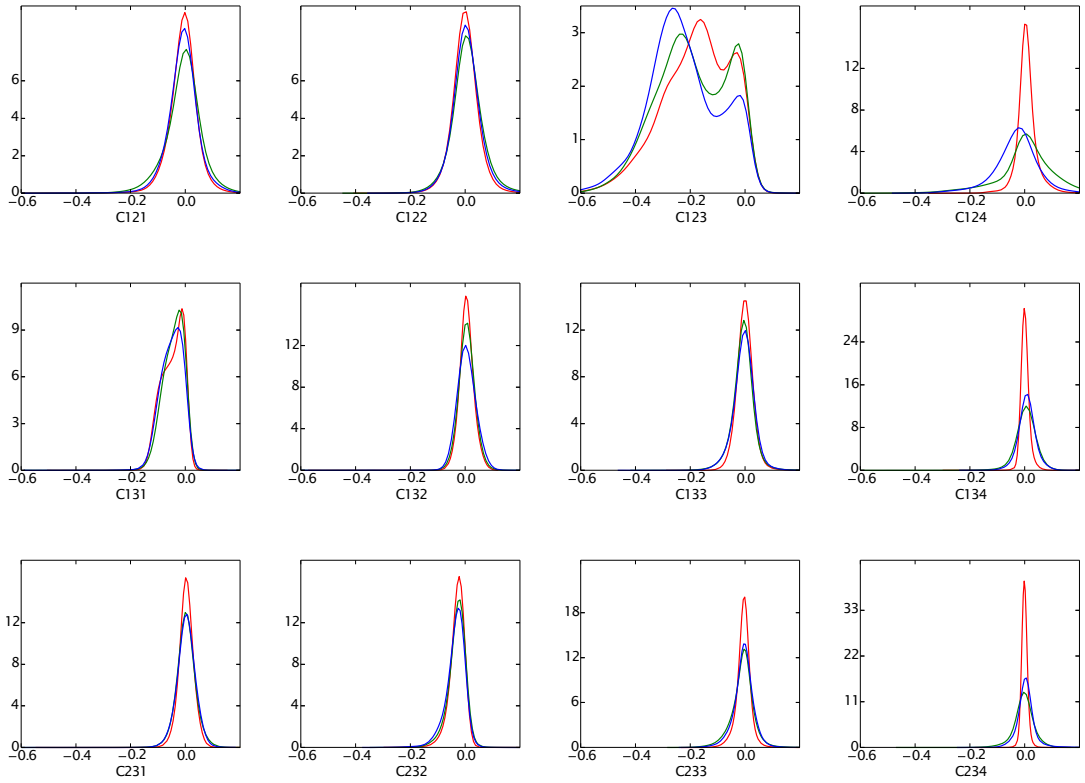

Figure 9.2: The 12 Cartan connection parameters obtained via fits to the canine data set, illustrated in Figure 9.1. The red, green and blue curves show histograms corresponding to the 50 ms, 200 ms and 350 ms time samples in the systolic phase from 0 ms to 400 ms.

at around 100ms, so the red curve for the c_{ij4} terms in the right column of the figure is in fact expected to be very small since it corresponds to 50ms, at which time the fibers are relatively static. We observe that the c_{123} and c_{124} fits show the expected increase in the magnitude of these parameters as time progresses, with the peaks of the histograms shifting towards the left (red $\rightarrow$ blue). The other c_{ijk} terms remain close to zero with the exception of the c_{121} and c_{232} terms since they reflect sectional curvatures of the heart wall, consistent with results on fitting orientation data from static ex vivo hearts [65].

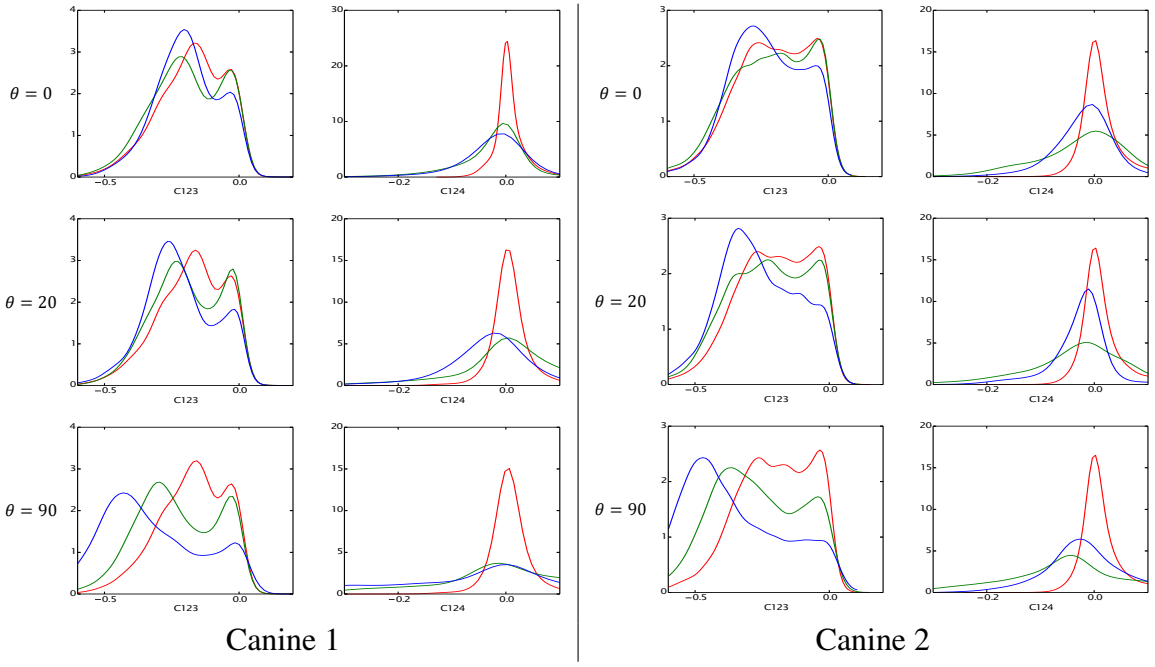

Figure 9.3: We focus on c_{123} and c_{124} and show the effect of different choices for the total applied additional transmural rotation (θ): 0 degrees (**top**), 20 degrees (**middle**) and 90 degrees (**bottom**) for the same canine data set as in Figure 9.2 (**left**) and for a second canine data set (**right**). The red, green and blue curves show histograms corresponding to the 50 ms, 200 ms and 350 ms time samples in the systolic phase from 0 ms to 400 ms

In Figure 9.3, we show additional histograms focusing now on the connection parameters with the highest magnitudes: c_{123} and c_{124}, but adding also a second canine data set. We also consider the effect of no additional rotation θ (top row) and the extreme case of $\theta = 90$ (bottom row). Although the latter case is not biologically realistic, this type of variation in controlled rotation of fibers gives us a way to evaluate our method. For both canine datasets we see the clear shift to the left in the c_{123} histograms (red $\rightarrow$ blue) as θ is increased, reflecting our expectation. The variation in the c_{124} parameters in time is more subtle, because this reflects the instantaneous (time sample to time sample) in plane

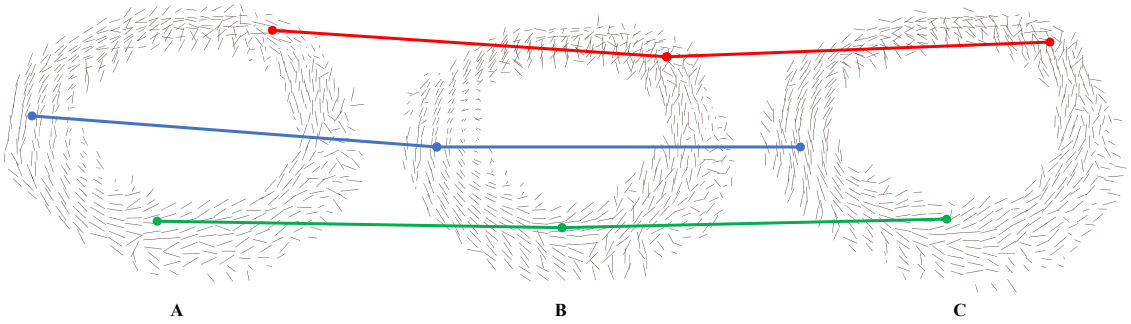

Figure 9.4: An illustration of the motion of human in vivo heart wall fibers at 3 time points in the systolic phase: 110 ms (**A**), 160 ms (**B**), and 210 ms (**C**). The red, green and blue lines show the notion of correspondences between selected material points, at three time samples, obtained by the registration method described in Section 8.3.1.

rotation of the fibers. Comparing the green and blue curves, the results suggest that c_{124} is more uniform in time for the first canine data set, but for the second it is more peaked later in the systolic phase. The consistent increase in c_{123} in time and the expected effect of increasing θ on this connection parameter is evident. The variation of c_{124} in time is more subtle and it appears to be non-linear.

Figure 9.4 illustrates a sample slices of our in vivo data on different time samples. In vivo diffusion imaging presently suffers from many challenges, including low spatial resolution, a limit on the range of possible timing and low signal-to-noise compared to ex vivo acquisitions. The data can also contain artifacts which are spatially varying, e.g., results near the apex are typically not reliable. As described in Section 8.2 we have applied an acquisition sequence that is designed for full heart imaging. As such, our time frames are quite close to each other in the beat cycle and are concentrated at end systole, when the heart wall is thick and fibers are relatively stationary, facilitating diffusion imaging.

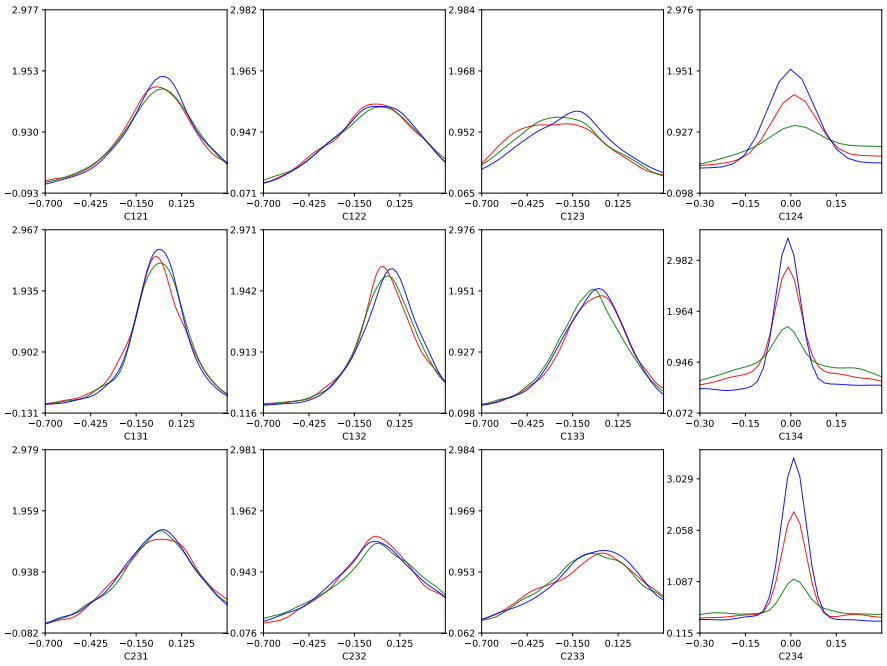

Figure 9.5: The 12 Cartan connection parameters obtained via fits to the in vivo human data set using the sheet-based coordinate system described in Section 8.2.2. The red, green and blue curves show histograms corresponding to the 110 ms, 160 ms and 220 ms time samples. See text for a discussion.

Despite these limitations, as demonstrated in the histogram plot of the in vivo cardiac connection forms in Figure 9.5, we observe the role of the non-zero c_{123} term, capturing transmural rotation, similar to the results for ex vivo static mammalian hearts reported in [65]. Moreover, for different time samples, we observe that the magnitude of transmural angle is shifting slightly to the right (becoming smaller) as time passes. Besides c_{123}, the histograms of the other spatial c_{ijk} terms overlap for the most part, indicating only small rotations in the non-transmural directions. For the temporal connection form histograms

c_{124}, c_{134}, and c_{234}, the magnitude of the terms are small and peaked at zero. Amongst them, c_{124} which measures the change in transmural rotation of fibers in time, has the flattest distribution corresponding to more non-zero values. This resonates with the earlier assumptions of the literature about the change of the fiber angle during the contraction phase [45, 82].

9.2 Detection of orientation outliers

Given a series of moving heart fiber volumes in time (the canine heart data discussed in Section 8.2.1), in Section 9.2.1 we add synthetic noise to the fiber field $\mathbf{f}_1$, and then estimate the connection form parameters at each voxel. The methodology described in Section 8.4 is then used to label statistical outliers as noise. We add two different types of synthetic noise, as described in Section 9.2.1. The fact that in both cases the noise is artificial in nature, allows us to empirically measure the detection performance, and compare it with two alternative approaches. Later, in Section 9.2.2, we apply the same algorithm to the in vivo human dataset, to perform a type of regularization.

9.2.1 Outlier detection with canine simulation data

The simulated canine data itself is considered to be the ground-truth, to which we add noise by perturbing orientations, to evaluate our outlier detection.

Artificial vector noise addition

To test the capabilities of our detection algorithm, we added synthetic noise to the fiber fields of our simulated canine datasets, via two different approaches. Each approach is applied separately to the heart time slices. The first method utilized the von Mises-Fisher

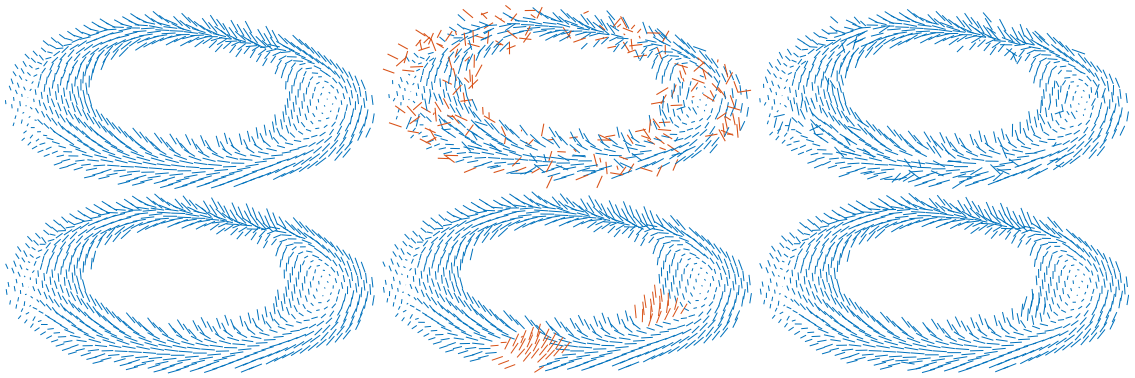

Figure 9.6: Visualization of outlier detection method on Canine data. **Top row**: heart slice with VMF-based noise. **Bottom row**: heart slice with random block rotation noise. **Left column**: ground truth. **Middle column**: outliers detected by our algorithm in red. **Right column**: slice with outliers detected, removed and inpainted.

(VMF) distribution, which describes a probability density function (PDF) on S^2 in $\mathbb{R}^3$, sampled via the Ulrich-Wood rejection sampling approach. There are two parameters: κ, which inversely controls the noise level per position, and ρ, the probability that a given voxel will have noise added to it. Given κ and ρ, for each position p, with probability ρ, we replace $\mathbf{f}_1(p)$ with a unit vector $\mathbf{v}$ from the VMF distribution with density $f(v|\kappa, \mu)$, where $\kappa \geqslant 0$ is the concentration parameter and the mean direction is $\mu = \mathbf{f}_1(p)$.

The second type of noise simultaneously alters blocks of data in the fiber field, via a random rotation matrix. Given a fixed number of noise blocks n_B, for each block B, we generate a random rotation matrix $R_B(\theta, a) \in SO(3)$, which rotates a given vector by an angle θ about an axis a. This is done by sampling θ uniformly from the fixed interval $[\theta_{\text{min}}, \theta_{\text{max}}]$ and choosing a as a uniformly random vector from S^2. We then replace every fiber vector $\mathbf{f}_1(p)$ with its rotated counterpart $R_B(\theta, a)\mathbf{f}_1(p)$, for every $p \in B$.

Alternate approaches for comparison

We compare our detection algorithm to two alternative approaches: a rule-based approach and a local deviation detector. As in the likelihood approach, each method assigns a scalar value per voxel, which can be used to rank and thus label the associated fiber vector as noise.

The first measures variation from the fiber vector field generated by the rule-based approach, using the methods for the left ventricular wall described in [5]. The α_{endo} and α_{epi} were optimized via grid search, to fit the simulated data at $t = 0$ (with total average undirected angular error $\sim 18^\circ$). In this case, a position p is assigned $\Theta_{\text{rule}}(p) = \delta_{\text{err}}(\mathbf{f}_1(p), \mathbf{f}_{1,\text{rule}}(p))$, where $\delta_{\text{err}}(u, v)$ is the undirected angular error between $\mathbf{u}$ and $\mathbf{v}$.

The second is a local method which labels a sudden deviation of the orientation of a fiber vector from that of its neighbours as noise. Per voxel position p, we consider its spatial neighbourhood $N(p)$ and assign to p the average local error $\bar{\Theta}(p) = |N(p)|^{-1} \sum_{q \in N(p)} \delta_{\text{err}}(\mathbf{f}_1(p), \mathbf{f}_1(q))$.

Noise detection results

We demonstrate that our statistical connection form likelihood approach performs better than the rule-based or local detector algorithms (see Table 9.1). In particular, the method is more accurate on the block based noise, which may be interpreted as a form of local structure detection. The neighborhood approach has difficulty with this case, because the rotational noise is consistent throughout the block. For the VMF noise, the local approach slightly outperforms the statistical approach when the concentration parameter κ is small, but the statistical approach is better at high concentrations (small deviations). In general,

Table 9.1: Performance comparison of detection algorithms across noise types. For VMF noise, $\rho = 0.35$. For block noise, $n_B = 10$ with blocksize of $5 \times 5 \times 5$, and we fix $\theta_{\text{max}} - \theta_{\text{min}} = \pi/4$ and define $\bar{\theta} = (\theta_{\text{max}} - \theta_{\text{min}})/2$. Values shown are detection accuracies as percentages. There are $\sim 10^6$ fiber vectors (i.e. unmasked voxels). For the block noise, we choose a detection threshold such that $\sim 5\%$ of the voxels are chosen; for the VMF noise, the proportion ρ is chosen.

	VMF Noise Detection				Block Noise Detection			
Method	$\kappa = 10^2$	$\kappa = 10$	$\kappa = 1$	$\kappa = 0.1$	$\bar{\theta} = \frac{\pi}{8}$	$\bar{\theta} = \frac{3\pi}{8}$	$\bar{\theta} = \frac{5\pi}{8}$	$\bar{\theta} = \frac{7\pi}{8}$
Cartan	**39.94**	**56.24**	65.32	70.17	**38.88**	**69.45**	**74.80**	**68.44**
Rule	35.10	36.80	50.67	69.43	8.70	46.66	63.84	45.43
Local	38.10	52.05	**66.79**	**76.12**	19.40	46.87	54.69	55.19

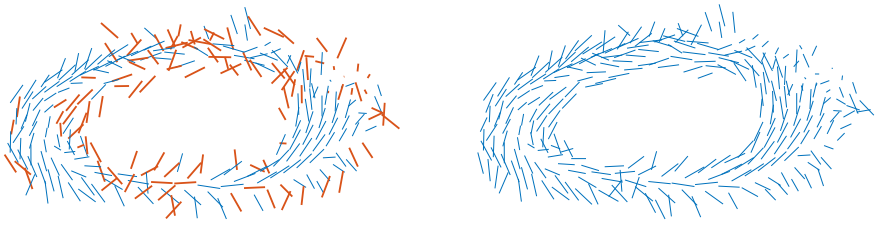

Figure 9.7: Visualization of outlier detection method on in vivo human data. **Left**: heart slice with outliers labeled as noise by our algorithm coloured in red. **Right**: slice with outliers detected, removed and inpainted.

the rule-based approach performs better when the noise is more severe; it has the advantage of not relying on the measured orientations, but this also means it is unable to utilize local information. Qualitatively, one can see the results of outlier detection with our algorithm in Figure 9.6.

9.2.2 Outlier detection with human in vivo data

Our methodology is motivated in part by the significant noise level observed in human in vivo DTI, which we hope to reduce by our outlier detection methodology. Since ground-

truth orientations are not known our results are qualitative in the sense that we hope to correct the most significant errors in the measurements, to obtain a more biophysically plausible reconstruction. In Figure 9.7, we show a slice of the fiber vector field, with the noise detected by our statistical algorithm (left), as well as the denoised version (right), which shows an increase in smoothness and consistency.

9.3 Discussion

The heart is a dynamic organ and little is known about the manner in which fibers rotate or move during the beat cycle. Yet, this knowledge is key to heart function and to understanding the distribution of fiber stress in relation to heart wall mechanics. As in vivo diffusion imaging advances and is used together with other imaging modalities, the tools proposed in this part could offer informative spatio-temporal geometric descriptors for analysis.

We have developed a moving frame method for the modeling of fibers in a dynamic, beating heart. The construction of the Cartan matrix for spatio-temporally varying fiber orientations, along with a method for fitting the Cartan connection parameters, shows promise when applied to simulated canine data with controlled rotations to fibers. In our experiments, we see that non-linearities in the variation of the (time) sample to (time) sample transmural rotation, as reflected in the c_{124} parameter, can arise. We speculate that such non-linearities may occur in the beat cycle to accommodate the wringing motion qualitatively seen when viewing the beating left ventricle in echocardiography or cardiac MRI. Our experiments on in vivo human data, though proof-of-concept at the present time, demonstrate the ability to recover curvature type signatures in such settings as well. We anticipate an improvement in in vivo connection form parameter fits if whole heart diffusion imaging is replaced with an acquisition sequence restricted to a smaller number of slices, but better optimized for temporal sampling.

We have also devised an algorithm for outlier detection via statistical analysis of observed Cartan connection form parameter values. Its performance and applicability to de-

noising have been demonstrated in both a synthetic setting, via artificial additive noise in heart beat cycle simulations of canine heart data, and for in vivo human DT measurements over time. The use of 4D connection forms represents a principled method to smooth and denoise moving fiber data in a spatiotemporally consistent manner. Such an approach can complement the algorithms presently in use, particularly for the lower signal-to-noise ratio of in vivo human DTI.

10

Conclusion

The geometry of fibrous structures in biological tissues can play an important role in their function. For instance, from early images of cardiac ventricular walls, scientists have observed elongated bundles of muscle cells that are locally parallel to each other. These myofibers have been reported to be separated by cleavage planes and to be stacked in sheets. Their arrangement in the myocardium plays a key role in cardiac contraction [82] and also in electrical propagation of the conduction wave [101, 55]. In a different setting, bundles of axons in the mammalian brain are organized in tract systems, which in turn connect different regions [39, 93, 86]. Tractography methods have been used to develop atlases of these tract systems in normal populations [93, 99] and also to study local alterations in these patterns. In recent work by Wedeen et al. [99], it has been argued that these bundles often intersect transversally and that they lie on specific sheets. Yet, methods to actually model or recover these sheets from orientation data are scarce.

Motivated by these considerations, this thesis has presented methods to model the geometry of structures in fibrous tissue from orientation data. In Part II, we introduced a method for finding sheets from a single input vector field tangent to the local direction of fibers. We demonstrated promising results for ex vivo cardiac DTI and for the mammalian brain. For the case of cardiac sheets, we showed that our findings are in accordance with the earlier reports in the literature. In particular, we observe a radial orientation for sheets in the mid-wall region and closer to axial orientation for them at the boundaries of the left ventricle. For the case of the HCP atlas, we observed that while some regions support the hypothesis that locally the fibers lie on sheets, others do not. For instance, in the Fornix tract system, our non-holonomicity energy is relatively low, and thus we were able to fit sheets with high confidence. Whereas for tracts with a tube-like structure, such as the inferior longitudinal fasciculus (ILF), our non-holonomicity energy is higher and therefore the fitted sheets are sparser and exhibit lower confidence. Additionally, within a single tract system, we have illustrated that some regions are more likely to have a sheet-like structure. A prominent example of this case is the corpus callosum (CC) where its central region has a more sheet-like structure than its edges.

Whereas modeling methods to capture the geometry of myofibers from diffusion MRI based orientation measurements in a static heart exist [45, 27, 67, 76, 65], few methods are available to capture the geometry of fibers when the heart beats. To this end, in Part III we specialized in developing a model that can locally capture the spatio-temporal motion of myofibers. We provided applications of our model using a simulation framework as well as proof of concept results for human in vivo DTI. Additionally, we showed how this model could be used in related applications to find regions in tissue that are anomalous

with respect to the orientation statistics of their local neighborhoods, which may arise due to limitations in current in vivo DTI reconstruction methods, or simply due to noise in the reconstruction process.

10.1 Software tools

In the course of my doctoral studies, I contributed to the development of several software tools that were used to implement the methods and to demonstrate the results of my research. These tools are presently within the repository of software packages that are in use by my colleagues in the Shape Analysis group at McGill.

1. **Finding sheets in direction fields**: We implemented a parallelizable gradient decent GPU based algorithm for our sheet finding method. We tested our implementation on several different datasets and verified that it converges experimentally. The code for this implementation is written in PyTorch 0.4 (Python 3.6).
2. **Calculating spatio-temporal connections**: We implemented a method to fit spatio-temporal connection forms, which captures the motion of cardiac frames both in space and time. We tested our code on simulated cardiac data and also on in vivo human cardiac data. The code for this implementation is written in Java.
3. **Visualization**: The visualizations of the results presented in this thesis were implemented using several different programming languages and environments, including Matlab, VTK (C++), Python, Java, and OpenGL. In the last two years of my doctoral research, I built a comprehensive visualization toolbox, based on Java and OpenGL for rendering vector fields, streamlines, sheets, and scalar volumes. The majority of the figures in Chapters 6 and 9, that illustrate the results of my meth-

ods, were generated using this visualization tool. I particularly want to thank Ryan Eckbo and Emmanuel Piuze for developing prototypes of the heart connection form software for the static case, which was then extended to reach its present state.

10.2 Limitations and future work

We believe that the methodologies and tools developed in this thesis open many windows to future research. The following are just a few examples.

For the study of the geometry of cardiac myofibers and mammalian brain tract systems, one could use the more advanced MR-based imaging modalities, such as high angular resolution diffusion imaging (HARDI), to better account for the local direction of fibers. The problem here is that these methods can compute multiple principal directions for fibers within a voxel. This could reflect the branching of myocytes between cleavage planes for the case of the heart [45] or the crossing of fiber tracts for the case of the brain [39]. In their current state, both our sheet finding and moving frame approaches are limited to work only for a single fiber direction per voxel. A solution to this problem is to use more advanced tractography techniques that are suitable for higher-order dMRI to extract different streamlines from the data (both probabilistic and deterministic) [39], and then apply our methods on individual tract systems, similar to what we did in Chapter 6, Section 6.2.

As described in Chapter 3, Sections 3.3.4, and 3.6, the spatial resolution of diffusion imaging is much lower than than the actual cellular dimension of cardiac myocytes or white matter axons. Moving beyond diffusion imaging, other modalities may benefit from our approach. For instance, Clarity imaging [88], which is an instance of a family of tis-

sue clearing methods, provides micro-level information about the tissue by combining staining for specific cell sub-structures such as WGA for membranes, α-actinin for sarcomeres, and Dapi for nuclei [96]. This method presents a unique way to look at tissue structure at the nanometer scale (compared to the millimeter or sub-millimeter scale of dMRI). One could extract the orientation of fibers using computer vision approaches and then use our non-holonomicity energy minimization method to fit sheets in these images. Then, the moving frame method could be applied to the extracted sheet-based coordinates to calculate connection forms which could provide geometrical and statistical information about sheets and fibers at a whole new scale.

Similarly, to address the low temporal resolution of the current state of cardiac DTI, we could consider utilizing the information from other imaging modalities. For example, with ultrasound, we may be able to take advantage of increased temporal resolution, as well as latent fiber information, by utilizing information extracted from the modeling of ex vivo hearts.

While our spatio-temporal connection approach is a natural extension of the methods of moving frames in space to space and time, there are a number of theoretical and practical considerations that can be further addressed. In comparison to other models, such as using regression or spline fits between time points, the use of Cartan forms provides an easily interpretable and intuitive set of measurements able to characterize the evolution of the frame fields over time. While it may be possible to obtain equivalent measurements with other models, we anticipate that this would compromise the elegance, extensibility, and simplicity of the approach we have taken.

10.2 Limitations and future work

Presently our moving frame approach uses only first-order Taylor expansion to calculate connection form values. Direct higher-order expansions can give a better estimate of these values. There are also other indirect approaches based on energy minimization, such as Nelder-Mead optimization [56], that are currently implemented for the static case [65]. Applying them to the spatio-temporal case is straightforward extension which could further improve the accuracy of the computed connection form values.

Furthermore, our connection form values are only based on 1-forms which are able to describe the rotation of fibers in the direction of frame bases. One could consider using higher-order forms to provide further statistics about the geometry of fibers.

As cardiac in vivo diffusion imaging advances, Cartan frame spatio-temporal fitting could offer informative geometric descriptors for analysis. As in the strictly spatial case, a number of natural applications of this formalism are apparent. Previous methods for atlas construction to allow inter-species comparison using differential geometric measures [64], is an example that can readily be extended to the spatiotemporal domain based on the approach described herein. The statistical properties of connection form values can also be adapted for use in learning-based approaches (e.g. for segmentation or other medical imaging tasks). More importantly, these statistics provide means for the analysis of fiber orientation as the heart beats, which will become increasingly important as in vivo diffusion imaging becomes more common. Our outlier detection method, which is based on a coarse global summary of the histogram of spatio-temporal connection forms, could be of significance in clinical applications to assist in providing signals of abnormal geometry, such as those which might occur in the presence of local cardiac infarcts.

10.2 Limitations and future work

A by-product of our sheet fitting algorithms is a sheet-based coordinate system. From this, one could compute connection forms on the fitted frames to the brain fibers for an individual tract system. The calculated connection form parameters could then be used for statistical analysis of brain tracts. The temporal evolution of these tracts due to aging or in the course of a neurodegenerative disease could be studied by applying our spatio-temporal method to multiple scans of the same subject in the course of time.

Finally, our methods for recovering spatio-temporal signatures for moving oriented structures, and for recovering sheet-like geometries for such measurements, are not limited to the case of orientation measurements from biological structures. These methods could be used to study sheet-like organization in the motion of arbitrary vector fields, such as the motion of streamlines recovered from computer vision methods, or directional fields arising in graphics or scientific visualizations.

Bibliography

[1] Michael Ankele and Thomas Schultz. A sheet probability index from diffusion tensor imaging. In *Computational Diffusion MRI*, pages 141–154. Springer, 2018.

[2] Haz-Edine Assemlal, David Tschumperlé, Luc Brun, and Kaleem Siddiqi. Recent advances in diffusion mri modeling: Angular and radial reconstruction. *Medical image analysis*, 15(4):369–396, 2011.

[3] LJ Bao, YM Zhu, WY Liu, P Croisille, ZB Pu, M Robini, and IE Magnin. Denoising human cardiac diffusion tensor magnetic resonance images using sparse representation combined with segmentation. *Physics in Medicine & Biology*, 54 (6):1435, 2009.

[4] Peter J Basser, Sinisa Pajevic, Carlo Pierpaoli, Jeffrey Duda, and Akram Aldroubi. In vivo fiber tractography using dt-mri data. *Magnetic resonance in medicine*, 44 (4):625–632, 2000.

[5] JD Bayer, RC Blake, G Plank, and NA Trayanova. A novel rule-based algorithm for assigning myocardial fiber orientation to computational heart models. *Annals of biomedical engineering*, 40(10):2243–2254, 2012.

[6] M Faisal Beg, Michael I Miller, Alain Trouvé, and Laurent Younes. Computing large deformation metric mappings via geodesic flows of diffeomorphisms. *International journal of computer vision*, 61(2):139–157, 2005.

[7] Mirza Faisal Beg, Patrick A Helm, Elliot McVeigh, Michael I Miller, and Raimond L Winslow. Computational cardiac anatomy using mri. *Magnetic Resonance in Medicine: An Official Journal of the International Society for Magnetic Resonance in Medicine*, 52(5):1167–1174, 2004.

[8] Ohad Ben-Shahar and Steven W Zucker. The perceptual organization of texture flow: A contextual inference approach. *Pattern Analysis and Machine Intelligence, IEEE Transactions on*, 25(4):401–417, 2003.

[9] Oscar Camara, Tommaso Mansi, Mihaela Pop, Kawal Rhode, Maxime Sermesant, and Alistair Young. LV mechanics challenge. In *STACOM*, volume LNCS, 8896. Springer, 2014.

[10] Elie Cartan. Les sous-groupes des groupes continus de transformations. In *Annales scientifiques de l'École Normale Supérieure*, volume 25, pages 57–194, 1908.

[11] Elie Cartan. *La théorie des groupes finis et continus et la géométrie différentielle: traitées par la méthode du repère mobile*. Gauthier-Villars, 1937.

[12] M. Catani, I. Bodi, and Dell'Acqua. Comment on "the geometric structure of the brain fiber pathways". *Science*, 337(6102):1605, 2012.

[13] Junjie Chen, Wei Liu, Huiying Zhang, Liz Lacy, Xiaoxia Yang, Sheng-Kwei Song, Samuel A Wickline, and Xin Yu. Regional ventricular wall thickening reflects changes in cardiac fiber and sheet structure during contraction: quantification with diffusion tensor mri. *Am. J. Physiol. Heart Circ. Physiol.*, 289(5):H1898–H1907, 2005.

[14] Allen Cheng, Frank Langer, Filiberto Rodriguez, John C Criscione, George T Daughters, D Craig Miller, and Neil B Ingels Jr. Transmural sheet strains in the lateral wall of the ovine left ventricle. *American Journal of Physiology-Heart and Circulatory Physiology*, 289(3):H1234–H1241, 2005.

[15] Benjamin JW Chow, George A Wells, Li Chen, Yeung Yam, Paul Galiwango, Arun Abraham, Tej Sheth, Carole Dennie, Rob S Beanlands, and Terrence D Ruddy. Prognostic value of 64-slice cardiac computed tomography: severity of coronary artery disease, coronary atherosclerosis, and left ventricular ejection fraction. *Journal of the American College of Cardiology*, 55(10):1017–1028, 2010.

[16] Manfredo P Do Carmo. *Differential forms and applications*. Springer Science & Business Media, 1994.

[17] Jiangang Dou, Timothy G Reese, Wen-Yih I Tseng, and Van J Wedeen. Cardiac diffusion mri without motion effects. *Magnetic resonance in medicine*, 48(1):105–114, 2002.

[18] Jiangang Dou, Wen-Yih I Tseng, Timothy G Reese, and Van J Wedeen. Combined diffusion and strain mri reveals structure and function of human myocardial laminar sheets in vivo. *Magnetic Resonance in Medicine*, 50(1):107–113, 2003.

[19] Charles Ehresmann. Les connexions infinitésimales dans un espace fibré différentiable. *Séminaire Bourbaki*, 1:153–168, 1948.

[20] Thomas SE Eriksson, AJ Prassl, Gernot Plank, and Gerhard A Holzapfel. Influence of myocardial fiber/sheet orientations on left ventricular mechanical contraction. *Mathematics and Mechanics of Solids*, 18(6):592–606, 2013.

[21] Piero Colli Franzone, Luciano Guerri, and Stefania Tentoni. Mathematical modeling of the excitation process in myocardial tissue: Influence of fiber rotation on wavefront propagation and potential field. *Mathematical biosciences*, 101(2):155–235, 1990.

[22] Martijn Froeling, Aart J. Nederveen, Dennis F.R. Heijtel, Arno Lataster, Clemens Bos, Klaas Nicolay, Mario Maas, Maarten R. Drost, and Gustav J. Strijkers. Diffusion-tensor mri reveals the complex muscle architecture of the human forearm. *Journal of Magnetic Resonance Imaging*, 36(1):237–248, 2012. ISSN 1522-2586. doi: 10.1002/jmri.23608. URL http://dx.doi.org/10.1002/jmri.23608.

[23] Martijn Froeling, Gustav J Strijkers, Aart J Nederveen, Steven A Chamuleau, and Peter R Luijten. Diffusion tensor mri of the heart–in vivo imaging of myocardial fiber architecture. *Current Cardiovascular Imaging Reports*, 7(7):9276, 2014.

[24] Martijn Froeling, Gustav J. Strijkers, Aart J. Nederveen, and Peter R. Luijten. Whole heart DTI using asymmetric bipolar diffusion gradients. *Journal of Cardiovascular Magnetic Resonance*, 17(Suppl 1):15, 2015.

[25] Liesbeth Geerts, Peter Bovendeerd, Klaas Nicolay, and Theo Arts. Characterization of the normal cardiac myofiber field in goat measured with mr-diffusion tensor imaging. *American Journal of Physiology-Heart and Circulatory Physiology*, 283 (1):H139–H145, 2002.

[26] SR Geiger. Gross morphology and fiber geometry of the heart. *Handbook of Physiology, Sect. 2, The Cardiovascular System*, 1979.

[27] Stephen H. Gilbert, Alan P. Benson, Pan Li, and Arun V. Holden. Regional localisation of left ventricular sheet structure: integration with current models of cardiac fibre, sheet and band structure. *Eur. J. Cardio-Thorac. Surg*, 32(2):231–249, 2007.

[28] Stephen H Gilbert, David Benoist, Alan P Benson, Ed White, Steven F Tanner, Arun V Holden, Halina Dobrzynski, Olivier Bernus, and Aleksandra Radjenovic. Visualization and quantification of whole rat heart laminar structure using high-spatial resolution contrast-enhanced mri. *American Journal of Physiology-Heart and Circulatory Physiology*, 302(1):H287–H298, 2011.

[29] RA Greenbaum, S Yen Ho, DG Gibson, AE Becker, and RH Anderson. Left ventricular fibre architecture in man. *Heart*, 45(3):248–263, 1981.

[30] AF Grimm. Myocardial sarcomeres and the functioning mammalian heart, 1976.

[31] JM Guccione and AD McCulloch. Mechanics of active contraction in cardiac muscle: part i - constitutive relations for fiber stress that describe deactivation. *Journal of biomechanical engineering*, 115(1):72–81, 1993.

[32] Myrianthi Hadjicharalambous, Radomir Chabiniok, Liya Asner, Eva Sammut, James Wong, Gerald Carr-White, Jack Lee, Reza Razavi, Nicolas Smith, and David Nordsletten. Analysis of passive cardiac constitutive laws for parameter estimation

using 3d tagged MRI. *Biomechanics and modeling in mechanobiology*, 14(4):807–828, 2015.

[33] Thomas Carolus Johannes Dela Haije. *Finsler Geometry and Diffusion MRI*. PhD thesis, Eindhoven University of Technology, 2017.

[34] Patrick Helm, Mirza Faisal Beg, Michael I Miller, and Raimond L Winslow. Measuring and mapping cardiac fiber and laminar architecture using diffusion tensor mr imaging. *Annals of the New York Academy of Sciences*, 1047(1):296–307, 2005.

[35] Patrick A Helm, Laurent Younes, Mirza F Beg, Daniel B Ennis, Christophe Leclercq, Owen P Faris, Elliot McVeigh, David Kass, Michael I Miller, and Raimond L Winslow. Evidence of structural remodeling in the dyssynchronous failing heart. *Circulation research*, 98(1):125–132, 2006.

[36] Gerhard A Holzapfel and Ray W Ogden. Constitutive modelling of passive myocardium: a structurally based framework for material characterization. *Phil. Trans. R. Soc. A: Mathematical, Physical and Engineering Sciences*, 367(1902):3445–3475, 2009.

[37] A Horowitz, M Perl, and S Sideman. Geodesics as a mechanically optimal fiber geometry for the left ventricle. *Basic research in cardiology*, 88:67–74, 1992.

[38] Neil B Ingels Jr, David E Hansen, GT Daughters 2nd, Edward B Stinson, Edwin L Alderman, and D Craig Miller. Relation between longitudinal, circumferential, and oblique shortening and torsional deformation in the left ventricle of the transplanted human heart. *Circulation research*, 64(5):915–927, 1989.

[39] Ben Jeurissen, Maxime Descoteaux, Susumu Mori, and Alexander Leemans. Diffusion mri fiber tractography of the brain. *NMR in Biomedicine*, 32(4):e3785, 2019.

[40] Derek K Jones. *Diffusion mri*. Oxford University Press, 2010.

[41] P-S Jouk, Yves Usson, Gabrielle Michalowicz, and Laurence Grossi. Three-dimensional cartography of the pattern of the myofibres in the second trimester fetal human heart. *Anatomy and embryology*, 202(2):103–118, 2000.

[42] Hideaki Kanzaki, Satoshi Nakatani, Naoaki Yamada, Shin-ichi Urayama, Kunio Miyatake, and Masafumi Kitakaze. Impaired systolic torsion in dilated cardiomyopathy: Reversal of apical rotation at mid-systole characterized with magnetic resonance tagging method. *Basic Research in Cardiology*, 101(6):465–470, Nov 2006. ISSN 1435-1803. doi: 10.1007/s00395-006-0603-6. URL https://doi.org/10.1007/s00395-006-0603-6.

[43] Gordon Kindlmann, Xavier Tricoche, and Carl-Fredrik Westin. Delineating white matter structure in diffusion tensor mri with anisotropy creases. *Medical image analysis*, 11(5):492–502, 2007.

[44] Stefan Klein, Marius Staring, Keelin Murphy, Max A Viergever, Josien PW Pluim, et al. Elastix: a toolbox for intensity-based medical image registration. *IEEE transactions on medical imaging*, 29(1):196, 2010.

[45] Ian J LeGrice, BH Smaill, LZ Chai, SG Edgar, JB Gavin, and Peter J Hunter. Laminar structure of the heart: ventricular myocyte arrangement and connective tissue architecture in the dog. *American Journal of Physiology-Heart and Circulatory Physiology*, 269(2):H571–H582, 1995.

[46] Karim Lekadir, Matthias Lange, Veronika A Zimmer, Corné Hoogendoorn, and Alejandro F Frangi. Statistically-driven 3d fiber reconstruction and denoising from multi-slice cardiac dti using a markov random field model. *Medical image analysis*, 27:105–116, 2016.

[47] Joao AC Lima, Richmond Jeremy, William Guier, Sophie Bouton, Elias A Zerhouni, Elliot McVeigh, Maurice B Buchalter, Myron L Weisfeldt, Edward P Shapiro, and James L Weiss. Accurate systolic wall thickening by nuclear magnetic resonance imaging with tissue tagging: correlation with sonomicrometers in

normal and ischemic myocardium. *Journal of the American College of Cardiology*, 21(7):1741–1751, 1993.

[48] AJ Linzbach. Heart failure from the point of view of quantitative anatomy. *The American journal of cardiology*, 5(3):370–382, 1960.

[49] Herve Lombaert, Jean-Marc Peyrat, Pierre Croisille, Stanislas Rapacchi, Laurent Fanton, Farida Cheriet, Patrick Clarysse, Isabelle Magnin, Hervé Delingette, and Nicholas Ayache. Human atlas of the cardiac fiber architecture: study on a healthy population. *IEEE Transactions on Medical Imaging*, 31(7):1436–1447, 2012.

[50] Pradeep K Luther. The vertebrate muscle z-disc: sarcomere anchor for structure and signalling. *Journal of muscle research and cell motility*, 30(5-6):171–185, 2009.

[51] Steve A Maas, Benjamin J Ellis, Gerard A Ateshian, and Jeffrey A Weiss. Febio: finite elements for biomechanics. *Journal of biomechanical engineering*, 134(1): 011005, 2012.

[52] Klaus H Maier-Hein, Peter F Neher, Jean-Christophe Houde, Marc-Alexandre Côté, Eleftherios Garyfallidis, Jidan Zhong, Maxime Chamberland, Fang-Cheng Yeh, et al. The challenge of mapping the human connectome based on diffusion tractography. *Nature communications*, 8(1):1349, 2017.

[53] Franklin P Mall. On the muscular architecture of the ventricles of the human heart. *American Journal of Anatomy*, 11(3):211–266, 1911.

[54] Michael E Moseley, Yoram Cohen, J Kucharczyk, J Mintorovitch, HS Asgari, MF Wendland, J Tsuruda, and D Norman. Diffusion-weighted mr imaging of anisotropic water diffusion in cat central nervous system. *Radiology*, 176(2):439–445, 1990.

[55] Martyn P Nash and Peter J Hunter. Computational mechanics of the heart. *Journal of Elasticity and the Physical Science of Solids*, 61(1-3):113–141, 2000.

[56] John A Nelder and Roger Mead. A simplex method for function minimization. *The computer journal*, 7(4):308–313, 1965.

[57] Sonia Nielles-Vallespin, Zohya Khalique, Pedro F Ferreira, Ranil de Silva, Andrew D Scott, Philip Kilner, Laura-Ann McGill, Archontis Giannakidis, Peter D Gatehouse, Daniel Ennis, et al. Assessment of myocardial microstructural dynamics by in vivo diffusion tensor cardiac magnetic resonance. *Journal of the American College of Cardiology*, 69(6):661–676, 2017.

[58] PM Nielsen, IJ Le Grice, BH Smaill, and PJ Hunter. Mathematical model of geometry and fibrous structure of the heart. *American Journal of Physiology-Heart and Circulatory Physiology*, 260(4):H1365–H1378, 1991.

[59] Iwao Ohtsuki. Localization of troponin in thin filament and tropomyosin paracrystal. *The Journal of Biochemistry*, 75(4):753–765, 1974.

[60] Barrett O'Neill. *Elementary differential geometry*. Academic press, 2006.

[61] Adam Paszke, Sam Gross, Soumith Chintala, Gregory Chanan, Edward Yang, Zachary DeVito, Zeming Lin, Alban Desmaison, Luca Antiga, and Adam Lerer. Automatic differentiation in pytorch. 2017.

[62] J. M. Peyrat, M. Sermesant, X. Pennec, H. Delingette, C. Xu, E. R. McVeigh, and N. Ayache. A computational framework for the statistical analysis of cardiac diffusion tensors: Application to a small database of canine hearts. *IEEE Transactions on Medical Imaging*, 26(11):1500–1514, Nov 2007. ISSN 0278-0062. doi: 10.1109/TMI.2007.907286.

[63] Steve Pieper, Michael Halle, and Ron Kikinis. 3d slicer. In *2004 2nd IEEE international symposium on biomedical imaging: nano to macro (IEEE Cat No. 04EX821)*, pages 632–635. IEEE, 2004.

[64] Emmanuel Piuze, Herve Lombaert, Jon Sporring, Gustav J Strijkers, Adrianus J Bakermans, and Kaleem Siddiqi. Atlases of cardiac fiber differential geometry. In

International Conference on Functional Imaging and Modeling of the Heart, pages 442–449. Springer, 2013.

[65] Emmanuel Piuze, Jon Sporring, and Kaleem Siddiqi. Maurer-cartan forms for fields on surfaces: application to heart fiber geometry. *IEEE transactions on pattern analysis and machine intelligence*, 37(12):2492–2504, 2015.

[66] Emmanuel Piuze, Jon Sporring, and Kaleem Siddiqi. Moving frames for heart fiber reconstruction. In *International Conference on Information Processing in Medical Imaging*, pages 527–539. Springer, 2015.

[67] Damien Rohmer, Arkadiusz Sitek, and Grant T Gullberg. Reconstruction and visualization of fiber and laminar structure in the normal human heart from ex vivo diffusion tensor magnetic resonance imaging (dtmri) data. *Investigative radiology*, 42(11):777–789, 2007.

[68] Robert F Rushmer, Dean K Crystal, and Clyde Wagner. The functional anatomy of ventricular contraction. *Circulation research*, 1(2):162–170, 1953.

[69] Babak Samari, Tristan Aumentado-Armstrong, Gustav Strijkers, Martijn Froeling, and Kaleem Siddiqi. Cartan frames for heart wall fiber motion. In *International Conference on Functional Imaging and Modeling of the Heart*, pages 32–41. Springer, 2017.

[70] Babak Samari, Tristan Aumentado-Armstrong, Gustav Strijkers, Martijn Froeling, and Kaleem Siddiqi. Denoising moving heart wall fibers using cartan frames. In *International Conference on Medical Image Computing and Computer-Assisted Intervention*, pages 672–680. Springer, 2017.

[71] Babak Samari, Tabish A Syed, and Kaleem Siddiqi. Minimizing non-holonomicity: Finding sheets in fibrous structures. In *International Conference on Information Processing in Medical Imaging*, pages 183–194. Springer, 2019.

[72] Joern JW Sandstede, Thorsten Johnson, Kerstin Harre, Meinrad Beer, Siegfried Hofmann, Thomas Pabst, Werner Kenn, Wolfram Voelker, Stefan Neubauer, and

Dietbert Hahn. Cardiac systolic rotation and contraction before and after valve replacement for aortic stenosis: a myocardial tagging study using mr imaging. *American Journal of Roentgenology*, 178(4):953–958, 2002.

[73] Peter Savadjiev, Steven W Zucker, and Kaleem Siddiqi. On the differential geometry of 3d flow patterns: Generalized helicoids and diffusion mri analysis. In *2007 IEEE 11th International Conference on Computer Vision*, pages 1–8. IEEE, 2007.

[74] Peter Savadjiev, Jennifer SW Campbell, G Bruce Pike, and Kaleem Siddiqi. Streamline flows for white matter fibre pathway segmentation in diffusion mri. In *International Conference on Medical Image Computing and Computer-Assisted Intervention*, pages 135–143. Springer, 2008.

[75] Peter Savadjiev, Gustav J Strijkers, Adrianus J Bakermans, Emmanuel Piuze, Steven W Zucker, and Kaleem Siddiqi. Heart wall myofibers are arranged in minimal surfaces to optimize organ function. *Proc. Natl. Acad. Sci. U. S. A.*, 109(24): 9248–9253, 12 June 2012.

[76] Peter Savadjiev, Gustav J Strijkers, Adrianus J Bakermans, Emmanuel Piuze, Steven W Zucker, and Kaleem Siddiqi. Heart wall myofibers are arranged in minimal surfaces to optimize organ function. *Proceedings of the National Academy of Sciences*, 109(24):9248–9253, 2012.

[77] Partho P Sengupta, Josef Korinek, Marek Belohlavek, Jagat Narula, Mani A Vannan, Arshad Jahangir, and Bijoy K Khandheria. Left ventricular structure and function: basic science for cardiac imaging. *Journal of the American College of Cardiology*, 48(10):1988–2001, 2006.

[78] Denis P Shamonin, Esther E Bron, Boudewijn PF Lelieveldt, Marion Smits, Stefan Klein, and Marius Staring. Fast parallel image registration on cpu and gpu for diagnostic classification of alzheimer's disease. *Frontiers in neuroinformatics*, 7: 50, 2014.

[79] Theodore Shifrin. *Multivariable mathematics: linear algebra, multivariable calculus, and manifolds*, volume 10. 2005.

[80] Kaleem Siddiqi, Emmanuel Piuze-Phaneuf, and Jon Sporring. Recovery of missing information in diffusion magnetic resonance imaging data, November 17 2016. US Patent App. 15/154,404.

[81] Kaleem Siddiqi, Emmanuel Piuze-Phaneuf, and Jon Sporring. Methods of modelling and characterising heart fiber geometry, February 14 2017. US Patent 9,569,887.

[82] H M Spotnitz. Macro design, structure, and mechanics of the left ventricle. *J. Thorac. Cardiovasc. Surg.*, 119(5):1053–1077, May 2000.

[83] Christian T. Stoeck, Constantin von Deuster, Martin Genet, David Atkinson, and Sebastien Kozerke. Second order motion compensated spin-echo diffusion tensor imaging of the human heart. *Journal of Cardiovascular Magnetic Resonance*, 17 (Suppl 1):81, 2015.

[84] Daniel D Streeter Jr, Henry M Spotnitz, Dali P Patel, JOHN ROSS Jr, and Edmund H Sonnenblick. Fiber orientation in the canine left ventricle during diastole and systole. *Circulation research*, 24(3):339–347, 1969.

[85] Tabish A Syed, Babak Samari, and Kaleem Siddiqi. Estimating sheets in the heart wall. In *International Workshop on Statistical Atlases and Computational Models of the Heart*, pages 3–11. Springer, 2018.

[86] Chantal MW Tax, Tom Dela Haije, Andrea Fuster, Carl-Fredrik Westin, Max A Viergever, Luc Florack, and Alexander Leemans. Sheet probability index (spi): Characterizing the geometrical organization of the white matter with diffusion mri. *NeuroImage*, 142:260–279, 2016.

[87] Chantal MW Tax, Carl-Fredrik Westin, Tom Dela Haije, Andrea Fuster, Max A Viergever, Evan Calabrese, Luc Florack, and Alexander Leemans. Quantifying the

brain's sheet structure with normalized convolution. *Medical image analysis*, 39: 162–177, 2017.

[88] Raju Tomer, Li Ye, Brian Hsueh, and Karl Deisseroth. Advanced clarity for rapid and high-resolution imaging of intact tissues. *Nature protocols*, 9(7):1682, 2014.

[89] Francisco Torrent-Guasp, Manel Ballester, Gerald D Buckberg, Francesc Carreras, Albert Flotats, Ignasi Carrió, Ana Ferreira, Louis E Samuels, and Jagat Narula. Spatial orientation of the ventricular muscle band: physiologic contribution and surgical implications. *The Journal of Thoracic and Cardiovascular Surgery*, 122 (2):389–392, 2001.

[90] Nicolas Toussaint, Christian T Stoeck, Tobias Schaeffter, Sebastian Kozerke, Maxime Sermesant, and Philip G Batchelor. In vivo human cardiac fibre architecture estimation using shape-based diffusion tensor processing. *Medical image analysis*, 17(8):1243–1255, 2013.

[91] Wen-Yih I Tseng, Van J Wedeen, Timothy G Reese, R Neal Smith, and Elkan F Halpern. Diffusion tensor mri of myocardial fibers and sheets: correspondence with visible cut-face texture. *Journal of Magnetic Resonance Imaging: An Official Journal of the International Society for Magnetic Resonance in Medicine*, 17(1): 31–42, 2003.

[92] David S Tuch, Timothy G Reese, Mette R Wiegell, Nikos Makris, John W Belliveau, and Van J Wedeen. High angular resolution diffusion imaging reveals intravoxel white matter fiber heterogeneity. *Magnetic Resonance in Medicine: An Official Journal of the International Society for Magnetic Resonance in Medicine*, 48(4):577–582, 2002.

[93] David C Van Essen, Stephen M Smith, Deanna M Barch, Timothy EJ Behrens, Essa Yacoub, Kamil Ugurbil, Wu-Minn HCP Consortium, et al. The wu-minn human connectome project: an overview. *Neuroimage*, 80:62–79, 2013.

[94] Anna Vilanova, G Berenschot, and C Van Pul. Dti visualization with streamsurfaces and evenly-spaced volume seeding. In *Proceedings of the Sixth Joint Eurographics-IEEE TCVG conference on Visualization*, pages 173–182. Eurographics Association, 2004.

[95] Guojie Wang, Damien Garcia, Yi Liu, Richard De Jeu, and A Johannes Dolman. A three-dimensional gap filling method for large geophysical datasets: Application to global satellite soil moisture observations. *Environmental Modelling & Software*, 30:139–142, 2012.

[96] Zhiwei Wang, Jie Zhang, Guangpu Fan, Hui Zhao, Xu Wang, Jing Zhang, Peide Zhang, and Wei Wang. Imaging transparent intact cardiac tissue with single-cell resolution. *Biomedical optics express*, 9(2):423–436, 2018.

[97] Karl T Weber. Cardiac interstitium in health and disease: the fibrillar collagen network. *Journal of the American College of Cardiology*, 13(7):1637–1652, 1989.

[98] Van J Wedeen, Douglas L Rosene, Ruopeng Wang, Guangping Dai, Farzad Mortazavi, Patric Hagmann, Jon H Kaas, and Wen-Yih I Tseng. Response to comment on "the geometric structure of the brain fiber pathways". *Science*, 337(6102):1605–1605, 2012.

[99] Van J Wedeen, Douglas L Rosene, Ruopeng Wang, Guangping Dai, et al. The geometric structure of the brain fiber pathways. *Science*, 335(6076):1628–1634, 2012.

[100] Wikipedia contributors. Heart — Wikipedia, the free encyclopedia. https://en.wikipedia.org/w/index.php?title=Heart&oldid=910050612, 2019. [Online; accessed 27-August-2019].

[101] Robert J Young and Alexander V Panfilov. Anisotropy of wave propagation in the heart can be modeled by a riemannian electrophysiological metric. *Proceedings of the National Academy of Sciences*, 107(34):15063–15068, 2010.

[102] Aminov Yu. The geometry of vector fields. *Gordon & Breach Publ*, 2000.

[103] Paul A. Yushkevich, Joseph Piven, Heather Cody Hazlett, Rachel Gimpel Smith, Sean Ho, James C. Gee, and Guido Gerig. User-guided 3d active contour segmentation of anatomical structures: Significantly improved efficiency and reliability. *NeuroImage*, 31(3):1116 – 1128, 2006. ISSN 1053-8119. doi: http://dx.doi.org/10.1016/j.neuroimage.2006.01.015.

[104] Paul A. Yushkevich, Hui Zhang, Tony J. Simon, and James C. Gee. Structure-specific statistical mapping of white matter tracts. *NeuroImage*, 41(2):448 – 461, 2008. ISSN 1053-8119.

A

Detailed Proof of Convergence of Minimizing Non-Holonomicity Energy

This is the detailed proof of convergence of the non-holonomicity energy minimization approach described in Chapter 5, Section 5.2, and published in "Minimizing Non-holonomicity: Finding Sheets in Fibrous Structures"[71] which is the result of collaborative work with Tabish Syed in the Shape Analysis Group at McGill University.

Babak Samari

Lemma 1 *For an orthonormal frame field* $\{\mathbf{u}, \mathbf{v}, \mathbf{n} = \mathbf{u} \times \mathbf{v}\}$ *with fixed field* $\mathbf{u}$*, the perturbed normal* $\hat{\mathbf{n}} = \mathbf{u} \times R^{\mathbf{u}}_{\theta}\mathbf{v}$ *corresponding to perturbation* θ *in* $\mathbf{v}$*, is given by* $\cos\theta\ \mathbf{n} - \sin\theta\ \mathbf{v}$.

Proof 2 *Consider a fixed vector field* $\mathbf{u}$ *and a variable vector field* $\mathbf{v}(t)$ *in* $\mathbb{R}^3$ *in plane perpendicular to* $\mathbf{u}$*, such that* $\langle \mathbf{u}, \mathbf{v} \rangle = 0$*. Notice that given an initial frame field* $\mathbf{v} = \mathbf{v}(0)$*,* $\mathbf{u}$*, it is sufficient to specify a single scalar function* $\theta(x, y, z)$ *to fully describe the perturbed vector field* $\hat{\mathbf{v}}$*. So that, we can write* $\hat{\mathbf{v}}(x, y, z) = \mathbf{R}^{\mathbf{u}}_{\theta}\mathbf{v}(x, y, z)$*. where* $\mathbf{R}^{\mathbf{u}}_{\theta}$ *is a* 3×3 *rotation*

matrix about axis $\mathbf{u}$ *by an angle* θ*. We can decompose* $\mathbf{R}^{\mathbf{u}}_{\theta}$ *by Rodriguez rotation formula as follows:*

$$R^{\mathbf{u}}_{\theta} = \cos\theta\,\mathbf{I} + \sin\theta\,[\mathbf{u}]_{\times} + (1-\cos\theta)(\mathbf{u}\otimes\mathbf{u}). \tag{A.1}$$

where,$\mathbf{I}$ *is the* 3×3 *identity matrix,* $\mathbf{u}\otimes\mathbf{u} = \mathbf{u}\mathbf{u}^T$ *and* $[\mathbf{u}]_{\times}$ *is the cross product matrix expanded below*

$$[\mathbf{u}]_{\times} = \begin{pmatrix} 0 & -u_z & u_y \\ u_z & 0 & -u_x \\ -u_y & u_x & 0 \end{pmatrix}$$

Using Equation (A.1) *we have,*

$$\begin{aligned}
\hat{\mathbf{n}} &= \mathbf{u}\times(\cos\theta\,\mathbf{I} + \sin\theta\,[\mathbf{u}]_{\times} + (1-\cos\theta)(\mathbf{u}\otimes\mathbf{u}))\,\mathbf{v} \\
&= \mathbf{u}\times\big(\cos\theta\,\mathbf{v} + \sin\theta\,(\mathbf{u}\times\mathbf{v}) + (1-\cos\theta)(\mathbf{u}\mathbf{u}^T\mathbf{v})\big)
\end{aligned}$$

since $\mathbf{u}\perp\mathbf{v}$*, therefore,* $\mathbf{u}^T\mathbf{v} = \mathbf{v}^T\mathbf{u} = 0$

$$\begin{aligned}
\hat{\mathbf{n}} &= \mathbf{u}\times(\cos\theta\,\mathbf{v} + \sin\theta\,(\mathbf{u}\times\mathbf{v})) \\
&= \cos\theta(\mathbf{u}\times\mathbf{v}) + \sin\theta(\mathbf{u}\times(\mathbf{u}\times\mathbf{v})) \\
&= \cos\theta(\mathbf{u}\times\mathbf{v}) + \sin\theta(\mathbf{u}\times\mathbf{n}) \quad \textit{where } \mathbf{n} = \mathbf{u}\times\mathbf{v} \\
&= \cos\theta\,\mathbf{n} - \sin\theta\,\mathbf{v}
\end{aligned} \tag{A.2}$$

Lemma 2 *For an orthonormal frame field* $\{\mathbf{u},\mathbf{v},\mathbf{n}=\mathbf{u}\times\mathbf{v}\}$ *with fixed field* $\mathbf{u}$*, derivative* $D[\hat{\mathbf{v}}]$ *of perturbed vector field* $\hat{\mathbf{v}}$ *corresponding to scalar perturbation field* θ *is given by*

$\cos\theta\ J_{\mathbf{v}} + \sin\theta\ J_{\mathbf{n}} - \sin\theta\ \mathbf{v}(\nabla\theta)^T + \cos\theta\ \mathbf{n}(\nabla\theta)^T$,

Proof 3

$$D[\hat{\mathbf{v}}] = J_{\hat{\mathbf{v}}} = J_{R^{\mathbf{u}}_{\theta}\mathbf{v}}$$

using Lemma 1 we have

$$\begin{aligned}
[J_{\hat{\mathbf{v}}}]_{ij} &= \left[\frac{\partial}{\partial x^j}\cos\theta\ v_i\right] + \left[\frac{\partial}{\partial x^j}\sin\theta\ n_i\right] \\
&= \left[\cos\theta\frac{\partial v_i}{\partial x^j} + v_i\frac{\partial\cos\theta}{\partial x^j}\right] + \left[sin\theta\frac{\partial n_i}{\partial x^j} + n_i\frac{\partial\sin\theta}{\partial x^j}\right] \\
&= \cos\theta\ [J_{\mathbf{v}}]_{ij} + \sin\theta\ [J_{\mathbf{n}}]_{ij} - \sin\theta\ \left[v_i\frac{\partial\theta}{\partial x^j}\right] + \cos\theta\ \left[n_i\frac{\partial\theta}{\partial x^j}\right] \\
\implies J_{\hat{\mathbf{v}}} &= \cos\theta\ J_{\mathbf{v}} + \sin\theta\ J_{\mathbf{n}} - \sin\theta\ \mathbf{v}(\nabla\theta)^T + \cos\theta\ \mathbf{n}(\nabla\theta)^T
\end{aligned}$$

Lemma 3 *The Lie Bracket* $[\mathbf{u}, \hat{\mathbf{v}}]$ *of perturbed vector field* $\hat{\mathbf{v}}$ *is given by* $\cos\theta\ [\mathbf{u}, \mathbf{v}] + \sin\theta\ [\mathbf{u}, \mathbf{n}] + \nabla_{\mathbf{u}}\theta\ (\cos\theta\ \mathbf{n} - \sin\theta\ \mathbf{v})$

Proof 4

$$
\begin{aligned}
[\mathbf{u}, \hat{\mathbf{v}}] &= J_{\hat{\mathbf{v}}}\mathbf{u} - J_{\mathbf{u}}\hat{\mathbf{v}} \\
&= \cos\theta\, J_{\mathbf{v}}\mathbf{u} + \sin\theta\, J_{\mathbf{n}}\mathbf{u} \\
&- \sin\theta\, \mathbf{v}(\nabla\theta)^T\mathbf{u} + \cos\theta\, \mathbf{n}(\nabla\theta)^T\mathbf{u} - J_{\mathbf{u}}\left(\cos\theta\, \mathbf{I} + \sin\theta\, [\mathbf{u}]_\times + (1-\cos\theta)(\mathbf{u}\otimes\mathbf{u})\right)\mathbf{v} \\
&= \cos\theta\, J_{\mathbf{v}}\mathbf{u} + \sin\theta\, J_{\mathbf{n}}\mathbf{u} + (\nabla_{\mathbf{u}}\theta\cos\theta)\,\mathbf{n} - (\nabla_{\mathbf{u}}\theta\sin\theta)\,\mathbf{v} - J_{\mathbf{u}}\left(\cos\theta\,\mathbf{v} + \sin\theta\,(\mathbf{u}\times\mathbf{v})\right) \\
&= (\cos\theta)J_{\mathbf{v}}\mathbf{u} + (\sin\theta)J_{\mathbf{n}}\mathbf{u} + (\nabla_{\mathbf{u}}\theta\cos\theta)\mathbf{n} - (\nabla_{\mathbf{u}}\theta\sin\theta)\mathbf{v} - (\cos\theta)J_{\mathbf{u}}\mathbf{v} - (\sin\theta)J_{\mathbf{u}}\mathbf{n} \\
&= \cos\theta\,[\mathbf{u}, \mathbf{v}] + \sin\theta\,[\mathbf{u}, \mathbf{n}] + \nabla_{\mathbf{u}}\theta\,(\cos\theta\,\mathbf{n} - \sin\theta\,\mathbf{v})
\end{aligned}
$$

Lemma 4 *(non-holonomicity of perturbed field) The non-holonomicity $\rho(\theta)$ of perturbed frame field is given by $\rho_s(\theta) + \nabla_{\mathbf{u}}\theta$.*

Proof 5 *Using Equation (A.2) we get,*

$$
\begin{aligned}
\rho(\theta) &= \langle \mathbf{u}\times\hat{\mathbf{v}}, [\mathbf{u}, \hat{\mathbf{v}}]\rangle = \langle \cos\theta\,\mathbf{n} - \sin\theta\,\mathbf{v}\ ,\ [\mathbf{u}, \hat{\mathbf{v}}]\rangle \\
&= \cos\theta\left\langle \mathbf{n}\ ,\ [\mathbf{u}, \hat{\mathbf{v}}]\right\rangle - \sin\theta\left\langle \mathbf{v}\ ,\ [\mathbf{u}, \hat{\mathbf{v}}]\right\rangle
\end{aligned} \tag{A.3}
$$

From Lemma 3 we have

$$
\begin{aligned}
\cos\theta\left\langle \mathbf{n}\ ,\ [\mathbf{u}, \hat{\mathbf{v}}]\right\rangle &= \cos\theta\left\langle \mathbf{n}\ , \cos\theta\,[\mathbf{u}, \mathbf{v}] + \sin\theta\,[\mathbf{u}, \mathbf{n}] + (\nabla_{\mathbf{u}}\theta\cos\theta)\mathbf{n} - (\nabla_{\mathbf{u}}\theta\sin\theta)\mathbf{v}\right\rangle \\
&= \cos\theta\Big\langle \mathbf{n}\ , \cos\theta\,[\mathbf{u}, \mathbf{v}] + \sin\theta\,[\mathbf{u}, \mathbf{n}]\Big\rangle + (\nabla_{\mathbf{u}}\theta\cos^2\theta)\langle \mathbf{n}, \mathbf{n}\rangle \\
&- (\nabla_{\mathbf{u}}\theta\sin\theta\cos\theta)\langle \mathbf{n}, \mathbf{v}\rangle \\
&= \cos\theta\left\langle \mathbf{n}\ , \cos\theta\,[\mathbf{u}, \mathbf{v}] + \sin\theta\,[\mathbf{u}, \mathbf{n}]\right\rangle + (\nabla_{\mathbf{u}}\theta\cos^2\theta)
\end{aligned} \tag{A.4}
$$

Similarly we have,

$$\sin\theta\Big\langle \mathbf{v}\ ,\ [\mathbf{u},\hat{\mathbf{v}}]\Big\rangle = \sin\theta\left\langle \mathbf{v}\ ,\cos\theta\ [\mathbf{u},\mathbf{v}] + \sin\theta\ [\mathbf{u},\mathbf{n}]\right\rangle - (\nabla_{\mathbf{u}}\theta\sin^2\theta) \tag{A.5}$$

Using Equations (A.4) *and* (A.5) *in Equation* (A.3) *we get* $\rho(\theta) =$

$$\begin{aligned}
&(\cos\theta)\Big\langle \mathbf{n}\ ,(\cos\theta)[\mathbf{u},\mathbf{v}] + (\sin\theta)[\mathbf{u},\mathbf{n}]\Big\rangle - (\sin\theta)\Big\langle \mathbf{v}\ ,(\cos\theta)[\mathbf{u},\mathbf{v}] + (\sin\theta)[\mathbf{u},\mathbf{n}]\Big\rangle + \nabla_{\mathbf{u}}\theta \\
&= \cos^2\theta\left\langle \mathbf{n}\ ,[\mathbf{u},\mathbf{v}]\right\rangle + \cos\theta\sin\theta\left\langle \mathbf{n}\ ,[\mathbf{u},\mathbf{n}]\right\rangle - \sin\theta\cos\theta\left\langle \mathbf{v}\ ,[\mathbf{u},\mathbf{v}]\right\rangle \\
&- \sin^2\theta\left\langle \mathbf{v}\ ,[\mathbf{u},\mathbf{n}]\right\rangle + \nabla_{\mathbf{u}}\theta \\
&= \cos^2\theta\left\langle \mathbf{u}\times\mathbf{v}\ ,[\mathbf{u},\mathbf{v}]\right\rangle + \cos\theta\sin\theta\ \left(\left\langle \mathbf{n}\ ,[\mathbf{u},\mathbf{n}]\right\rangle - \left\langle \mathbf{v}\ ,[\mathbf{u},\mathbf{v}]\right\rangle\right) \\
&+ \sin^2\theta\left\langle \mathbf{u}\times\mathbf{n}\ ,[\mathbf{u},\mathbf{n}]\right\rangle + \nabla_{\mathbf{u}}\theta \\
&= \rho^{\mathbf{uv}}\cos^2\theta + \rho^{\mathbf{un}}\sin^2\theta + \alpha^{\mathbf{uv}}\sin 2\theta + \nabla_{\mathbf{u}}\theta = \rho_s(\theta) + \nabla_{\mathbf{u}}\theta
\end{aligned} \tag{A.6}$$

where, $\alpha^{\mathbf{uv}} = \frac{\langle\mathbf{n},[\mathbf{u},\mathbf{n}]\rangle - \langle\mathbf{v},[\mathbf{u},\mathbf{v}]\rangle}{2}$*, and* $\rho^{\mathbf{ab}} = \Big\langle \mathbf{a}\times\mathbf{b},[\mathbf{a},\mathbf{b}]\Big\rangle$.

Theorem 2 *For incompressible vector field* $\mathbf{u}$ *with a smooth energy, there exist a positive time step* η *such that gradient descent update decreases the energy at every iteration.*

Proof 6 *Consider an energy* $E(\theta) = \rho^2(\theta)$ *then derivative of* E *w.r.t* θ *is given by*

$$\begin{aligned}
\frac{\partial E(\theta)}{\partial\theta} &= \frac{\partial}{\partial\theta}\left(\rho^2(\theta)\right) = 2\rho\frac{\partial\rho(\theta)}{\partial\theta} \\
&= 2\rho\left(\frac{\partial\rho_s(\theta)}{\partial\theta} + \frac{\partial}{\partial\theta}\left(\nabla_{\mathbf{u}}\theta\right)\right)
\end{aligned}$$

$$\begin{aligned}\frac{\partial}{\partial\theta}\left(\nabla_{\mathbf{u}}\theta\right) &= \frac{\partial}{\partial\theta}\left((\nabla\theta)^T\mathbf{u}\right) = \frac{\partial}{\partial\theta}\left(\sum_i u_i\frac{\partial\theta}{\partial x^i}\right)\\ &= \sum_i\left(\frac{\partial u_i}{\partial\theta}\frac{\partial\theta}{\partial x^i} + u_i\frac{\partial^2\theta}{\partial\theta\partial x^i}\right) = \sum_i\left(\frac{\partial u_i}{\partial x^i}\right)\\ &= \operatorname{div}\mathbf{u}\end{aligned}$$

Therefore we have,

$$\begin{aligned}\frac{\partial E(\theta)}{\partial\theta} &= 2\rho\left(\frac{\partial\rho_s(\theta)}{\partial\theta} + \operatorname{div}\mathbf{u}\right)\\ &= 2\Big(\rho_s(\theta) + \nabla_{\mathbf{u}}\theta\Big)\Big((\rho^{\mathbf{un}} - \rho^{\mathbf{uv}})\sin 2\theta + 2\alpha^{\mathbf{uv}}\ \cos 2\theta + \operatorname{div}\mathbf{u}\Big)\end{aligned}$$

At $t = 0$*, we have* $\theta = 0$ *therefore,*

$$\frac{\partial E(\theta)}{\partial\theta}\Big|_{\theta\equiv 0} = 2\rho_s(0)(2\alpha^{\mathbf{uv}} + \operatorname{div}\mathbf{u}) = 2\rho^{\mathbf{uv}}(2\alpha^{\mathbf{uv}} + \operatorname{div}\mathbf{u})$$

Using gradient descent to update $\mathbf{v}$ *we have at time* $t = 1$

$$\begin{aligned}\theta^1(x,y,z) &= -\eta\frac{\partial E(\theta)}{\partial\theta}\Big|_{\theta\equiv 0}\\ &= -2\eta\rho^{\mathbf{uv}}(2\alpha^{\mathbf{uv}} + \operatorname{div}\mathbf{u}) = -\eta\mathcal{E}_0^{\rho}\end{aligned} \tag{A.7}$$

Detailed Proof of Convergence of Minimizing Non-Holonomicity Energy

To prove that the algorithm converges it suffices to show that

$$\begin{aligned} E(\theta^0) &\geqslant E(\theta^1) \\ E(0) &\geqslant E\Big(-\eta\mathcal{E}_0^{\rho})\Big) \\ \rho_s^2(0) &\geqslant \Big[\rho_s\Big(-\eta\mathcal{E}_0^{\rho}\Big) + \nabla_{\mathbf{u}}(-\eta\mathcal{E}_0^{\rho})\Big]^2 \\ (\rho^{\mathbf{uv}})^2 &\geqslant \Big[\rho_s\Big(-\eta\mathcal{E}_0^{\rho}\Big) - \eta\nabla_{\mathbf{u}}\mathcal{E}_0^{\rho}\Big]^2 \end{aligned} \tag{A.8}$$

For small angle θ we have from Equation (A.6)

$$\rho_s(\theta) \approx \rho^{\mathbf{uv}} + \rho^{\mathbf{un}}\theta^2 + 2\alpha^{\mathbf{uv}}\theta \tag{A.9}$$

Using Equation (A.9) *in Equation* (A.8) *we have*

$$\begin{aligned} \Big[\rho^{\mathbf{uv}} + \rho^{\mathbf{un}}(-\eta\mathcal{E}_0^{\rho})^2 + 2\alpha^{\mathbf{uv}}(-\eta\mathcal{E}_0^{\rho}) - \eta\nabla_{\mathbf{u}}\mathcal{E}_0^{\rho}\Big]^2 &< (\rho^{\mathbf{uv}})^2 \\ \Big[\rho^{\mathbf{un}}(\mathcal{E}_0^{\rho})^2)\,\eta^2 - (2\alpha^{\mathbf{uv}}\mathcal{E}_0^{\rho} + \nabla_{\mathbf{u}}\mathcal{E}_0^{\rho})\,\eta + \rho^{\mathbf{uv}}\Big]^2 &< (\rho^{\mathbf{uv}})^2 \\ \Big[\Big(\frac{\rho^{\mathbf{un}}}{\rho^{\mathbf{uv}}}(\mathcal{E}_0^{\rho})^2\Big)\,\eta^2 - \frac{1}{\rho^{\mathbf{uv}}}(2\alpha^{\mathbf{uv}}\mathcal{E}_0^{\rho} + \nabla_{\mathbf{u}}\mathcal{E}_0^{\rho})\,\eta + 1\Big]^2 &< 1 \\ \Big[A\,\eta^2 - B\,\eta + 1\Big]^2 &< 1 \end{aligned}$$

Where A,B are appropriately defined. It is therefore sufficient to show that for a small

positive η if $A\eta^2 - B\eta < 0$ the algorithm converges. where,

$$B = \frac{1}{\rho^{\mathbf{uv}}}(2\alpha^{\mathbf{uv}}\mathcal{E}_0^\rho + \nabla_{\mathbf{u}}\mathcal{E}_0^\rho) \tag{A.10}$$
$$A = \frac{\rho^{\mathbf{un}}}{\rho^{\mathbf{uv}}}(\mathcal{E}_0^\rho)^2$$

Thus we need to show:

$$A\eta < B$$

for the case $A > 0$ we then we have $\eta < \frac{B}{A}$ so, we need to show $B > 0$. Also when $A < 0$, we have $\eta > \frac{B}{A}$. Hence, there exists a non-negative time step η, $B > 0$.

From Equations (A.10) and (A.7) we have:

$$\begin{aligned} B &= \frac{1}{\rho^{\mathbf{uv}}}(2\alpha^{\mathbf{uv}}\mathcal{E}_0^\rho + \nabla_{\mathbf{u}}\mathcal{E}_0^\rho) \\ &= \frac{2\alpha^{\mathbf{uv}}\rho^{\mathbf{uv}}(2\alpha^{\mathbf{uv}} + \operatorname{div}\mathbf{u})}{\rho^{\mathbf{uv}}} + \nabla_{\mathbf{u}}\mathcal{E}_0^\rho \\ &= 4\alpha^{\mathbf{uv}}(2\alpha^{\mathbf{uv}} + \operatorname{div}\mathbf{u}) + \nabla_{\mathbf{u}}\mathcal{E}_0^\rho \end{aligned} \tag{A.11}$$

Under the assumption that the vector field $\mathbf{u}$ is divergence free have:

$$B \approx 8(\alpha^{\mathbf{uv}})^2 + \nabla_{\mathbf{u}}\mathcal{E}_0^\rho$$

Thus, when $\nabla_{\mathbf{u}}\mathcal{E}_0^\rho > -8(\alpha^{\mathbf{uv}})^2$ we have convergence.

Note 7 *If* $|\nabla_{\mathbf{u}}\mathcal{E}_0^{\rho}| < 8(\alpha^{\mathbf{uv}})^2$ *then the convergence condition holds. This bound on the gradient of energy subsumes a bound on non-holonomicity for the field. We described above that the reason for an iteration to diverge maybe because the gradient update at a point may increase the energy in the neighborhood. However, if the gradient of the energy is not a large negative number, the gradient update a point does not affect the neighborhood as enough to cause the energy to increase. i.e For gradient update at a point to effect the surrounding neighbourhood the gradient of energy has to be a large negative number. A region with high negative* $\nabla_{\mathbf{u}}\mathcal{E}_0^{\rho}$ *means that it is the region of streamline where we suddenly transition from very non-sheet region to a sheetlike region so fast that energy along* $\mathbf{u}$ *falls off faster than a limit.*

Note 8 ***(The case of non-zero divergence)*** *for a given smoothness level (given Lipschitz constant for energy), the regions where the update will be most sensitive is the sink regions in the field.*

B

Different Methods of Fitting Frames to Cardiac DTI

In this Apendix, we briefly review three different approaches to fitting local frames $F = [\mathbf{f}_1, \mathbf{f}_2, \mathbf{f}_3]^T$ to cardiac DTI data.

Babak Samari

Transmural (extrinsic geometry) frame The first approach considers $\mathbf{f}_1$ to be in the direction of the principal eigenvector of the tensor matrix (the eigenvector corresponding to the highest eigenvalue), $\mathbf{f}_3$ to be the component of the heart wall normal orthogonal to f_1 (as described in Section 8.2.1), and $\mathbf{f}_2 = \mathbf{f}_3 \times \mathbf{f}_1$ [76, 65]. In this way, the extrinsic geometry of the heart wall is combined with the local geometry of the fibers to build up the cardiac frame field. In this construction, we assume that at each voxel, $\mathbf{f}_1$ is tangent the myofiber passing through that voxel.

Diffusion tensor based frame The second approach, uses only the local information of the diffusion tensor matrices to build the entire frame field. Let $\mathbf{e}_1, \mathbf{e}_2$, and $\mathbf{e}_3$ represent the sorted eigenvectors of the tensor matrix according to their corresponding eigenvalue magnitudes. As explained in Section 3.3.1, e_1 is commonly taken to be the direction tangent locally to the direction of a myofiber. From histology, we know that cardiac myofibers preserve an elongated structure (i.e., they do not cross each other) [45, 82]. Moreover, myofibers are locally parallel to each other in sheet-like structures [45, 67]. These observations suggest at each voxel, the water molecules have the least freedom in motion in the direction represented by the eigenvector with the smallest eigenvalue, i.e., $\mathbf{e}_3$. Therefore we can assume that the orientation of a frame at a particular spatial position is aligned to the orientation of its tensor eigenvectors, i.e., $F = [\mathbf{e}_1, \mathbf{e}_3, \mathbf{e}_3]^T$. This frame is often used in the literature to describe local geometry [82, 67, 101, 49].

Sheet-based frame Alternatively, one can use the sheet-based coordiate system constructed in Section 8.2.2. Then $F = [\mathbf{e}_1, \mathbf{v}, \mathbf{e}_1 \times \mathbf{v}]^T$.

We believe that the sheet-based coordinate system better aligns with the local geometry of myofibers and resonates with the earlier findings in histology [45, 82]. As discussed in Part 3.3.4, eigenvalues for the second and third eigenvectors have a smaller magnitude in comparison with the principle one and are often close to each other, and thus interchangeable. Moreover, due to the low signal to noise ratio of in vivo DTI acquisitions, the smaller two eigenvectors are more vulnerable to noise.

Figure B.1 provides the histogram plots of connection form parameters fitted to our human in vivo dataset by incorporating the extrinsic geometry of the heart (the **Trans-**

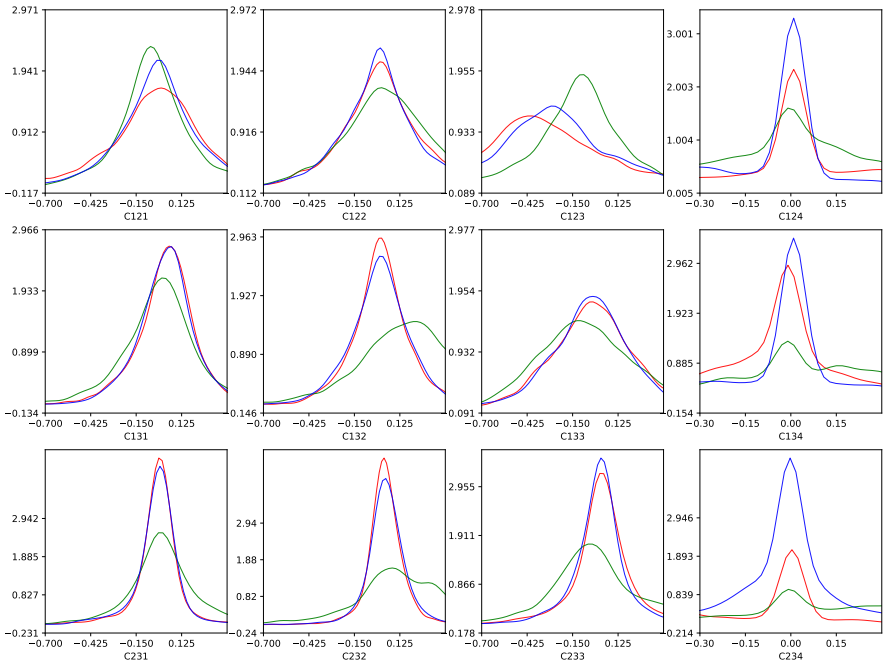

Figure B.1: The 12 Cartan connection parameters obtained via fits to the in vivo human data set using extrinsic geometry of the heart. The red, green and blue curves show histograms corresponding to the 110 ms, 160 ms and 220 ms time samples.

mural frame above). If we compare these fitting results with those in Figure 9.5, which used the sheet-based coordinate system, see that the spatial connection form parameters across different time samples during the cardiac beat cycle are clearly aligned better for the latter case. This behavior is expected since the heart has an almost stationary state during these three scan times.This suggests that our sheet-based coordinate system may be better suited for fitting frames to cardiac DTI.